Clemson University

TigerPrints

December 2018

Investigating the Use of Streaming and Robotic Dielectrophoresis to Enable Continuous Cell Sorting and Automatic Cell Transfer in Sample Preparation

Rucha Natu
Clemson University, naturuchah@gmail.com

Follow this and additional works at: https://tigerprints.clemson.edu/all_dissertations

INVESTIGATING THE USE OF STREAMING AND ROBOTIC
DIELECTROPHORESIS TO ENABLE CONTINUOUS CELL SORTING AND
AUTOMATIC CELL TRANSFER IN SAMPLE PREPARATION

A Dissertation
Presented to
the Graduate School of
Clemson University

In Partial Fulfillment
of the Requirements for the Degree
Doctor of Philosophy
Mechanical Engineering

by
Rucha Natu
December 2018

Accepted by:
Dr. Rodrigo Martinez-Duarte, Committee Chair
Dr. Xianchung Xuan
Dr. Richard Miller
Dr. Phanindra Tallapragada

ABSTRACT

The sorting of targeted cells or particles from a sample is a crucial step in the sample preparation process used in medical diagnosis, environmental monitoring, bio-analysis and personalized medicine. Current cell sorting techniques can be broadly classified as label based or label-free. Label-based techniques mostly rely on fluorophores or magnetic nanoparticles functionalized to bind with targeted cells. Although highly specific, this approach can be expensive and suffers from limitations in the availability of suitable markers. Label-free techniques exploit properties inherent to the cell, such as density and size, to simplify the sorting protocol and reduce cost by eliminating the need to incubate samples with labels. However, the specificity of separation is low due to minor differences between the density and size of many cells of interest. In this work, the use of dielectrophoresis (DEP) is emphasized as a label-free technique that exploits the combination of size and membrane capacitance of a cell as a marker. DEP is the movement of dielectric particles in the presence of a non-uniform electric field, which can be towards the electrode (positive DEP) or away from electrode (negative). The cell membrane capacitance used in this project can distinguish between cells based on their type, age, fate, and circadian rhythm to provide higher specificity than other label free sorting techniques. DEP has been demonstrated to separate various bio particles including viruses, plant and animal cells, biomolecules as well as stem cells. The work presented here integrates fabrication, numerical simulations, analysis and experimentation to focus on three main objectives 1) addressing the gaps of knowledge in

electrode fabrication 2) developing analytical system for rapid cell sorting of cell population 3) demonstrating feasibility of automated single cell sorting. These are addressed in the following paragraphs in that order.

Carbon electrodes are excellent alternatives for DEP because of the ease of fabrication of 3D electrode geometries and low voltages involved. Previous works have used these electrodes for applications like DEP, electrochemical bio sensing applications, fuel cells and micro-capacitors. The fabrication process involves photo patterning of SU-8 posts followed by carbonization in an inert atmosphere. During pyrolysis, the structures retain their shape, but show shrinkage. Though the fabrication process is reproducible, limited knowledge is available about the shrinkage process. Shrinkage affects the design of devices where these structures are used because the electrode dimensions after pyrolysis vary from the design and resulting electric field in the domain is affected. Previous works observed dependence of shrinkage on structure height and width, but a defining relation between shrinkage and the geometry was lacking. In this work, shrinkage is studied as an effect of degassing through the lateral and top surface area of the electrodes. Empirical relations are to enable prediction of shrinkage in the design stage

StreamingDEP refers to focusing particles into narrow streams with a proper play of positive DEP and drag force. This is important in continuous sorting because of the high throughput, limited exposure of cells to electric field and ability of integration to further analysis steps. Though streamingDEP has been demonstrated previously, the dependence of the particle focusing on system parameters has not been studied. In this

work, an analytical model is built to study the effect of electrode geometry, flow and electric field parameters as well as cell properties. The analytical expression developed here is validated by experiments and simulations.

Robotic transfer is required for efficient handling of cells and integration with analysis steps. Liquid handling robots are currently used in laboratories to transfer cells between different steps. Though they have precise control over the transfer of cells, the sorting ability is limited. To address these limitations, a proof-of-concept of roboticDEP device was innovated to enable transfer of targeted cells. The development of this system required studying the influence of DEP parameters in pick up and transfer of cells. The device was studied for elimination of contamination by using flow and electric field. The robotic DEP platform demonstrates a novel and unique approach to automated cell sorting with potential applications for single cell analysis, cell sorting and cell patterning.

DEDICATION

I would like to dedicate my dissertation to my beloved paternal grandmother Late

Mrs. Ramabai P. Natu and my maternal grandmother Late Mrs. Nirmala J.Lele for

instilling ideals of education and a strong value system in my family and me.

ACKNOWLEDGMENTS

I would like to sincerely thank my advisor Dr. Rodrigo Martinez-Duarte for giving me the opportunity to pursue research work and for guiding me through the journey towards my dissertation. My advisor has been a great source of inspiration during stressful times and I genuinely appreciate his patience. I have learned a lot from him over the years and through the several opportunities for professional and academic development provided by him. I would also like to thank professors in my dissertation committee, Dr.Xuan, Dr.Miller and Dr.Tallapragada for providing me guidance and helpful suggestions in my research work.

I am extremely grateful to the Department of Mechanical Engineering and Dr.Todd Schweisinger for providing me financial support through graduate assistantships. I thank Dr.Schweisinger for his support and encouragement during my teaching assistantship. Working as a teaching assistant with him has been a memorable experience and has given me opportunity to revisit undergraduate courses as well as to develop my soft skills and leadership qualities. The staff members in the mechanical engineering department are very helpful and I would like to thank all of them. I would specially thank Trish and Kathryn for their help. Jamie, Michael and Steven from the ME machine shop have been a great help in my lab work and I am grateful to them.

Multiscale Manufacturing laboratory has provided me various interdisciplinary research opportunities. My colleagues have been extremely helpful and supportive in my projects. The spirit of friendship and cooperation nurtured in this lab is admirable. I am

TABLE OF CONTENTS

Page

LIST OF TABLES

LIST OF FIGURES

CHAPTER ONE

INTRODUCTION

1.1 Motivation

Sample preparation is essential for diagnosis, personalized medicine, to conduct biomedical analysis and environmental sensing [1][2]. Cell sorting forms an important part of the sample preparation process. Cell sorting processes need to have specificity, rapidity and an ability for integration with analysis steps. Currently, fluorescent activated cell sorting (FACS) and magnetic activated cell sorting (MACS) are defined as the gold standards for cell sorting. These techniques rely on the use of conjugate labels, which bind with the cell of interest. Labels have high specificity, are not always available for the cell of interest. Moreover, these labels can interfere with cell processes. Label free techniques rely on cell properties like cell size and density. These techniques are inadequate to separate cells of different type but similar in size. This work uses dielectrophoresis (DEP), which is the movement of dielectric particle in the influence on non-uniform electric field, as a separation technique. Membrane capacitance along with cell size is used as a separation parameter in DEP. This work focusses on developing cell-sorting systems using DEP force. Two different approaches are explored here. The first approach target continuous focusing of cell population under the action of DEP and drag force. Objective is to understand the effect of system parameters on the focusing behavior of the particles. Second approach targets development of roboticDEP platform for cell pick up and transfer.

Carbon electrodes have been used for various applications like electrochemical sensors, biosensors, fuel cells, micro capacitors and electrodes for DEP devices. These provide a low cost, low operation voltage alternative to the use of metal electrodes, which are expensive for 3D fabrication and insulator-based electrodes, which use high voltages. The fabrication process of these electrodes includes photo patterning of a polymer called SU-8, followed by carbonization in inert atmosphere. During the carbonization process, the posts shrink as they lose material, but the shape of the structure is retained. Though the SU-8 fabrication is well characterized, the available knowledge about shrinkage behavior of the posts is limited. Study of shrinkage is important because the shrinkage affects the final dimensions of the posts and shows a variation from the designed dimensions. The electric field and gradient generated in the device depend upon electrode geometry and thus shrinkage can affect the application of these posts as sensors or electrodes. In this work, the shrinkage behavior is studied to understand the effect of structure geometry and carbonization parameters. Dependence of shrinkage on geometry of the SU-8 structures is addressed to provide insight into degassing during the carbonization process. Empirical relations are developed based on the effect of geometry and carbonization protocol to enable prediction of shrinkage in the design stage.

The next step of the work utilizes the electrode structures to develop a continuous cell separation device using DEP. Traditionally, DEP has been used as a batch sorting technique where cells are isolated from a sample by trapping them in specific locations using positiveDEP and then released at different times. The caveats of this approach are that particles are exposed to the electric field for long periods of time, which can impact

their viability [3], and that throughput is usually low since the DEP force must overcome the drag force on the particle to achieve trapping. Continuous sorting using NegativeDEP, also known as focusing, is a well-known approach to overcome these limitations. Cells are flowed through a channel but instead of trapping them, they are focused into streams thanks to the repelling force from electric field gradients positioned in strategic locations. Since the magnitude of repulsion depends on the cell properties, different cells can be focused into different streams located at a specific distance from the field gradient [4][5]. The feasibility of streaming DEP as a label free sorting process using positive DEP along with pressure-based flow has not been widely explored. Positive DEP has an untapped potential for continuous separation and is expected to provide a better spatial resolution than negative DEP. This system was further used to develop an analytical model to predict the streaming and capturing behavior of the particles suspended in a DEP channel.

The third part of this project focusses on automated pick and transfer of cells. The use of automated processes is desired for cell manipulation, especially with single cells to obtain precise control of the process. Few automated single cell manipulation devices use micro-grippers and mobile micro robots. These techniques have limited cell sorting ability and can have a low scope for parallelization. Liquid handling robots with high ability for parallel transfer of cells are used in laboratories to transfer cells into different sections between sample preparation steps. The cell sorting ability of these robots is limited to the use of size and image intensity as sorting parameters. Use of DEP as a sorting technique can enhance the cell selection process. 3D carbon electrode chips can enable pickup and sorting of several single cells in parallel. Based on this idea, the use of

robotic system along with DEP was investigated. The device developed in this work shows feasibility of automated cell transfer. It is further studied to understand the effect of different system parameters like cell properties, voltage and speed of operation on the performance. The use of device for cell sorting and single cell pick and transfer is explored.

1.2 Background

1.2.1 Label-free sorting techniques

Microfluidic techniques are extensively used in sample preparation. Use of microfluidics is advantageous because of the small instrument footprint which uses reduced volumes of sample and reagents, has potential for integrating functional components, multiplexing to enable parallel analysis of several samples and portability of point of care devices [6]. Techniques to address different steps in sample preparation using microfluidics have been developed for isolation of rare target cells like circulating tumor cells [7], hematopoietic stem cells [8], cancer stem cells [9], Protein and DNA fractionation[10], cell lysis [11][12], point of care detection [13] for example detection of *E.coli* [14] or Swine influenza virus [15], as well as towards personalized medicine and stem cell therapeutics [16,17] . Though each of these processes has been successfully tackled with microfluidics, the integration and packaging of several functionalities into a single system is proving to be a complex task [2]. Cell sorting is an important step in sample preparation. The cell separation approach depends on the target application. The efficiency, throughput, rate of cell sorting and the integration with post analysis steps

play an important role in selecting a sorting technique. Based on the applications, cell sorting can be broadly classified as sorting of populations and single cells.

Sorting of cell population has applications in therapeutics, enrichment of rare cells and diagnosis. The methods used for population sorting are different from the single cell sorting techniques. The focus here is on high sorting efficiency, specificity, rapid and high throughput. The ability to integrate with further analysis steps is an added advantage. Fluorescent activated cell sorting (FACS) [18], which uses fluorophore-conjugated antibodies as a discriminating factor and magnetically activated cell sorting (MACS) [19] which uses magnetic microbeads conjugated with antibodies are the gold standards for cell sorting. FACS can sort upto 70,000 cells per second with higher achievable rates with cost of purity. The major drawback of these methods is the use of external chemical labels to identify the target cells. These labels have limited specificity and there is no clear set of surface markers with sufficient specificity to identify promising cells. The labels can be retained in the separated population and potentially limit the use of these cells. There is a risk that the labels can also interfere chemically with the cell [20]. Moreover, these setups are very expensive and can have high cell losses. Density gradient cell sorting which utilizes the difference between cell densities is also prevalent. Intensive research is on label-free techniques to reduce complexity and cost of operation. Deterministic lateral displacement (DLD) [21,22], inertial microfluidics [23,24], acoustophoresis [25,26] have emerged as label-free techniques with high separation throughput. However, these techniques normally utilize the variation in size and shape of the involved cells and fail for cells with similar sizes. Aim of this work is to

use dielectrophoresis (DEP), a label free cell sorting technique for rapid and high throughput cell separation.

Single cell sorting and isolation is of paramount importance in sample preparation for studying cell to cell variability, cancer research where minority of cells have far reaching implications in cancer origin, developmental biology and drug screening [27]. Cell heterogeneity can affect cell decision-making and cell fate, and thus study of a single cell gains weightage. In case of single cell sorting, the cell specificity, ability to target and capture a single cell, easy accessibility after separation, high recovery rate and effective manipulation of the cell play an important role. For some single cell analysis systems, microwells or microchambers for sorting reaction reagents are necessary, which makes the ability to trap and transport cells necessary. Robotic manipulators are used to achieve high degree of resolution in this process. Microfluidic approach utilized for single cell sorting involves use of droplets based devices to trap a single cell in a drop [28], hydrodynamic focusing in arrays of microstructures designed to hold individual cells in place [29], dielectrophoresis [30] and optical traps to trap the target cells at focal point and exclude the other cells by the use of electric field [31]. Since single cell sorting process is required to be precise due to the small volume of the cell, various automated techniques have been used. Optical tweezers are used as tools for manipulating single cells for various biological applications[32][33], but the high intensity laser beam can damage the cells. Use of microrobotic arms, microgrippers and mobile microrobots to pick and transport micro/nano particles are also prevalent. These techniques have a precise control over the placement location of cell, but have limited scope for

6

parallelization and cell sorting [34–38]. The C1 and Polaris System by Fluidigm offer

solutions for automatic isolation of single cells followed by lysis and cell multiplexing in

an integrated system. C1 uses size based cell selection whereas Polaris enables cell

selection based on imaging of the stained cells [39]. DEP along with automated cell

manipulation has also been used to trap and transport cells. 3D manipulation of single

HeLa cells using DEP based electrode array were demonstrated by Sakamoto et al.[40].

The DEPArray NxT instrument for automated single-cell collection uses

dielectrophoresis (DEP) based cages to trap and move isolated cells with high throughput

to locations for downstream applications [41]. An important goal of this work is to

develop an automated single cell-sorting platform, which can selectively sort cells and

transfer them to specific locations, which can be later integrated further analysis steps.

The technique used to achieve the above two objectives is dielectrophoresis.

1.2.2 Dielectrophoresis as label-free sorting technique

     Dielectrophoresis is the movement of a dielectric particle in a non-uniform

electric field. DEP enables electrically controllable trapping, focusing, translation,

fractionation and characterization of particulate mineral, chemical, and biological

analytes within a fluid suspending medium. Because the dielectric properties of a particle

depend on both its structure and composition, dielectrophoretic forces access a much

richer set of particle properties than electrophoresis. DEP is particularly well suited to

applications at the small scales of microfluidic devices.

Table 1. 1.Comparison of different label free cell sorting techniques[20,42–44]

Technique	Separation Criteria	Types of cells	Resolution	Efficiency/ throughput	Limitation
Mechanical Filters	Size, deformability	Blood cells	Around 17 µm cells from 5-9 µm cells	10^9 cells/min with 90% efficiency	Size difference is necessary
DLD	Size and shape	Blood cells, liver cells		10^7 cells/min with 99+% efficiency	Difficulties with soft cells
Microstru-ctures	Size, Density, deformability	Blood, cancer cells	Smaller than 3 µm	95+%	Damaged by deformation
Inertial	Size	Blood cells and bacteria	~2-3 µm	10^6 cells/min, 90+% efficiency	High shear in channel, size
Acoustic	Size, density, compressibility	Blood	> 1 µm	10^8 cells/min	Invasive
DEP	Polarizability, size	Liposomes, yeasts, bacteria	Size difference <0.5 µm, viability	>90%, 105 cells/min	Difference in polarizability is needed
Optical	Refractive index and size	Silica particles	0.5 µm	10^3 cells/min	Complex system

On a larger, preparative scale, DEP methods are applicable to the purification, enrichment, and characterization of a wide range of environmental, biological and clinical components and significant progress has been made in developing technologies in these areas[45]. DEP was successfully used to manipulate viruses, DNA, proteins, plant cells, mammalian cells and special cells like stem cells. Different commercial platforms using DEP have developed in recent years. Commercial DEP platform, called Apocell was introduced for the separation of circulating tumor cells from white blood cells, aiming at high selectivity by using DEP with a throughput of 5000 cells/min [20]. Another commercial platform launched recently called as DEParator, which can process up to 1,50,000 cells per second. DEParray locks tens of thousands of cells in DEP actuated cages to transfer the target cells to the analysis areas. Cell show about 97.1% viability after DEP operation and no difference is seen in the growth of these cells with respect to the cells not subjected to DEP [46].

1.2.3 Carbon MEMS

Glass-like carbon electrodes are fabricated by set of methods termed as C-MEMS, in which an organic polymer is patterned and pyrolysed to obtain glass-like carbon microstructures. SU-8, a negative photoresist, a carbon precursor is widely used in the fabrication of carbon microstructures using the C-MEMS technique. Although other precursors can also be used to make planar films, such as positive tone photoresists like AZ and Shipley products, SU-8 is the material of choice when fabricating high aspect ratio structures with height above 10 μm [47]. The process of SU-8 photolithography

[48–57] includes the steps of 1)spin coating, where the substrate is coated with SU-8 photoresist 2) soft bake, for evaporation of the solvent in the resin 3) Exposure to UV light through a mask, during which, the area on the SU-8 layer, exposed to the light gets crosslinked. 4) Developing to wash away the uncross-linked resin. (Schematic is shown in Figure 1. 1). The crosslinked resin structures are retained on the substrate. In the next step these substrates are subjected to heat treatment in an inert atmosphere, during which, the SU-8 carbonizes and carbon posts are obtained. In the pyrolysis process, the carbon formed retains the structure of the SU-8 posts, but the posts experience shrinkage. The fabrication and pyrolysis processes are detailed in several works [48,56,58,59]. However the study of the shrinkage phenomena is conducted in limited number of works [60–62] and does not address all aspects of shrinkage.

Glass-like carbon posts fabricated in this way have enabled myriad applications such as biosensors [63,64], electrochemical sensors [65–67], fuel cells [68], batteries [69–72], micro capacitors[73,74], and cell sorting and manipulation using dielectrophoresis (DEP) [48,54,58,59,62,75] and electro-osmosis [76]. This technology provides a low cost alternative to the use of metal electrodes and increases the device throughput due to the distribution of the field in 3 dimensions.
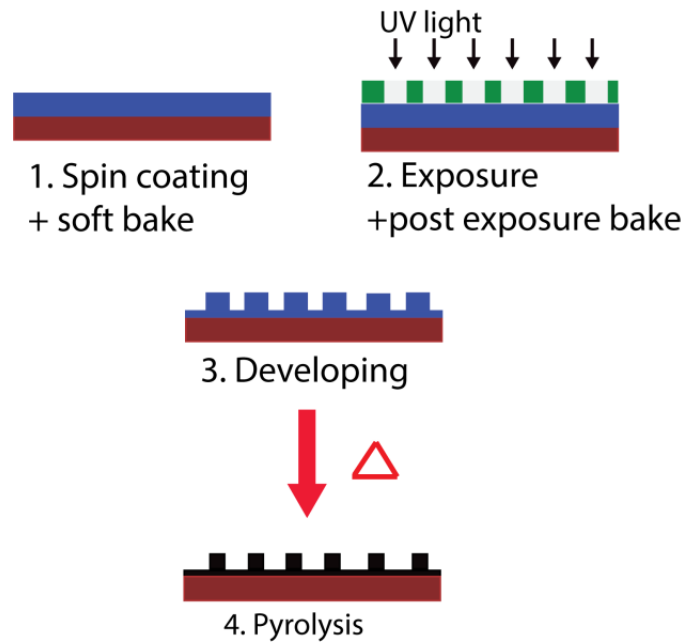
Figure 1. 1 Fabrication steps for 3D carbon electrodes

1.2.4 Use of carbon electrodes for dielectrophoresis

Most of the work in DEP relies on the use of microelectrodes made of metals like
gold and platinum contained in a microfluidic channel to induce non-uniform electric
field in the sample. However, the use of metal microelectrodes in direct contact with the
sample severely restricts the magnitude of the applied voltages, as one must prevent
sample electrolysis. Moreover, the fabrication of 3D metal electrodes is costly. Another
approach is the use of electrodes made by insulating materials which require application
of extremely high (~1000V) voltages to generate a uniform field, where insulated
structures can introduce a disturbance in field [77,78]. The field is disrupted by the use of
insulated posts placed in the channel. The use of insulator electrodes is advantageous as
they can be made in 3D with lower costs than metal electrodes and high throughput

devices can thus be made. The use of glass-like carbon electrodes in dielectrophoresis combines the advantages of metal-based DEP and insulator-based DEP (iDEP) and yields some other key benefits that make carbon-DEP an alternative to current DEP techniques [79]. The carbon electrodes allow the use of higher voltages than the metal electrodes without sample lysis and are suitable for voltages in the range of tens of volts instead of the hundreds or thousands of volts required in iDEP [80]. For high throughput systems, much taller electrodes are required. 3D carbon electrodes are an accepted alternative for high throughput DEP devices. Glass-like carbon is chemically very inert in almost all solvents/electrolytes. It withstands attack from strong acids such as nitric, sulfuric, hydrofluoric or chromic and other corrosive agents such as bromine. Reaction with oxygen occurs only at high temperature. Carbon being a building block of nature, glass-like carbon has excellent biocompatibility [56].

Several works have used 3D carbon electrodes for dielectrophoresis to obtain cell capture, separation, filtration as well as lysis. 3D carbon electrodes were integrated with CD-microfluidic devices to demonstrate the use of 3D electrodes as filters for yeast cells [50]. 3D carbon electrode devices are used in separation of bacterial cells [58], trapping of biomolecules like DNA [48], pathogen detection [81] and high throughput cell lysis [59]. Recently 3D carbon electrodes were used for enrichment of diluted populations [54] and to study the dielectrophoretic effect of fluorescent dyes on the cell [82]. Carbon electrodes fabricated by the use of C-MEMS techniques will be used in this work due to the advantages provided by them.

1.2.5 Cells of interest

This project uses different types of cells and particles for experimentation. The use of variety of cells enables the application of techniques studied here for diverse cell populations, particle properties, cell sizes and cell morphologies.. The pathogenic variety of yeast cells, known as the *Candida* cells are used in this work. *Candida* comprises an extremely heterogeneous group of fungal organisms that can all grow as yeast morphology. Species such as *C.albicans* can produce a filamentous type of growth called as hyphae. The size of these cells is around 4-6 μm. Another species considered in this work is *C.tropicalis*, which has a size of 4-8 μm and can also show hyphae [83]. *Candida* species are most frequently isolated from the oral cavity, and vulvovaginal and urinary tracts and are detected in approximately 31–55% of healthy individuals. *C.albicans* and *C.tropicalis* cells used in this work were cultured for 1 day before use, in yeast malt broth (Sigma Life Science) supplemented with 40% glucose solution to get a final concentration of 1% glucose. Sugar solution is prepared with 200 ml distilled water by adding 18gm Sucrose, 0.5 gm dextrose and 0.3 gm Bovine Albumin Serum. The cell culture for DEP is prepared by centrifugation and washing of the cell sample with the sugar solution at least thrice. The cells were centrifuged and washed with sugar solution thrice, to adjust the final conductivity of the media to $2.5*10^{-3}$ S/m. The cell concentration used was $\sim 10^6$ cells/ml.

1 μm and 10 μm polystyrene particles were also used in this work. These are homogenous spherical particles with low intrinsic conductivity, which carry slight surface charge. The surface conductance and the particle size dominate the behavior of

these particles under the action of DEP force [84]. 1μm polystyrene beads were purchased from Bangs Laboratories (lot no. 9396) while 10 um beads were acquired from Magsphere (catalog no.PS010UM). Particle suspensions were prepared in distilled water supplemented with 0.1% Bovine Serum Albumin (Sigma-Aldrich, MO, USA) by weight to a particle concentration of ~10^6 /ml and electrical conductivity 10^{-5} S/m.

The Rat Adipose Stem Cells (RASCs) were used for the DEP experiments. Adipose stem cells are multipotent and have potential for a wide range of therapeutic applications. Use of these cells enabled the study of response of stem cells to the DEP applications developed here. The Rat Adipose Stem Cells (RASC) used for this experiment are acquired from the Cell and Tissue Culture Laboratory in Bioengineering Department, at Clemson University. The cell strains are cultured in DMEM (Dulbecco's Modification of Eagle's Medium) x1 (Mediatech, Inc. Manassas, VA), 10% Culture Supplement (Discovery Labware Inc, Bedford, MA) and 1% Antibiotic Antimycotic Solution (Mediatech, Inc., Manassas, VA) for 5 days to obtain a nearly confluent cells in 5 ml flasks.

Numerical study in this project uses the properties of neural stem cells. Neural stem cells can be differentiated as three types of cells in the central nervous system: neurons, astrocytes, and oligodendrocytes [85], with neurons being the most sought-after type of cell. Neurons obtained from the neurogenic progenitors play an important role in the treatment of Parkinson's disease, spinal cord injuries, and motor neuron diseases and also to restore lost neuronal populations [86]. Numerical simulations considered

separation of astrogenic progenitors SC23 and neurogenic progenitors SC27 with radius of ~7 μm.

1.3 Dissertation framework

Aim of this work can be divided in three fronts: 1) studying the shrinkage during pyrolysis process for the formation of carbon electrodes and developing an empirical model, 2) exploring continuous particle separation to understand dependence on system parameters, 3) demonstrating feasibility and studying the factors affecting the performance of robotic transport of selected cells. The Chapter 1 contains the background study of different cell sorting methods that are currently available and comparison between these. Introduction of dielectrophoresis as label free cell sorting technique is also detailed. Carbon-MEMS and their applications for DEP are discussed briefly. Chapter 2 focuses on the theoretical background required for this project. Theory of DEP and particle polarization to derive Clausius Mossotti factor is addressed. Different forces acting on the particle suspended in the microchannel are also discussed. Chapter 3 focusses on the first objective, where the study of pyrolysis process to obtain carbon electrodes is conducted. Focus here is on the effect of geometry and pyrolysis conditions in determining the shrinkage of the structures. Chapter 4 discusses the concept of streaming DEP used for sorting of cell populations with a numerical system to study the sorting of neural stem cells. Chapter 5 develops analytical expression for streaming DEP, which is experimentally validated by using DEP with polystyrene particles. A non-dimensional streaming DEP number is developed to predict the fate of a particle in microchannel under the influence of flow and DEP. Chapter 6 focusses on the

development of automated cell sorting device with an application to single cell sorting. The device operation is studied for parameters affecting the pick, wash and place steps. A numerical study of electrode geometry to pick up single cell robotically is also conducted. Chapter 7 summarizes the contributions of this work and discusses the scope for future work in this domain.

CHAPTER TWO

THEORETICAL BACKGROUND

2.1 Dielectrophoresis force on a particle

Dielectrophoresis (DEP) is a label free cell sorting technique. It refers to the force exerted on the induced dipole moment of an uncharged dielectric and/or conductive particle by a non-uniform electric field. It was first described by Pohl[87]. DEP force is observed for AC as well as DC excitation. In this work, AC excitation is used to obtain the non-uniform electric field. The starting point to consider the DEP force is the consideration of a small physical dipole consisting of equal and opposite charges +q and −q existing in a particle in an electric field $\bar{E}$. If the electric field is non-uniform, the dipole will experience a net force given by,

$$\bar{F} = q\bar{E}(\bar{r} + \bar{d}) - q\bar{E}(\bar{r}) \qquad (2.1)$$

Where, $\bar{r}$ is the position vector of −q and $\bar{d}$ is the vector distance between charges +q and −q. when $\overline{|d|}$ is small compared to the characteristic dimension of the electric field non- uniformity, Equation (2. 1) can be simplified further. Electric field about the position $\bar{r}$ can be expanded using the Taylor's series as,

$$\bar{E}(\bar{r} + \bar{d}) = \bar{E}(\bar{r}) + \bar{d}.\nabla\bar{E}(\bar{r}) + \frac{\bar{d}^2}{2!}\nabla^2\bar{E}(\bar{r}) + \cdots \qquad (2.2)$$

The terms of the order $\bar{d}^2, \bar{d}^3$ and so forth are neglected for moderately inhomogeneous electric fields [45]. By combining Equations (2. 1) and (2. 2), the resultant force obtained is,

$$\bar{F} = q\bar{d}.\nabla\bar{E}(\bar{r}) \qquad (2. 3)$$
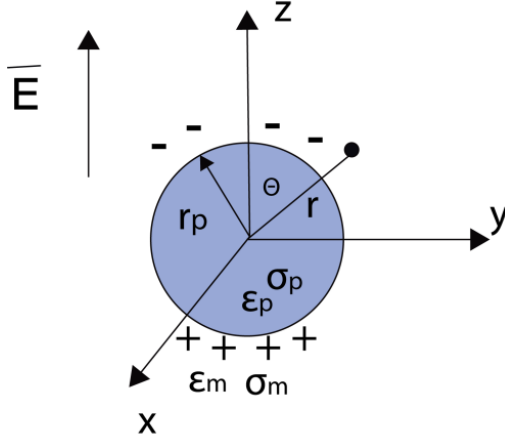
Figure 2. 1 Dipole created in a dielectric spherical particle in the presence of electric field

In the Equation (2. 3), for an infinitesimal dipole, with the limit $\overline{|d|} \rightarrow 0$, the dipole moment is given by $\bar{p} \equiv q\bar{d}$. Equation (2. 3) implies that, no net force acts on the dipole unless the electric field is non-uniform. This is valid for the cases where the scale of electric field non-uniformity is large compared to the particle dimensions. In the case of closely spaced particles, where the non-uniformity in the field induced by the particles is comparable to the particle size, Equation (2. 3) becomes inaccurate and higher order terms of Equation (2. 2) need to be retained [88].

By considering the coordinate system with origin at the center of the particle, the system can be defined by spherical co-ordinates r, θ in 2 dimensions. To obtain the equation for DEP force, effective moment method can be used, where the effective dipole

moment for the dipole is defined by $\bar{p}_{eff}$ and the electrostatic potential due to point diploe in the dielectric medium with permittivity ε, is given as,

$$\emptyset = \frac{\bar{p}_{eff}cos\theta}{4\pi\varepsilon r^2} \tag{2.4}$$

Where θ and r are polar angle and radial position in spherical coordinates. If the insulating particle is spherical, with radius R and permittivity ε_p , conductivity σ_p suspended in a fluid with permittivity εm and conductivity σ_m , subjected to AC electric field $\overline{E}(r)$ of magnitude E_0, applied at the frequency f, electrostatic potential $\emptyset_m$ outside the sphere and $\emptyset_p$ inside the sphere take the form;

$$\emptyset_m = -E_0 rcos\theta + \frac{Acos\theta}{r^2} \text{ for r>R} \tag{2.5}$$

$$\emptyset_p = -E_0 rcos\theta + \underline{B}rcos\theta \text{ for r>R}$$

Where, $\underline{A}$ and $\underline{B}$ are complex numbers. The first term contained in $\emptyset_m$ is due to the imposed electrostatic field and second term is due to the induced dipole due to the particle, given by $\emptyset$ in Equation (2. 4). At the particle-media interface, a boundary condition with equal potential is applied as,

$$\emptyset_m(r_1 = R, \theta) = \emptyset_p(r_2 = R, \theta) \tag{2.6}$$

The second boundary condition at the particle-media interface is the continuity for the displacement flux vector across the boundary,

$$\sigma_m E_m - \sigma_p E_p + \frac{d(\varepsilon_m E_m - \varepsilon_p E_p)}{dt} = 0 \tag{2.7}$$

To simplify the analysis for frequency domain, d/dt can be replaced by $j2\pi f$, where j is $\sqrt{-1}$. Equation (2. 6) takes the form,

$$\underline{\varepsilon_m}\underline{E_m}(r_m = R, \theta) = \underline{\varepsilon_p}\underline{E_p}(r_p = R, \theta) \qquad (2.8)$$

Where, $\underline{\varepsilon_m}$ and $\underline{\varepsilon_p}$ are complex permittivity values, $\underline{\varepsilon_m} = \varepsilon_m - \frac{j\sigma_m}{2\pi f}$ and $\underline{\varepsilon_p} = \varepsilon_p - \frac{j\sigma_p}{2\pi f}$ for media and particle respectively. The complex permittivity models the polarizable material as the electric equivalent to a resistor in parallel with a capacitor. This captures both low frequency conductive and high frequency dielectric charging mechanisms. For materials such as a cell or polymeric micro particle, polarization involves the contribution the physical movement of free charges described by conduction and the field-induced perturbation of bound charges, such as in dielectric materials. Physically, surface charges induced at a particle interface are composed of induced charges as well as free charges arising due to conductivity. The cell or particles are considered as lossy electric materials, i.e the materials which have both a permittivity and conductivity [89]. On solving, the values of A and B are obtained is,

$$A = (\frac{\underline{\varepsilon_p} - \underline{\varepsilon_m}}{\underline{\varepsilon_p} + 2\underline{\varepsilon_m}}){r_p}^3 E_0 \qquad (2.9)$$

$$B = \frac{3\underline{\varepsilon_p}}{\underline{\varepsilon_p} + 2\underline{\varepsilon_m}}$$

Using Equations (2. 4)-(2. 9)

$$\bar{p}_{eff} = 4\pi\varepsilon_1\left(\frac{\underline{\varepsilon}_p - \underline{\varepsilon}_m}{\underline{\varepsilon}_p + 2\underline{\varepsilon}_m}\right)r_p{}^3E_0 \qquad (2.\,10)$$

According to the effective moment method, the force $\bar{F}$ can be expressed in terms of effective moments identified for solutions for induced electrostatics field [88]. $\left(\frac{\underline{\varepsilon}_p - \underline{\varepsilon}_m}{\underline{\varepsilon}_p + 2\underline{\varepsilon}_m}\right)$ is the Clausius Mossotti [fcm] function and it can be further separated into real Re[fcm] and imaginary parts Im[fcm]. For the time varying field, where there is no phase gradient in the AC field, the imaginary part disappears[90] and the time averaged force is obtained by combining Equations (2. 2)and (2. 10),

$$F_{DEP} = 2\pi\varepsilon_m Re[fcm]r_p{}^3\bar{E}.\nabla\bar{E} \qquad (2.\,11)$$

Equation (2. 11) gives the DEP force acting on the particle with radius R in AC electric field $\bar{E}$. Magnitude of this force depends on $\bar{E}.\nabla\bar{E}$, r_p, ε_m and Re[fcm] whereas the direction depends on Re[fcm]. If Re[fcm] is positive, the force is positive and particle gets attracted towards the electrode. The force is negative when Re[fcm] is negative and the particle repels the electrode.

2.2 Particle polarization

Clausius Mossotti factor is the dielectrophoretic signature of a cell. This determines if the DEP force will be positive or negative. The Clausius Mossotti factor the particle depends on its permittivity and conductivity. The value varies from -0.5 to 1. The value of Clausius Mossotti factor depends on frequency of the current applied when the conductivity and permittivity for the particle and media are fixed. With the change in

21

frequency, the value of Re[fcm] can be catered to obtain positive or negative DEP. The frequency at which the sign of Re[fcm] factor changes is called as the crossover frequency f_0. Figure 2. 1 shows the change Re[fcm] with the change in conductivity.
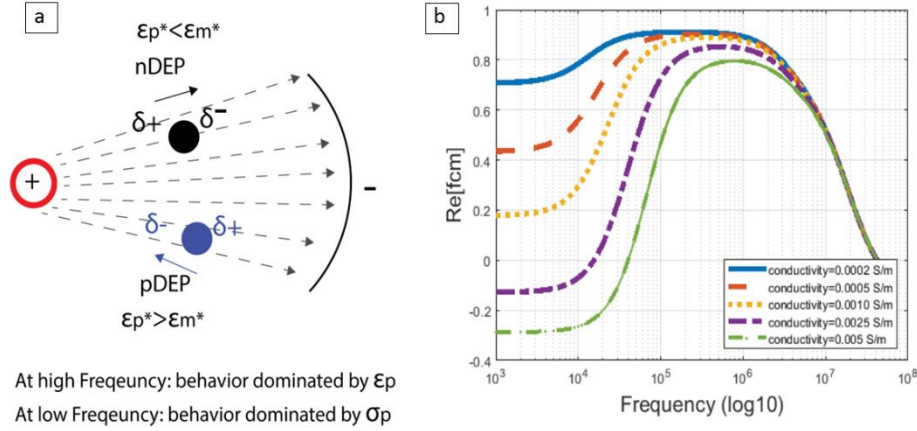
Figure 2. 2 Dielectrophoretic response of cell. a) Positive and negative DEP acting on a particle in the presence of electric field gradient is shown in the figure. b) The Re[fcm] value depends on the conductivity of the media and cell. With the increase in media conductivity, the Re[fcm] value decreases and after a certain conductivity, it reverses sign and particles experience negative DEP. The figure on the right shows the change in Re[fcm] of *S.cerevisiae* cells with the increase in media conductivity.

The fcm factor given in Equation (2. 10) is for homogeneous spherical particles. In case of bio-particles, the cellular domain is made of the cytoplasm, nucleus and cell wall and it is no longer homogeneous. The analysis conducted above for the homogeneous dielectric is expanded by considering each domain as an electric shell.

For the cells used in this work and the biological particles common in experiments, the single shell model is used. This model considers cytoplasm, cell membrane and media as the three domains. The boundary conditions stated in Equations (2. 6)-(2. 8) are used at the cytoplasm-membrane interface and the membrane-media interface. The value of fcm obtained for single shell model is given as,

$$fcm = \left(\frac{\underline{\varepsilon}_{eff} - \underline{\varepsilon}_m}{\underline{\varepsilon}_{eff} + 2\underline{\varepsilon}_p}\right)$$
(2. 12)

Where, $\underline{\varepsilon}_{eff}$ is the effective complex permittivity of the cell given by,

$$\underline{\varepsilon}_{eff} = \underline{\varepsilon}_{mem} \frac{\left(\frac{r_{outer}}{r_{inner}}\right)^3 + 2\frac{\underline{\varepsilon}_{cyt} - \underline{\varepsilon}_{mem}}{\underline{\varepsilon}_{cyt} + 2\underline{\varepsilon}_{mem}}}{\left(\frac{r_{outer}}{r_{inner}}\right)^3 - \frac{\underline{\varepsilon}_{cyt} - \underline{\varepsilon}_{mem}}{\underline{\varepsilon}_{cyt} + 2\underline{\varepsilon}_{mem}}}$$
(2. 13)

Where, r_{inner} and r_p are inner and outer diameters of the cell (d_0 is the thickness of cell membrane and $r_p = r_{inner} + d_0$, $d_0 \ll r_p$) and $\underline{\varepsilon}_{cyt}$ and $\underline{\varepsilon}_{mem}$ are complex permittivity of cytoplasm and membrane. Charges build up at the membrane-medium interface with a characteristic relaxation time t and thus at a characteristic relaxation frequency f_r, given by $1/(2\pi t)$. For frequencies much lower than fr, the value of $\frac{\underline{\varepsilon}_{cyt} - \underline{\varepsilon}_{mem}}{\underline{\varepsilon}_{cyt} + 2\underline{\varepsilon}_{mem}} = 1$ [91]. The Equation (2. 13) can be simplified as,

$$\underline{\varepsilon}_{eff} = \underline{\varepsilon}_{mem} \frac{\left(\frac{r_{outer}}{(r_{outer} - d_0)}\right)^3 + 2}{\left(\frac{r_{outer}}{(r_{outer} - d_0)}\right)^3 - 1} \cong \underline{\varepsilon}_{mem}\left(\frac{r_{outer}}{d_0}\right)$$
(2. 14)

By defining membrane capacitance of the cell as, $C_{mem} = Re[\underline{\varepsilon}_{mem}]/d_0$, using Equation

(2. 14), one gets

$$C_{mem} = Re[\underline{\varepsilon}_{eff}]/d_0 \qquad (2.\ 15)$$

For frequencies much lower than f_r, the crossover frequency f_0 can be given as[92],

$$f_0 \approx \frac{\sigma_m}{\sqrt{2}\pi r_p C_{mem}} \qquad (2.\ 16)$$

C_{mem} is cell specific plasma membrane capacitance and varies with cell age,

morphology as well as circadian rhythms. Combination of r_p and C_{mem} can be used to

distinguish cells based on the difference in their radius and cell membrane properties. The

real part of fcm can be determined in terms of membrane capacitance, given by [93],

$$Re[fcm] = \frac{\left(\sqrt{2}\pi r_p C_{mem}f\right)^2 - (\sigma_m)^2}{\left(\sqrt{2}\pi r_p C_{mem}f\right)^2 + 2(\sigma_m)^2} \qquad (2.\ 17)$$

Equation (2. 17) enables the use of cell membrane capacitance to determine Re[fcm]

for the cells at frequencies lower than the relaxation frequencies. Membrane capacitance

was shown to change due to subtle cell changes including cell age, size, morphology,

early apoptosis, fate and circadian rhythms[94–98]. Thus, the membrane capacitance is

an inherent cell property that can distinguish the cell. Equation (2. 17) enables the use of

membrane capacitance in a product with cell radius and this enables one to use both the

size and the inherent cell properties as distinguishing parameters for the cell. For

example, Labeed and colleagues have demonstrated the separation of mice neurogenic progenitors from a mixture [99] while Bagnaninchi et al. used membrane capacitance to detect differentiated adipocytes and osteoblasts from their progenitors [100]. Membrane capacitance has also been used to identify six main leucocyte subpopulations in hematopoietic lineage [101]. While Stephens et al. have characterized how the membrane capacitance of Clostridium difficile can be used for separation from peripheral blood cell harvest, Talary et al. demonstrated the separation and enrichment of hematopoietic stem cells that express CD34+ from bone marrow and peripheral blood [97,102]. Furthermore, Flanagan et al. concluded that distinct changes in the dielectrophoretic properties of the neural stem cells are observed before the presence of specific cell-surface proteins (antigens) can be detected [103] and Vykoukal et al. used DEP coupled with field flow fractionation to enrich putative stem cells from adipose tissue [104].

In this work, one objective is studying the impact of device design and experimental protocol on the throughput and efficiency when separating neurogenic progenitor cells (SC27) from astrogenic ones (SC23) in a sample of neural stem/progenitor stem cells (NSPCs). The study presented here is based on the experimental results by Labeed and co-workers. Labeed et al. [99] have shown how the membrane capacitances of SC27 and SC23 huNSPCs are different even though they are remarkably similar in their size and levels of nestin and sox2 markers. Their experimental results are replicated here in Figure 2. 3, with SC23 cells displaying a membrane capacitance value of 9.9 ± 0.2 mF/m^2 and SC27 cells of 7.6 ± 0.3 mF/m^2 and both overlapping in the size range of 6.57 to 7.75 μm.

(a)   (b)   (c)
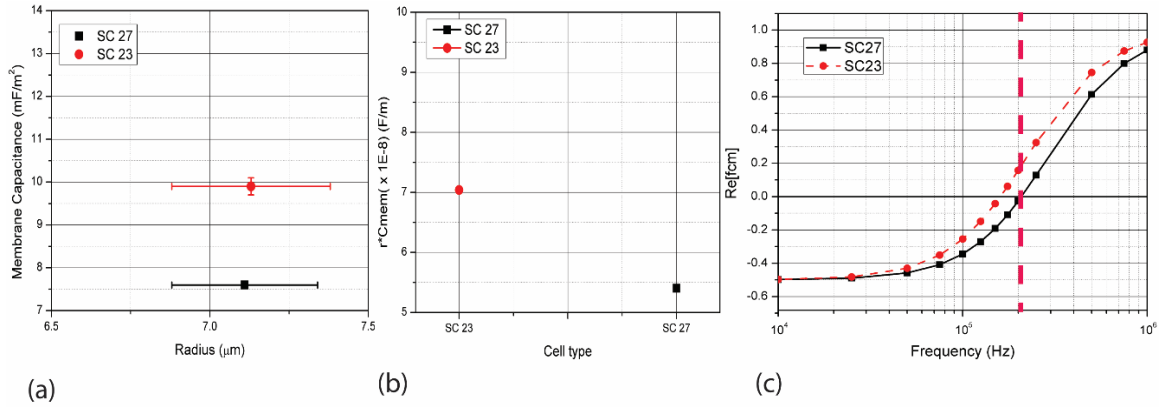
Figure 2. 3 The radius and membrane capacitance of different cells considered in this work as obtained experimentally by Labeed et al. [99].The radius and membrane capacitance of different cells considered in this work as obtained experimentally by Labeed et al. [99]. The membrane capacitance of SC23 cells is 9.9 ± 0.2 mF/m2 while that of SC27 is 7.6 ± 0.3 mF/m2. The cell radius lies between 6.57 and 7.75 μm; (b) The product of radius and membrane capacitance for SC23 and SC27 is different and can be used to further distinguish the two types of cells. The values of rCmem for SC27 and SC23 used here are $(5.40 \pm 0.06) \times 10^{-8}$ F/m and $(7.50 \pm 0.05) \times 10^{-8}$ F/m respectively. Note the small deviation on the average values (c). The values of the real part of the Clausius Mossotti factor Re[fCM] for SC23 and SC27 as frequency changes are obtained using Equation (2. 2) using the r and Cmem values shown in Figure 2. 3a. At the frequency of 200 kHz (dashed red line), the cells SC23 and SC27 show the highest difference in their Re[fCM] values, whereas SC23s show a positive value of 0.15, and SC27s show a slight negative −0.02.

For the homogenous polystyrene particles considered in this work, the electrophoretic behavior cannot be completely explained by shell model. Though these particles have low intrinsic conductivity, the measured conductivity on the particle is high [84,105] and researchers have attributed this conductivity to the movement of counter ions to the surface charge on these particles. The total particle conductivity for these particles is defined as,

$$\sigma_p = \sigma_{int} + \frac{2K}{r_p} \tag{2.18}$$

Where, K is the surface conductance and σ_{int} is the internal particle conductivity. It is important to note that the particle conductivity for polystyrene particles is inversely proportional to the radius r_p of the particle.

2.3 Forces acting on a particle in microchannel

Pressure driven flow is applied in the micro channels described in this work. The channel Reynold's number is defined as, $\rho U_a D_h / \mu$, where, U_a is the mean fluid velocity in the microchannel, ρ is the fluid density, D_h is the hydraulic diameter of the channel and μ is the dynamic viscosity of the fluid. Since the channel is closely represented by a rectangle, the hydraulic diameter is given by 2wH/(w+H), where w is the width of the channel and H is the channel height. For the system of electrode arrays embedded in the channel, w is replaced by gap between the electrodes. For the systems considered in this work, the Reynold's number is between 1 and 10. The velocity of fluid u, in the channel

is computed by solving the Navier Stokes equation with the continuity equation in the domain. The flow is assumed to be incompressible and steady.

$$\nabla . u = 0 \qquad (2.\ 19)$$

$$\rho(u.\nabla)u = -\nabla p + \mu\nabla^2 u \qquad (2.\ 20)$$

Different forces act on the particles suspended in a flow inside a microchannel. These are shown in Figure 2. 4. By assuming the particles to be spherical, the particle Reynold's number is defined as, $\rho U_a r_p/\mu$, where, rp is the particle radius. For the cells and particles considered in this work, the Reynold's number is smaller than 1 and the drag force, F_{Drag}, acting on the particles can be approximated by Stoke's law,

$$F_{Drag} = 6\pi\mu r_p(u - v) \qquad (2.\ 21)$$

Where u is the flow velocity and v is the particle velocity. For the particles which are trapped at the electrodes, in a microfluidic channel with a flow u, relative particle velocity, $v = 0$. For DEP operation, when cells are trapped at the electrode, it is very important that the cells remain captured at the electrode during this step. Thus the drag force acting on these cells should be smaller than the DEP force. The value of u for fluid can be selected by equating the drag force acting on the particle with the DEP force. Thus maximum value of u, under which a cell will remain trapped is given by,

$$u_{max} = \frac{2\pi\varepsilon Re[f_{cm}]r_p{}^3\nabla E^2}{6\pi r_p\mu} \qquad (2.\ 22)$$

A particle suspended in the microchannel is also affected by the sedimentation force. For a particle with mass density ρ_p, the sedimentation force is given by,

$$F_{Sedi} = 4\pi r_p{}^3 (\rho - \rho_p) g/3 \qquad (2.23)$$

Where, g is the acceleration due to gravity. Diffusion can play an important role in particle motion in the microchannel. The particle Peclet number (Pe) is defined as $\frac{6\pi\mu r_p U_a L}{kT}$, where L is the characteristic length, k is the Boltzmann constant and T is the absolute fluid temperature. Typically, when Pe is greater than 1, inertial forces dominate particle migration over diffusion, whereas for Pe values smaller than 1, diffusion is dominant [106]. For the cases considered in this work, Pe is greater than 1 hence the effect of diffusion is negligible. Particle suspended in the fluid are also subjected to inertial forces in the regime where particle Reynolds number is comparable to 1. The inertial focusing of particles in a straight channel similar to the one considered in this work, is driven by counter action of two types of inertial forces, namely, shear lift force and wall lift force. The shear lift depends on the curvature of the fluid velocity profile and its interaction with finite sized particle. The wall induced lift results from the disturbance of the flow field around the suspending particles and its effect because of the wall [107–109]. When the particle is small compared to the channel size, the net lift force is given by,

$$F_L = \frac{\rho U_a{}^2 r_p{}^4}{D_h{}^2} f_L(Re_c, x) \qquad (2.24)$$

Where, D_h is the hydraulic diameter of the channel, f_L is the lift coefficient which is a function of particle position with channel cross-section x and channel Reynold's number Re_c. These lift forces for straight channels are observed to be much smaller than the DEP force. The other steric lift force which acts very close to the wall of the channel, is considered in literature as [110,111],

$$F_L = \frac{1.032\mu r_p{}^3 U_a}{D_h(x - r_p)}$$
(2. 25)

Where x is the particle position with respect to the wall. This force is at least ten times smaller than the DEP force and particle drag force in the channel and is neglected in the analysis. Thus, the dominating forces considered to act on the particle in suspension are DEP, sedimentation force and hydrodynamic drag force. The particle velocity can be determined by analyzing these forces on the particle. Hence, the motion of the particle in the microfluidic channel is influenced by the total force F_t, which is calculated by vector summation of F_{DEP}, F_{Drag} and F_{Sedi}:

$$F_t = F_{Drag} + F_{DEP} + F_{Sedi}$$
(2. 26)

According to Newton's second law of motion, the total force F_t can also be expressed as,

$$m_p \frac{dv}{dt} = F_t$$
(2. 27)

where the mass of the particle is m_p and v is particle velocity. The total force acting on a particle is given by,

$$m_p \frac{dv}{dt} = 6\pi\mu r_p(u - v) + F_{DEP} + F_{Sedi} \tag{2.28}$$

Equation (2. 7) can be considered a general equation from which the sum of forces on a particle can be obtained. By solving Equation (2. 28), the particle velocity can be obtained as,

$$v = \left(v_0 - u - \frac{F_{DEP} + F_{Sedi}}{6\pi\mu r_p}\right)e^{-\left(\frac{6\pi\mu r_p}{m_p}\right)} + u + \frac{F_{DEP} + F_{Sedi}}{6\pi\mu r_p} \tag{2.29}$$

Where v_0 is initial particle velocity. The characteristic time of particle acceleration is given by,$m_p/6\pi\mu r_p$, which is much smaller (~10-6 seconds) than the typical observation time of 1 second for particles considered in this work. Thus, Equation (2. 29) can be written as[5,112],

$$v = u + \frac{F_{DEP} + F_{Sedi}}{6\pi\mu r_p} \tag{2.30}$$

Equation (2. 27) is used in this work to obtain the particle velocity. The instantaneous particle position can be determined by integrating velocity v with time.

$$x_p = x_0 + \int_0^t v dt \tag{2.31}$$

In Equation (2. 31), x_p is the instantaneous position of the particle and x_0 is the initial

particle position. The equations developed in this chapter form the basis of this work are

used for further analysis and numerical simulations.
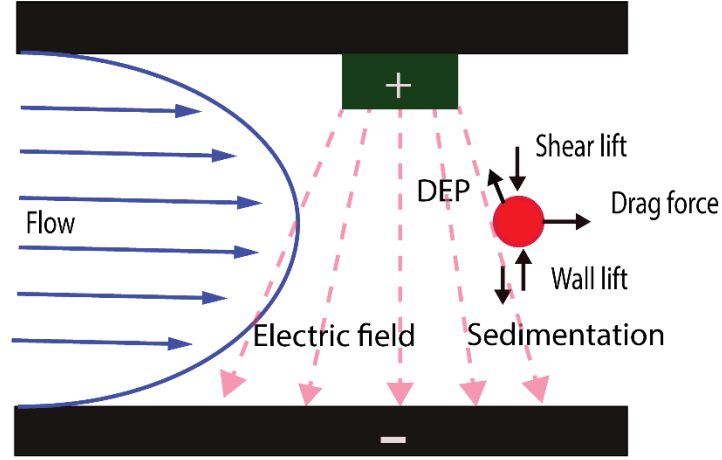
Figure 2. 4 Schematic showing different forces acting on a particle suspended in a
microchannel with non-uniform electric field

In the presence of electrodes in the microchannel domain, the electromagnetic

field is governed by Maxwell's equations. By considering negligible magnetic field, the

equations for electromagnetic relations can be stated by Equations (2. 32)-(2. 34),

$$\nabla.\,(\varepsilon E) = \rho_q \qquad (2.\ 32)$$

$$\nabla \mathrm{x} E = 0 \qquad (2.\ 33)$$

$$\nabla.\,j + \frac{d\rho_q}{dt} = 0 \qquad (2.\ 34)$$

Where, ρ_q is the volume charge density and j is the electric current. The electric current j

can be given by conduction current ($\sigma_m E$) and convection current ($\rho_q v$), where v is the

32

fluid velocity [113]. The convective current is negligible in the system considered here. The Equations (2. 32)-(2. 34) can thus be written as,

$$\nabla.\big((\sigma_m + i\omega\varepsilon_m)E\big) = 0 \qquad (2.35)$$

Electric field E can be written in terms of E_0 which is the applied field and E_1 which is the perturbation field where, $|E_1| <<< |E_0|$. Which modifies Equation (2. 35) as,

$$\nabla\sigma_m.E_0 + j\omega\nabla\varepsilon_m.E_0 + \sigma_m\nabla.E_1 + j\omega\varepsilon_m\nabla.E_1 = 0 \qquad (2.36)$$

For an applied AC voltage, the non-zero electrical force f exerted on the media is,

$$f = -0.5\left[\left(\frac{\nabla\sigma_m}{\sigma_m} - \frac{\nabla\varepsilon_m}{\varepsilon_m}\right).E_0\frac{\varepsilon_m E_0}{1 + (\omega t)^2} + 0.5|E_0|^2\nabla\varepsilon\right] \qquad (2.37)$$

Where t is the charge relaxation time of the liquid. The first term in Equation (2. 37) is the Coulomb force and the second term is the dielectric force. In certain frequency ranges either the Coulomb force or the dielectric forces dominate [113]. The frequency where this behavior changes is of the order of the inverse of charge relaxation time ε_m/σ_m. These forces can cause motion of fluid across the electrodes. This behavior was not observed during experiments in this work, due to the low conductivity of the media and is neglected in the numerical analysis.

The use of electric field in the domain results into power generation in the domain, which is dissipated in the channel in the form of heat. The order of magnitude comparison of increase in temperature with electric field is given by Equation (2. 38),

$$\Delta T \approx \frac{\sigma_m V_{rms}^2}{k} \qquad (2.\,38)$$

Where, ΔT is the rise in temperature, V_{rms} is the voltage applied to the device and k is the thermal conductivity of the medium. For the device in consideration, the conductivity is around 10^{-3} S/m and for water, k is around 0.6 J/m. The V_{rms} is about 7 V. Thus the ΔT value is around 0.2°C and can be neglected [114].

Application of a voltage can cause appearance of charges at the electrode-electrolyte interface. This modifies the charge density in the electric double layer. For the frequency below the relaxation frequency, the on the electrode and in the double layer will alternate in each half cycle of the applied field. This can cause fluid movement into steady counter rotating vortices. Most applications of electro osmosis exist in low frequency domains (~1 kHz) [115]. The electroosmotic velocity for the low conductivity medium and high current frequency (`100 kHz) used here is negligible.

When a cell is exposed to an external electric field, the transmembrane potential is induced in the cell. Generally, if the transmembrane potential is higher than about 1 V, the cell membrane is permeable to an outside medium. With the increase in applied potential, the membrane can be disrupted irreversibly [116]. The cell membrane potential for a spherical particle is calculated using the Equation (2. 39),

$$V_m = \frac{1.5 E r_p \cos \alpha}{\sqrt{1 + (2\pi f \tau)^2}} \qquad (2.\,39)$$

Where, $\tau = r_p C_{mem}(\frac{1}{\sigma_{cyto}} + \frac{1}{2*\sigma_{medium}})$, V_m is the cell membrane potential, E is the

applied electric field, α is the angle between the field line and a normal from the center of

the particle to a point of interest on the membrane. In this work α equals 0° to account for

maximal trans-membrane potential, σ_{cyto} is the conductivity of cytoplasm, σ_{medium} is the

conductivity of the suspending medium and C_{mem} is the capacitance of the cell

membrane.

2.4 Computational model

In this work, COMSOL Multiphysics is used for computation on the Windows 7

Enterprise 64-bit operating system with 32GB RAM and Intel® Xeon ® CPU E5-1650

v2 @ 3.50 GHz processor by using the Electric Currents and Laminar Flow Modules. A

model is developed for the microchannel in consideration by solving the Navier Stokes

Equation along with continuity equation for laminar, steady flow in the channel

(Equations (2. 19)-(2. 20)). The electric field in the channel is computed by solving

Maxwell's equations for electric field at steady state ((2. 32)-(2. 34)).

2-dimensional as well as 3-dimensional models are used for simulations in this work.

Chapter 4 uses a 3-dimensional model, where the channel is modelled as a rectangular

block and electrodes are modelled as pockets. The material specified to the block is

water. The normal inflow velocity of the fluid entering the domain is presented as the

inlet condition ($velocity\ u = u_0 \hat{n}$). The atmospheric pressure is provided as the

maximum pressure at the outlet condition for the channel ($\overline{p_0} \le atm$). The side walls and

the top and bottom walls of the channel have no slip boundary condition ($velocity\ \bar{u}=0$).

The pockets representing the electrodes are also assigned no slip boundary condition. To solve the for the electric currents domain, the inlet and outlet and channel walls are specified as insulating boundaries ($\hat{n}.\bar{J} = 0$). Alternate electrodes are specified with a constant voltage corresponding to the *Vrms* voltage for the AC current applied. Alternate electrodes are grounded. In case of the 2-dimensional model used in Chapter 5, similar conditions are used, except that the electrodes are modelled as holes. The flow velocity at inlet is calculated by considering a 2-dimensional domain with 100 μm as the height of channel. This value of height is selected as it corresponds to the experiments.

In case of the two-dimensional model, the electrodes are modelled as holes.

The three dimensional model uses tetrahedral mesh elements with boundary-layered mesh along the channel edges and electrode surfaces. The grid independence study was conducted to determine the maximum element size that can be used. In this study, the velocity and electric field profile were plotted for an arbitrary line in the domain between two electrodes. The profile obtained did not show any change with the change is mesh size. Secondly, two arbitrary probe points were selected in the channel domain and the electric field and velocity was computed for these points. The change in velocity value shown by these points was smaller than the relative tolerance (set to 0.01 for velocity and 0.0003 for electric field) set for the model when the mesh element size was smaller than 15 μm. Thus, this was selected as the maximum element size for the mesh.

Finite element method based solver with first order discretization for fluid flow and quadratic discretization for electric field is used with the relative convergence error of

0.0001. The model was used to compute the value of electric field and flow field in the channel domain. Presence of particles was not considered to track the particle trajectories, instead, the particles were treated as points and the value of particle velocity was calculated using Equation (2. 30) . Model Specific details are given in Chapter 4 and Appendix B.

CHAPTER THREE

STUDY OF SHRINKAGE DURING PYROLYSIS OF SU-8 PHOTORESIST

(Natu, Rucha, et al. "Shrinkage of SU-8 microstructures during carbonization." *Journal of Analytical and Applied Pyrolysis* 131 (2018): 17-27)

3.1 Introduction:

SU-8, a negative photoresist, is a carbon precursor that is widely used in the fabrication of carbon microstructures using the C-MEMS technique. Once fabricated, the SU-8 microstructures are pyrolyzed, or heat treated in an inert atmosphere, to derive glass-like carbon as explained in Section 1.2.3 of Chapter 1 [117–119]. As expected, the SU-8 original shapes shrink during carbonization. This shrinkage has been shown to be reproducible for specific dimensions of the precursor SU-8 structure and the carbonization protocol [57]. Hence, once shrinkage is characterized one may implement a production process. However, there are no guidelines for the *a priori* design of carbon microstructures. To this end, here the focus is on elucidating the impact of 1) heating protocol and 2) geometry and shape of the SU-8 precursor on the shrinkage of SU-8 microstructures during carbonization.

SU-8 shrinkage was initially reported when studying films. Previous works reported a slight increase on shrinkage as the temperature increased from 600 to 1000˚C [120,121]. The effect of pyrolysis atmosphere was studied by Ranganathan et al, who reported that vacuum produces the least shrinkage, while nitrogen generally produced the most shrinkage. These authors also showed the shrinkage to depend on temperature [122]. The

reported studies characterizing shrinkage of SU-8 microstructures are few; although different authors have reported a strong and repeatable dependence of the shrinkage of cylindrical structures on the structure height and aspect ratios of the SU-8 precursor [56,57,60,123–127].

The aim of this chapter is to elucidate the dependence of shrinkage on the dimensions and shape of the precursor, as well as pyrolysis conditions. Statistical analysis based on Analysis of Variance test (ANOVA) with the p-value 0.01 and Tukey's Honest Significant Difference test (HSD) for comparison of shrinkage for multiple parameters is used to study different posts. The goal is to advance the understanding of shrinkage of SU-8 microstructures and enable a design tool for 3D carbon microelectrodes. This is important given the number of demonstrated and potential applications of carbon microstructures derived from SU-8.

3.2. Materials and Methods

3.2.1 SU-8 Photolithograpy

SU-8 (Gersteltec, Switzerland) microstructures of different cross sections (circle, square, triangle and hexagon), nominal height H (10, 50, and 100 µm) and characteristic dimension D (10, 20, 30, 40, 80 and 160 µm) were fabricated as detailed in Table 3. 1. Cylindrical posts with varying characteristic dimension with a set height of 300 µm were obtained from a previous project [128]. The fabrication of all these structures on a silicon/silicon oxide substrate was optimized (data not shown) and detailed in Table 3. 2.

3.2.2 Pyrolysis protocol
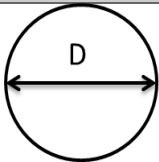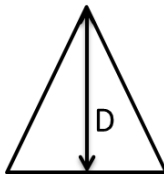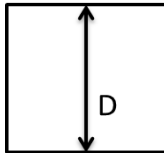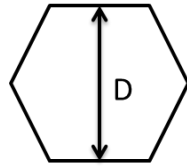
The SU-8 microstructures were pyrolyzed in an inert atmosphere using a quartz tube furnace (TF1400 Across International, New Jersey, USA). The details of the carbonization protocols are summarized in

Table 3. **1**. The carbonization protocol featured five stages: (i) heating from room temperature to 300˚C with a heating rate of 5 °C/min; (ii) a dwell time of 30 minutes at 300 °C to allow for residual oxygen to be evacuated from the chamber; (iii) a temperature ramp from 300 °C to the final temperature with a specific heating rate; (iv) a dwell at the final temperature to complete carbonization; and (v) cooling to room temperature with a cooling rate of 5 °C/min. The heating rates in step (iii) were varied from 2, 5 to 10 °C/min to study the effect of heating ramp on shrinkage. Final temperatures in step (iv) were 600 °C, 900 °C and 1150 °C. In order to study the effect of dwell time, time of 0, 1.25, 6 and 12 hours was used at 900 °C. The effect of heating atmosphere was investigated by using vacuum (pressure = -762 torr =-30 in of Hg) or nitrogen atmospheres (760 torr (29.92 in of Hg) at a flow rate of 0.005 m^3/min in a tube furnace of 140 mm inside diameter) at 900 °C. In this study 900°C was used as the pivot final temperature given the wide application of carbon structures obtained at this temperature [123,124,129–131]. Thermogravimetric analysis (TGA) was conducted for SU-8 posts using a TGA Q5000 system (TA Instruments, Delaware USA). The sample was heated in a nitrogen environment at 5°C/min initially to the temperature of 300°C, where it was held constant for 30 minutes, and further to the temperature of 1000°C, where it has held

for 75 minutes before cooling down naturally. Due to system limitation, the temperature could not be increased beyond 1000°C.

In **Table 3. 1**, the geometry section details the different shapes used in this work as well as their dimensions. The pyrolysis section summarizes the values tested for different process variables. The first step during spin coating was used to coat the substrate with photoresist. The thickness of the layer was obtained thanks to the speed and spin time used in step 2.

Table 3. 1 Details of geometry and pyrolysis variables

Parameter	Value
Geometry	
Shape	Circle Triangle Square Hexagon
Height, *H* (µm)	10, 50, 100, 300
Characteristic Dimension, *D* (µm)	10, 20, 30, 40, 80, 160
Pyrolysis	
Temperature (°C)	650, 900 and 1150
Atmosphere	Nitrogen(760 torr) and Vacuum (-762 torr)

Heating Rate (°C/min)	2, 5, 10
Dwell Time (hours)	0,1.15, 6, 12

*Notes: rpm= revolutions per minute, PEB= post exposure bake, PGMEA= Propylene glycol methyl ether acetate, HC=hard contact, SC= soft contact, Cyl= cylinder

Table 3. 2 Photolithography parameters to fabricate cylindrical posts of SU-8.

Height of Post (µm)	Shapes	Type of SU-8	Spin Coating			Soft Bake at 95 °C	Exposure (mJ/cm2)	PEB * at 95 °C	Develop (min)
			Step	Speed (rpm*)	Time (s)				
10	Cyl	GM 1060	1	500	5	30 min	225 (HC)	20 min	3
			2	2500	40				
50	Cyl	GM 1075	1	500	5	45 min	165 (HC)	35 min	6
			2	3000	100				
50	All shapes	GM 1075	1	1700	100	At 90°C - 30 min and at 130°C -15 min	200 (SC)	25 min	6
			2	2700	For edge bead				

100	Cyl	GM 1075	1	500	5	45 min	195 (HC)	35 min	8
			2	1700	100				

3.2.3 Structure characterization

The characteristic dimension D of the SU-8 and carbon structures were analyzed using optical microscopy (Nikon Eclipse LV100) and the native Nikon NIS Elements BR software. The characteristic dimension was measured at the top surface of the structure. The nominal height H was measured using a surface profilometer (Tencor Alpha Step 200) as the difference between the height of the wafer and the elevation at the center of the structure. The tip radius of the probe of the profilometer was 1.5 µm and the resolution of this instrument as reported by the manufacturer was 5 nm in the micron mode. Height was also measured at the edges of the structure and was used for characterizing the sagging behavior of the structure. Sagging is essentially the difference between the structure height at the center and at the edges of the top surface. At least 8 structures were measured for each data point reported in the results section (n=8). The maximum standard deviation from these measurements was 1.5 µm for lateral and 1.8 µm for height measurements.

Such measurements allowed for the calculation of surface area, volume, and aspect ratio (H/D) for all structures before and after pyrolysis. The surface area was calculated as the sum of the top and the lateral surfaces, which are the only ones available for degassing. Hence, the surface area of the structure that is attached to the substrate was not considered.

3.2.4 Data Analysis

The percent shrinkage was calculated using Equation (3. 1), where the dimension can be either the height or diameter of the microstructure. The reported data points are the average values of at least 8 measurements. Standard deviation is reported as the error.

$$\% \ Shrinkage \qquad\qquad (3.1)$$

$$= \frac{Dimension \ before \ pyrolysis - Dimension \ after \ pyrolysis}{Dimension \ before \ pyrolysis} * 100$$

A surface area ratio (*SAR*) was defined using Equation (3. 2). *SAR* is necessary since neither the characteristic dimension *D* or height *H* is enough to characterize the surface area of a structure. Furthermore, the *SAR* used here for all microstructures considers the surface area that is available for degassing. Hence, the surface of the structure on direct contact with the substrate was not considered.

$$Surface \ Area \ Ratio \ (SAR) = \frac{Lateral \ Surface \ Area}{Top \ Surface \ Area} \qquad\qquad (3.2)$$

The factors considered here for the study of shrinkage were the *SAR*, shape of cross section, temperature of pyrolysis, pyrolysis atmosphere, heating rates and dwell times of the pyrolysis process. A statistical analysis based on Analysis of Variance (ANOVA) and Tukey's honest significant difference (HSD) test was performed to determine the impact of each of these factors on shrinkage. The procedure is explained in Appendix A. Briefly, ANOVA was used here to determine the contribution of different parameters for shrinkage of the same structure. If results of ANOVA indicated that the

considered factor, for example pyrolysis temperature, affected the shrinkage of the posts, then the shrinkage obtained at different temperatures was analyzed using Tukey's HSD. Tukey's method provided the tools to identify which temperature from the analyzed values gave a statistically different shrinkage value.

Three categories of *SAR* were used and one ratio in each category was selected. The categories used were a low value of *SAR* (<1), representing a short structure; a high *SAR* (>10), representing a tall structure; and an intermediate SAR. For example, the SAR values 0.60, 2.57 and 12.49 were selected in the three categories for the study of dwell time. It is important to note that different shapes did not have the exact same *SAR* values. Hence, the closest possible values between them were selected for analysis. For example, structures with cross section of hexagon with the *SAR* value of 2.15±0.84, square with *SAR* value of 1.87±1.07 and circle with *SAR* value of 1.80±0.23 were grouped together.

3.3. Results and discussion:

3.3.1 SU-8 Photolithography

The results from the fabrication of SU-8 microstructures are shown in Figure 3. 1 when plotting the designed vs. the fabricated aspect ratio. The structures were fabricated as designed as long as the aspect ratio (AR) was less than 6. Posts with square cross section were fabricated slightly bigger than fabricated at AR values between 6 and 10. In contrast, circular posts were fabricated slightly smaller than designed in this same range; triangles and hexagons display a significant deviation. At AR>12, the deviation between designed and fabricated is rather significant for hexagons and circles. These fabrication

results were obtained using the optimized parameters of Table 3. 2. It is assumed that the SU-8 microstructures fabricated here were fully cross-linked. This is an important assumption since partially cross-linked SU-8 structures have been shown to deform during heat treatment.[132] Further photolithography optimization is necessary for structures with AR>12, but this is out of the scope of this paper. The dimensions of SU-8 microstructures used in the rest of this current work were those of the fabricated structures.

3.3.2 Dependence of shrinkage on geometry:

Examples of carbon structures obtained from SU-8 are shown in Figure 3. 1. Note that the shrinkage was not uniform throughout the height of structures. A curvature at the base of all structures resulted because the SU-8 structure was well adhered to the substrate, which restricted shrinkage at the base. This curvature exists in the region within 10 um from the substrate and had been reported by us and other authors before [67,129,133]. This curvature is expected to change according to the choice of substrate due to the difference between the coefficient of thermal expansion of the substrate and the morphing material from SU-8 to carbon. This curvature disappears when carbonizing free-standing SU-8 structures[134]. After this curvature, the profile is uniform throughout the height of the structure. Sagging on the top surface was also detected and is discussed below. Connecting wires between structures can be seen in some cases, which result when the gap between structures is small and exposure dose is optimized [135].
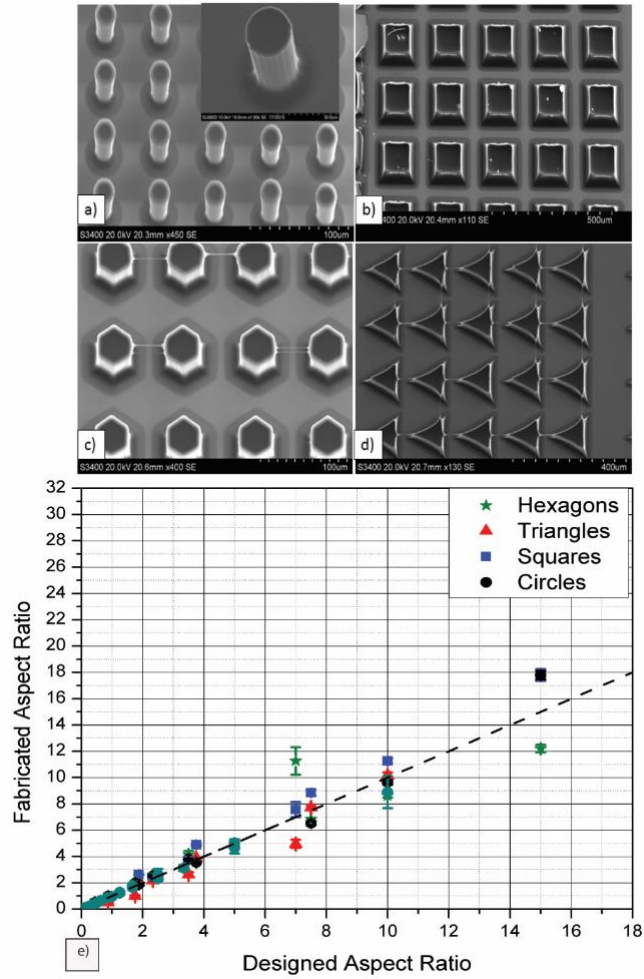
Figure 3. 1 Carbon structures with obtained by SU-8 photolithography followed by pyrolysis. Carbon structures with (a) circular, (b) square, (c) hexagonal and (d) triangular cross section. The base of the structures featured a curved profile (insert Figure 3. 1 A). (e) Results for fabricated aspect ratio in comparison to designed aspect ratio for different structures.

3.3.2.1 Effect of Surface Area Ratio (SAR)

The percent shrinkage of the characteristic dimension D for cylinders with respect to the logarithm of *SAR* is shown in Figure 3. 2a. Low values of log (*SAR*) denote

structures with low aspect ratio. In this case, shrinkage in H (Figure 3. 2b) is considerably

higher than shrinkage in D. This is because degassing occurs mostly through the top

surface. A similar trend was observed in previous works where a low shrinkage in

linewidth and a high shrinkage in thickness was seen for low aspect ratio structures and

films [120,136–138] As the *SAR* value increases, the shrinkage in H decreases and the

shrinkage in D gradually increases. The solid vertical line marked in Figure 3. 2a-c

indicates the SAR value of 1. At this line, the lateral and top surface areas are equal.

Beyond this, the lateral surface area becomes dominant. As the *SAR* value increases

further, the lateral surface area becomes excessively dominant for degassing. Hence, the

lateral surface area becomes the preferred path for degassing, which results in a gradual

increase of the shrinkage of D. With an increase in *SAR, the* top surface area plays a

secondary role in degassing thus resulting in the gradual decrease of shrinkage of H.

Curve fitting was employed to derive relations that describe this behavior for D and H.

Equations (3. 3) and (3. 4) offer a quantitative relation between *SAR* and percentage

shrinkage in D and H respectively. For *SAR* values greater than the studied values, the

shrinkage in D is expected to increase gradually and the shrinkage in case of H is

expected to decrease gradually.

Based on the trend observed in Figure 3. 2c it can hypothesized that shrinkage in

D for lower values of log (*SAR*) than those shown here will further reduce, and the

shrinkage of H will gradually increase. Such behavior is similar to that seen in the case of

thin SU-8 films.[120]. These results might differ slightly depending on the SU-8

manufacturer, but the trend reported here is expected to be the same. This expectation is based on previous observations with SU-8 procured from MicroChem [57].

% Shrinkage in D   (3. 3)

$$= (51.28 \pm 1.32) - (16.61 \pm 2.14) * \exp(\frac{\log(SAR)}{-(0.46 \pm 0.07)})$$

% Shrinkage in H   (3. 4)

$$= (50.73 \mp 1.88) + (19.98 \mp 2.22) * exp(\frac{log(SAR)}{-(0.47 \pm 0.08)})$$

3.3.2.2 Effect of shape

The shrinkage in *H* and *D* for the different shapes was characterized. Results are presented in Figure 3. 2a and b for *H* and *D* respectively. Results from Amato et al [123] who characterized the shrinkage of cylinders with 1.4 μm diameter and 11 μm height are also plotted.

Tuckey's test analysis for selected shapes (marked by blocks in Figure 3. 2a,b) indicates that the shrinkage for different cross sections does not show a statistically significant difference as long as the *SAR* is similar. Thus, the cross sectional shape was not seen to play a role in determining the shrinkage for posts. Equation (3. 3) for percent shrinkage in *D* and Equation (3. 4) for percent shrinkage in *H* are valid for the shapes considered in the range of area ratios plotted in Figure 3. 2.
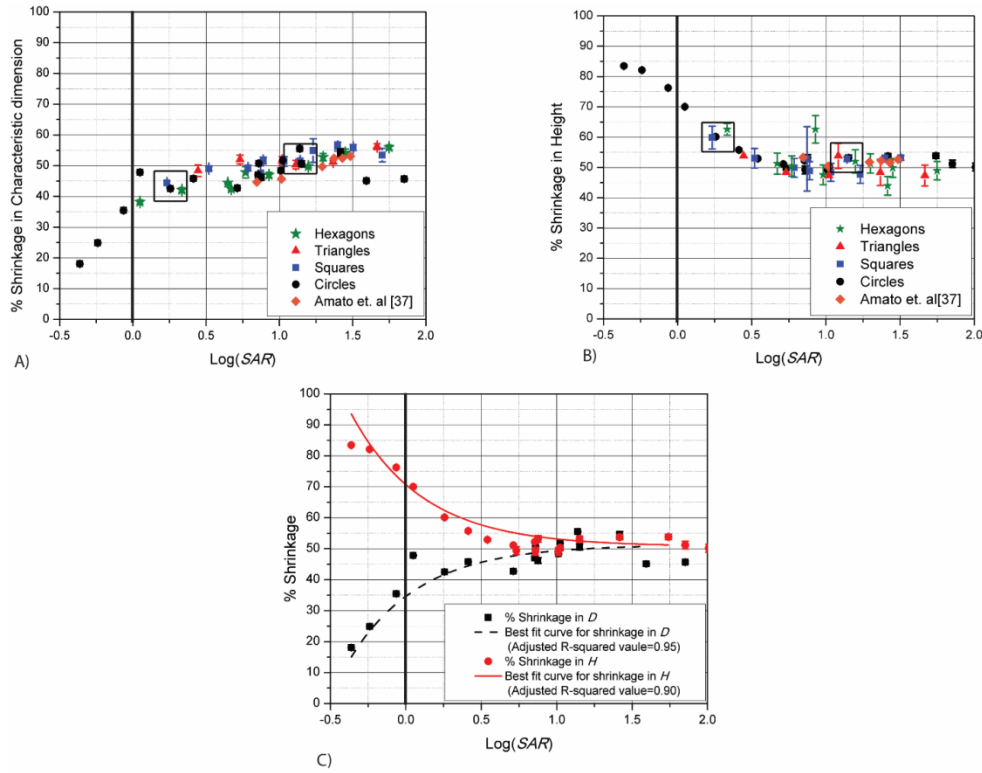
Figure 3. 2 The effect of shape on shrinkage during carbonization. a) The plot shows the shrinkage in characteristic dimension D for posts with different cross sections. The blocks show the points that were studied in the statistical analysis. b) This plot shows the shrinkage in height for different cross sections: hexagons, squares and triangles as superimposed on the graph for shrinkage in height in case of cylinders. c) The plot shows the variation of diameter and height for the cylindrical posts with respect to the logarithm of SAR. The shrinkage in diameter increases with the increase in the ratio and the shrinkage in height decreases with the increase in ratio.

3.3.2.3 Sagging on top surface of carbon structures

Sagging at the top surface was observed on carbonized structures as shown in Figure 3. 3a, b, c. Such sagging was not observed in the SU-8 structures. The edges of

50

short carbon posts are seen to protrude compared to the central region of the top surface. The dependence of sagging on the top surface area for different shapes and as percentage of H after pyrolysis (nominal height) for varying log (SAR) are plotted in Figure 3. 3 d and e respectively. Height measurements were done with a Tencor Alpha Step 2 featuring a tip radius of 1.5 um and expected resolution of 5 nm in micron mode. Sagging increases with the top surface area for any given shape, i.e. circles, triangles, squares. Sagging decreases as log(SAR) increases. Since SAR is proportional to the aspect ratio, sagging decreases with an increasing aspect ratio. We hypothesize that the sagging phenomena occurs due to the residual stresses developed in the sample during degassing. Such phenomena is observed during shrinkage at different instances with polymers [139,140]. Residual stresses appear as tensile forces at the surfaces of the structure as it attempts to shrink. Similar behavior is also observed in other polymers during shrinkage [141,142].

For a SAR<1, the top surface area is larger than the lateral surface area and degassing primarily happens through the top surface. Hence, residual stresses will primarily appear at the top surface, resulting in increased sagging at the top surface. For structures with SAR >1, degassing primarily happens through the lateral surface area, leading to decreased sagging on the top surface.

In the case of cross sections containing vertices such as squares, hexagons and triangles, it is hypothesized that the stress develops at these vertices along with the edges. Because of this, the region near the vertices shrinks at a different rate than the edges and the center of the structure. The center develops sagging, whereas the vertices look protruded compared to the edges. For example, in the case of a post with triangular cross

51

section, the top surface shows three different height levels. As the structure shrinks, the central region develops sagging. The edges also show sagging (~1μm) as compared to the vertices. This indicates that the center, edges and vertices all shrink at different rates.

An empirical relation to predict the sagging as a percentage of nominal height was obtained using curve fitting and presented here as Equation (3. 5). This equation is valid in the range of SARs studied in this work.

$$\text{Sagging as a percentage of nominal height} \qquad (3.5)$$

$$= 56.92 * \exp\left(\frac{-\log(\text{SAR})}{0.60}\right) - 21.22$$

3.3.3 Dependence of shrinkage on pyrolysis conditions:

3.3.3.1 Final temperature

It is known that carbonization of an organic polymer occurs in several stages [143–146]. For most bulk materials, the initial stage is the dehydration and elimination of halogens below 500° C. Above 500°C, hydrogen, oxygen and nitrogen are eliminated and the coalescence of polymer chains results in volume shrinkage. Above 800°C, pores in the structure gradually disappear and aromatic networks are interconnected. Annealing above the temperature of 1200°C allows for the gradual elimination of any structural defects, the elimination of the last vestiges of hydrogen, and the evolution of any further impurities [57,143,147]. Thus, the primary shrinkage due to degassing of volatile products other than hydrogen compounds happens at temperatures around 600°C. After

this temperature, the shrinkage can be attributed to condensation of aromatic chains, pore closing and removal of hydrogen.
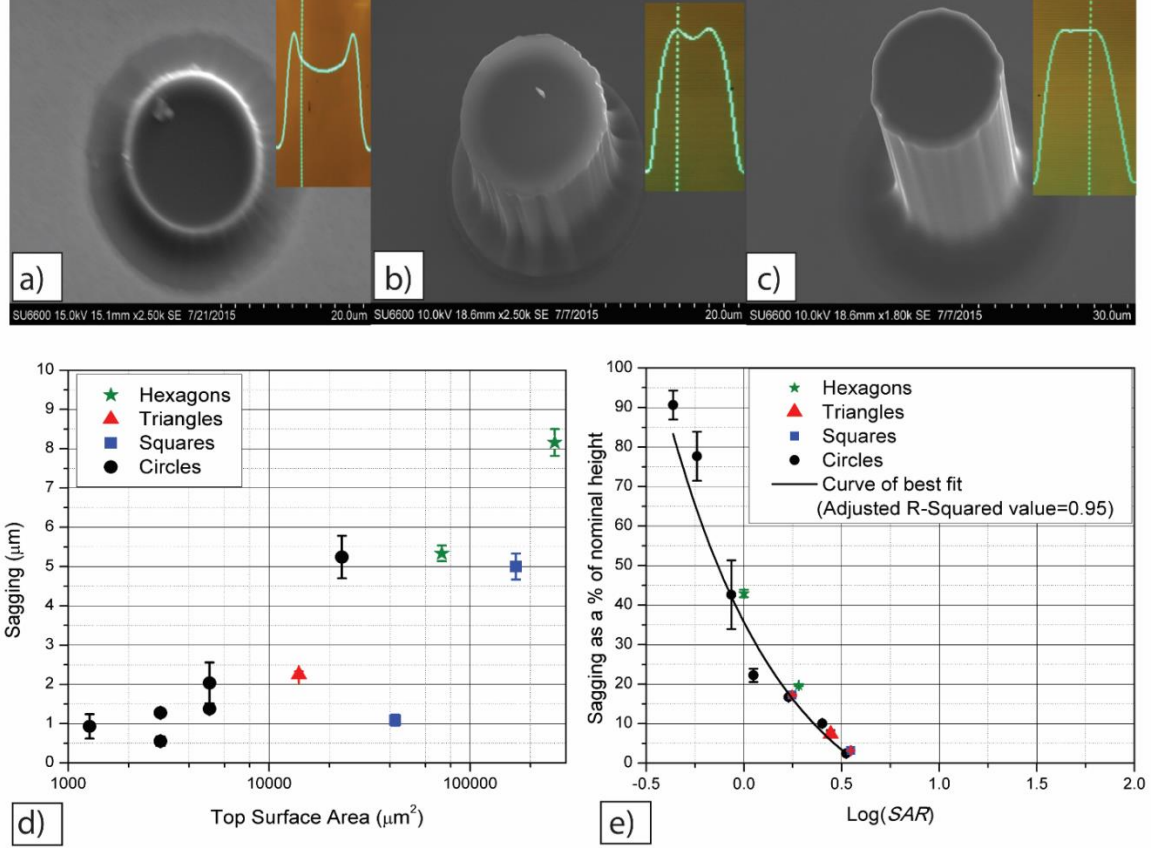
Figure 3. 3 Sagging obtained during pyrolysis. a)-c)Cylindrical posts with height 10 μm, 50 μm and 100 μm after pyrolysis are shown in the figure with corresponding post profile. The inset figures show the height profile measured by the profilometer. d) The plot shows the sagging obtained for different structures as a function of top surface area. e) The graph shows the sagging caused in the top surface of the posts as a percentage of the post height.

The shrinkage that results when heating SU-8 microstructures with different SARs to different final temperatures in the range 650-1150°C is shown in Figure 3. 4a

and b. Low aspect ratio structures shrink more in their H than on their D. Shrinkage of both H and D seems to slightly depend on heating temperature. The ANOVA test for different temperatures proved that the difference between shrinkage at different temperatures was statistically significant. This prompted us to perform the Tuckey's test on the data set to find out which temperature resulted in a different shrinkage. The data points used are enclosed by the rectangles shown in Figure 3. 4a and b. Tuckey's test indicated that the average shrinkage differed for all the three temperatures. Hence, shrinkage shows a dependence on final pyrolysis temperature.

The rate of change of shrinkage for selected SARs is shown in Figure 3. 4 c. The slopes of the different curves are similar. However, the shrinkage in H for SAR=0.57 is much higher than shrinkage of D of the same structure. As the SAR value increases, the shrinkage in H and D show a similar value. Irrespective of the SAR value, the rate of change of shrinkage with respect to temperature is similar for all the considered SARs. Thus, the effect of temperature is independent of the SAR value. As temperature increases, shrinkage of the structure occurs due to interconnection of aromatic rings and removal of the last vestiges of gases. The slope for the increase in shrinkage from 650°C to 1150°C is around 0.01%/°C. Hence, by knowing the shrinkage at the temperature of 900°C (Equations (3. 3) and (3. 4)) and considering the slope of the curve in Figure 3. 4c, the shrinkage at other temperatures in the range 650-1150°C can be predicted. The average increase in shrinkage when using temperatures between 650-1150˚C for all SARs tested here was 3.45±0.93 % in diameter and 4.92±1.17% in height. The TGA results (Figure 3. 4d) show a rapid weight loss occurring at the temperature of 300°C, where the

temperature is held constant for 30 minutes. This can be related to the weight loss

occurring due to the complete evaporation of the solvent. The weight loss between

300°C to 600°C can be attributed to the elimination of halogens followed by nitrogen,

hydrogen and oxygen as discussed previously. Beyond 600°C, the weight loss becomes

gradual to the temperature of 800°C. Beyond this temperature, the weight loss decreases

further due to the elimination of hydrogen and the formation of interconnects in the

aromatic structure. These results are similar to results by previous works [121,132,148].

This shows that the increase in shrinkage in diameter and height are comparable

and do not depend on the SAR.

3.3.3.2 Dwell time at final temperature

Dwell time refers to the time the sample is maintained at the final temperature.

Different dwell times (0, 75 min, 6 and 12 hours) were tested when carbonizing

cylindrical structures at 900 ˚C. Dwell times do not show a statistically valid change in

shrinkage (Figure 3. 5d); indicating that increasing the carbonization time does not have

an effect on shrinkage. Previous work by Mardegan et al reported that the increase of

dwell time from 1 hour to 4 hours resulted in about 10% higher weight loss at 800 and

900°C [138]. A corresponding change in dimensions was not observed in here. Further

work is required to draw more conclusions on the effect of dwell time.
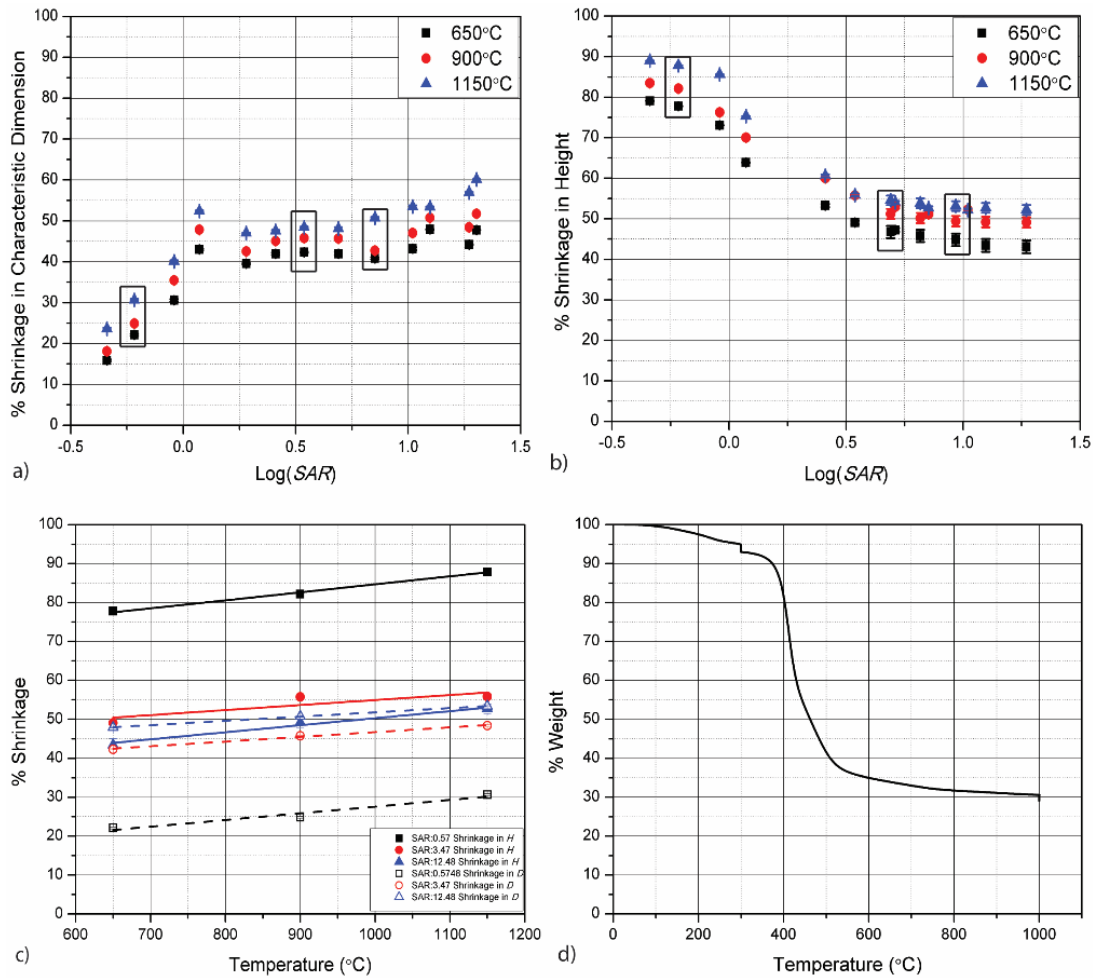
Figure 3. 4 Effect of temperature on shrinkage a) The figure shows the diametrical shrinkage in cylindrical posts for the pyrolysis temperature of 650, 900 and 1150˚C. b) The shrinkage in height for cylindrical posts pyrolysed at different temperatures is shown in this figure. c) The plot for percent shrinkage in diameter (a) and percent shrinkage in height (b) with respect to the change in temperature indicates a gradual increase in the shrinkage. The rate of increase in shrinkage or the slope of the graphs remains same with the change in *SAR* as shown in the figure. d) TGA results showing the weight loss as temperature increases.

3.3.3.3 Heating rate

Three different heating rates were implemented in order to elucidate the dependence of shrinkage on heating rate. Results are shown in Figure 3. 5c when carbonizing cylindrical posts. Tuckey's test concluded that varying the heating rate between 2, 5 and 10 °C/min did not yield a statistically valid impact on shrinkage. Hassan et al reported an increase on shrinkage of around 10% when carbonizing SU-8 polymer at 50 °C/min [149]. Sharma et al reported that an increase on heating rate up to 15° C/min leads to the formation of micropores in the carbon structures. The pore size found at the heating rate of 90°C/min is around 10-15 µm[150]. The internal structure of the carbon cylinders by fabricating in-situ cross sections of the different carbon structures obtained from SU-8 using ion milling (Focused Ion Beam, nanoDUET NB5000, Hitachi) was studied. However, it did not show any micropores in the carbon sample derived at a heating rate of 10 °C/min using electron microscopy at magnification 40k.

3.3.3.4 Pyrolysis atmosphere

It is hypothesized that shrinkage would depend on the evacuation of byproducts from the sample and the heat transfer coefficient of the atmosphere. The byproducts of carbonization would diffuse from the core of the structure to its surface, and such transport would be enhanced by implementing a low pressure environment in the tube [151]. The ability of the gas to conduct the heat to the sample also plays an important role in formation of byproducts and consequent degassing [152]. Previous studies of the pyrolysis of positive photoresist AZ4430 indicated that the shrinkage in the vacuum environment was less than in nitrogen environment due to presence of traces of oxygen in

the furnace environment and that this difference increased with the temperature [122]. Lyons et al. compared the shrinkage of HPR-206 photoresist in pure H2 and pure N2 atmospheres. The use of an hydrogen atmosphere resulted in about 10% more shrinkage [137]. Based on the values of thermal conductivity and viscosity for Nitrogen and Hydrogen [153–156], the heat transfer coefficient for Nitrogen and Hydrogen was compared. Hydrogen has a higher heat transfer coefficient than nitrogen resulting into higher amount of heat transferred to the sample. Hydrogen also provides a reducing environment for pyrolysis which results in degassing of more carbonaceous material than with nitrogen atmosphere and results into higher shrinkage [157].

The results when characterizing shrinkage for different SARs depending on the tube atmosphere during carbonization are shown in Figure 3. 5a-b. The use of vacuum during carbonization yielded a higher shrinkage than when using a nitrogen atmosphere. This difference is statistically valid as determined using ANOVA. The geometry of the structure still plays a significant role, as shown by the different shrinkage of D and H in low aspect ratio structures with log(SAR)<1. The increase in the shrinkage of D for a given SAR between the two atmospheres is 5.37±1.24 %, whereas the shrinkage in H only increases by 2.26±0.81%. This indicates that a change in pyrolysis atmosphere has a greater effect on the lateral shrinkage compared to the vertical shrinkage.

In the case of a vacuum environment, the pressure is expected to be lower than in the case of nitrogen environment. At low pressure, we expect enhanced diffusion of volatile byproducts. In a study for thermal degradation of polyethylene under vacuum and nitrogen environment with 787 torr (31 inches of Hg) pressure, it was observed that the

vacuum produces volatiles which are about ten times heavier, indicating that the volatilization is higher in vacuum environment [158]. The formation of volatile byproducts in vacuum also occurs at a temperature lower than in the case of nitrogen [127,159]. Thus, it is expected that the formation of volatiles occur at an earlier stage with a vacuum environment. In case of high pressure in the furnace, the rise in temperature can increase the formation of volatile components. This is evident from the fact that the shrinkage in nitrogen environment increases with increase in temperature. Other authors reported on the effect of pressure on shrinkage when carbonizing different materials. For example, the pyrolysis of bituminous coal in nitrogen atmosphere at high pressure resulted in a decrease of the yield of volatiles [160]; pyrolysis of biomass chars also show evidence of low degassing at high pressure [161]; while a study on the thermal decomposition of polyethylene showed an evidence for decrease in volatiles with increase in furnace pressure [162].

3.3.4 A proposed curve fit to predict shrinkage

The results show that SAR is the most important factor in determining the shrinkage of the SU-8 structure. The final temperature and atmosphere during carbonization also play a role.

Below reported are three relations that can help in the design of SU-8 structures that will be carbonized. Equations (3. 6)-(3. 8) help calculating the percent of shrinkage in characteristic dimension and height, as well as the total height of the carbon posts when taking sagging into account. These equations apply when using process temperature T between 650 °C to 1150 °C in a nitrogen environment.
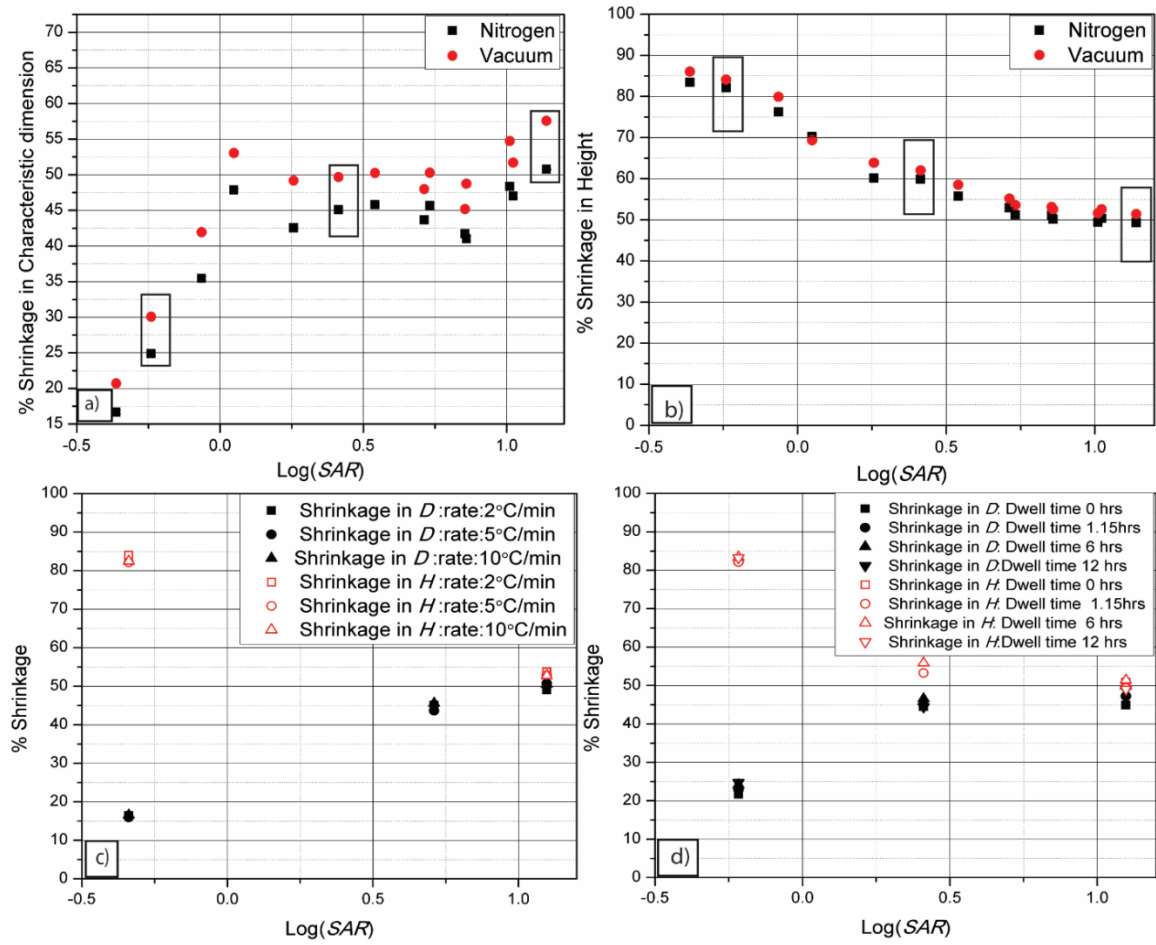
Figure 3. 5 Dependence of shrinkage on atmosphere. a-b) Dependence of shrinkage on

pyrolysis atmosphere for the shrinkage in diameter and height of the structure are shown

in the figures. The shrinkage for vacuum and nitrogen atmosphere show a similar trend,

but the shrinkage in vacuum shows a higher value, especially for diametrical shrinkage.

c) The cases selected for statistical analysis for heating rates 2, 5 and 10˚C/min is shown

in the figure. These heating rates do not show statistically significant effect on the

shrinkage. d) The cases selected for statistical analysis for dwell times of 0, 1.15 hours, 6

hours and 12 hours during pyrolysis indicate that the shrinkage does not change with the

dwell time.

% Shrinkage in characteristic dimension D = $\qquad$ (3. 6)

$$51.28 \pm 1.32) - (16.61 \pm 2.14) * \exp\left(\frac{\log(\text{SAR})}{-(0.46 \mp 0.07)}\right) - 0.01$$

$$* (T - 900°C)$$

% Shrinkage in H $\qquad$ (3. 7)

$$= (50.73 \mp 1.88) + (19.98 \mp 2.22)$$

$$* \exp\left(\frac{\log(\text{SAR})}{-(0.47 \mp 0.08)}\right) - 0.01 * (T - 900°C)$$

Sagging of posts as a percentage of nominal height at different temperatures,

Sagging as % of nominal height = $\qquad$ (3. 8)

$$56.92 * \exp\left(\frac{-\log(\text{SAR})}{0.60}\right) - 21.22 - 0.01 * (T - 900°)$$

For calculations of shrinkage, using vacuum during carbonization, a factor of 5.37±1.24 % must be taken into account for characteristic dimension (Equation (3. 6)); and a factor of 2.26±0.81% for height to the total shrinkage in H (Equations (3. 7) and (3. 8)). For example, if the SAR value of the structure is 1.80, the shrinkage in D at the temperature of 650°C in nitrogen atmosphere can be calculated by Equation (3. 6) as 39.22±3.32% and shrinkage in H is 57.37±1.98% using Equation (3. 7). For a vacuum atmosphere, the

corresponding shrinkage in D will be 44.59±4.56% and shrinkage in H will be 59.63±2.79%

Equations (3. 6) and (3. 7) were used to calculate the shrinkage of structures presented by Amato et al. [123], Sharma et al.[70] and Lee et al. [133]. Results are shown in Figure 3. 6a. Amato et al. used SU-8 obtained from Microresist GmbH (Berlin, Germany) to fabricate carbon posts of 1.4 μm in diameter and 11μm um in height. Carbonization was done at a final temperature of 900°C, a dwell time of 1 hour and a heating ramp of 2°C/min. Lee et al. (Figure 3. 6b) used NANO™ SU-8 (MicroChem Corp., Newton, MA) for fabrication of mushroom-like shapes and cylindrical posts with height of 54 μm and diameter of 300 μm. Carbonization was carried out at 700°C with a dwell time of 30 minutes, and a heating rate of 10°C/min. Sharma et al. (Figure 3. 6c) used a carbonization protocol similar to Amato et al. but with a heating rate of 10°C/min. These authors carbonized cylindrical posts with height 80 μm and diameter of 15 μm.

In the case of Amato et al equation is effective in predicting shrinkage of the structures with an error of only around 1%. In the case of structures fabricated by Sharma et al. the shrinkage in the diameter was predicted precisely, but the shrinkage in height shows a difference of 10%. In the case of mushroom-like structures fabricated by Lee et al, equations are able to correctly approximate the shrinkage in diameter and height of the mushroom stem but not the shrinkage of the cap. Further work will be required to validate Equations (3. 6)-(3. 8) in predicting shrinkage of more complex shapes.
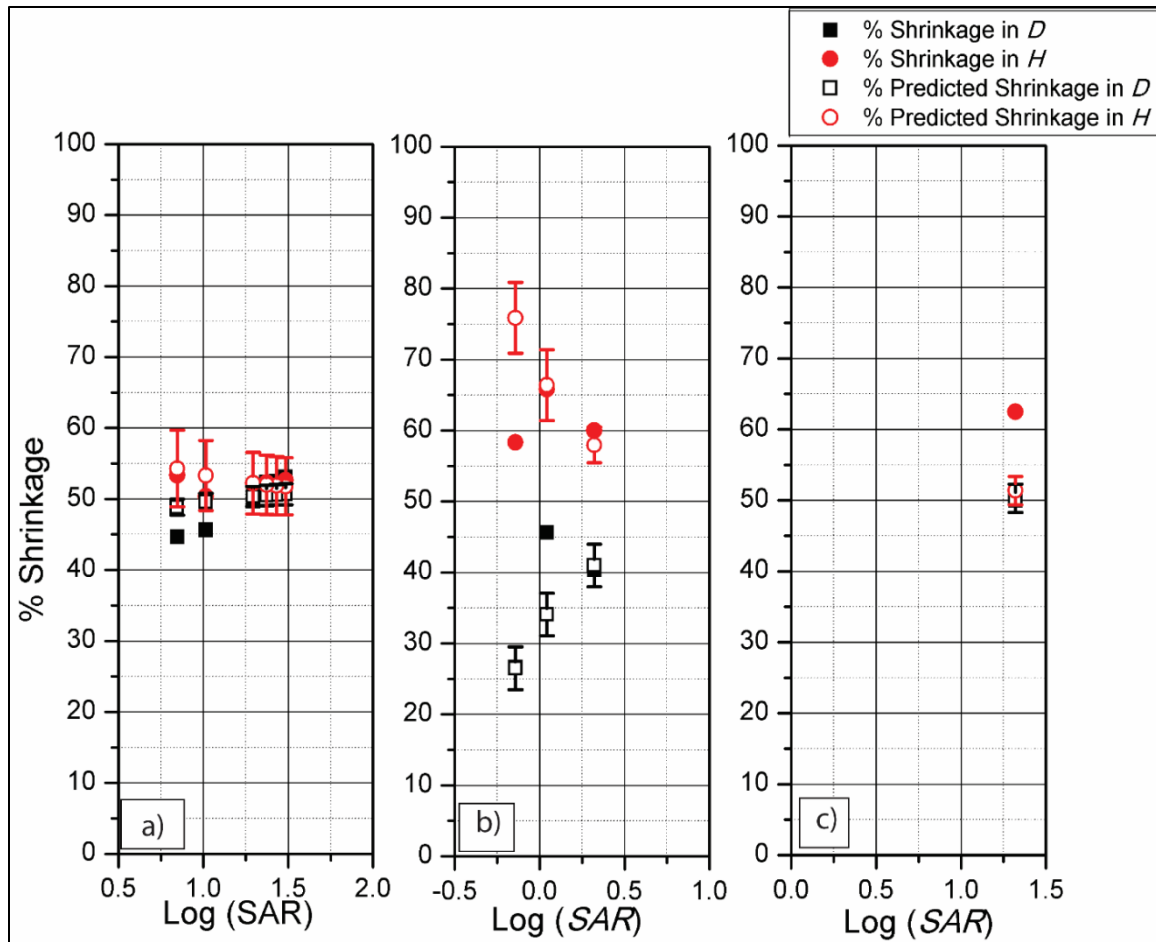
Figure 3. 6 Validation of the empirical equations for shrinkage. The graph shows the predicted shrinkage using Equations (3. 6) , (3. 7) and the shrinkage reported in the work by different authors [70,123,133] a) Posts from work of Amato et al.[123] and the predicted values of shrinkage for the structures show agreement. b) Posts from the work of Lee et al. [133] where the shrinkage in the stem of the mushroom structure shows agreement with the predicted value of shrinkage. c) The shrinkage of the posts fabricated by Sharma et al. [70] have shrinkage in diameter similar to the predicted value, but shrinkage observed in the height is more than the predicted value.

3.4. Summary of findings and contribution

In this analysis, the importance of degassing through surface area as a prime contributor for structural shrinkage is established. The results show that SAR is the most important factor in the basic shrinkage value for the SU-8 structure. A set of mathematical relations were obtained to calculate shrinkage based on SAR. The equations for curve fitting were successfully validated to predict shrinkage with previously published data. As long as the SAR value remains unchanged, the change in the cross section of the structure did not change shrinkage significantly. The effect of heating protocol on shrinkage was also studied. The final temperature and atmosphere during carbonization also play a role in shrinkage. Any impact on shrinkage from changes in dwell time and heating rate was not observed. Based on these results, it can be concluded that SAR, pyrolysis temperature and pyrolysis atmosphere are the major factors that affect shrinkage. These results were obtained using silicon substrates and taking the necessary steps to maximize the possibility that SU-8 was fully cross-linked before carbonization. These results will likely not be applicable for partially cross-linked SU-8. The shrinkage trends reported here are expected to be similar when using other substrates, as long as such substrate impedes degassing of the material during carbonization. The work presented here is the first methodical study of SU-8 shrinkage during carbonization and there are still gaps to be addressed. These include studying the impact of pressure, degree of SU-8 cross-linking, and exploring other atmospheres. These are necessary towards designing manufacturing processes that yield carbon structures tailored to specific applications.

The fabrication process to obtain 3D electrodes is optimized in this work. Consideration of shrinkage, during the design of electrodes can enable the user to make necessary adjustments beforehand. This can benefit the electrode design. The further part of the work utilizes the 3D carbon electrodes fabricated by SU-8 photolithography and pyrolysis process detailed in this chapter.

CHAPTER FOUR

COMPUTATIONAL MODEL FOR STREAMING DIELECTROPHORESIS

(Natu, Rucha, and Rodrigo Martinez-Duarte. "Numerical model of streaming DEP for

stem cell sorting." *Micromachines* 7.12 (2016): 217.)

4.1 Introduction

Next-generation therapeutics such as cellular therapy and tissue regeneration are

largely based on the use of stem cells [163]. These cells are characterized by a varying

capacity for growth and the ability to either differentiate into specialized cells or maintain

their stem cell phenotype. Neural stem cells are of special interest given their potential

for neurogenesis to treat spinal cord injuries and other nervous disorders [164–166].

However, the dynamic nature of stem cells and their susceptibility to environmental

changes demand technology to monitor, characterize, and manipulate living cells [103].

There is no clear set of surface markers with sufficient specificity to identify

promising cells, such as neural stem cells, from a background. This limits investigation of

lineage-biased progenitors and their potential use as therapeutic agents. Hence,

alternatives to traditional techniques are needed. The use of membrane capacitance and

dielectrophoresis (DEP) as a label-free technique to discriminate targeted cells from a

background is presented here for separation of neurogenic progenitors SC27 from

astr0genic progenitors SC23. The response of each type of cell to a polarizing field

gradient of a given frequency and when suspended in a specific medium depends on its

membrane capacitance as detailed in chapter 2, Figure 2. 3. The ultimate goal is an in-line

module for cell sorting that could be incorporated in the bio manufacturing of therapeutic cells, such as after cell expansion [167].

In this chapter, numerical simulation is used to assess the potential for continuous separation of Human Neural Stem/Progenitor Cells (HuNPSC) using streaming DEP. Streaming refers to the focusing of targeted cells into specific streams to facilitate their retrieval from the channel. The width of the stream should be maximized to increase throughput while the separation between streams must be widened to increase efficiency during retrieval. The goal is to understand the factors that influence the formation of these streams. To this end, the impact of electrode geometry, experimental flow rate and sample concentration on the efficiency and throughput of streaming DEP is assessed. Efficiency is defined as the ratio between the number of SC27 cells over total number of cells retrieved in the streams, and throughput as the number of SC27 cells retrieved in the streams compared to their total number input to the device. The implemented model can be applied for different electrode materials and DEP technologies. However, the goal is to use this model for the optimization of carbon electrodes.

4.2 Operating Principle of Streaming Dielectrophoresis

Cells can be attracted to a field gradient around the electrodes using positive DEP or repelled from it using negative DEP. Targeted cells can be focused into streams either collinearly with the electrodes by using positive DEP or between the electrodes using negative DEP. This is illustrated in Figure 4. 1. The red particles are attracted to the electrodes and eluted away in lines collinear with the electrodes. This is because the drag

and DEP forces acting on the cell are in equilibrium. Increasing the DEP force will lead to particle trapping while increasing the drag force will lead to particle elution.The blue particles in the figure are focused in streams between electrodes using negative DEP, as in this case is where the field gradient is of less magnitude. Once focused in streams, the retrieval of cells can be facilitated by geometries as those shown in the figure. By choosing the frequency of the polarizing waveform appropriately, one can induce a positive DEP force on specific cells while inducing negative DEP on the rest. Here, the aim is to study how the device geometry, such as electrode cross-section and height relative to the channel, and experimental parameters, such as flow rate and sample concentration, impact the width T and cell composition of these streams. Also, objective is to understand how these parameters need to be optimized to enable streams featuring all of the SC27 cells introduced in the system (100% throughput) without contamination with SC23 cells (100% efficiency).
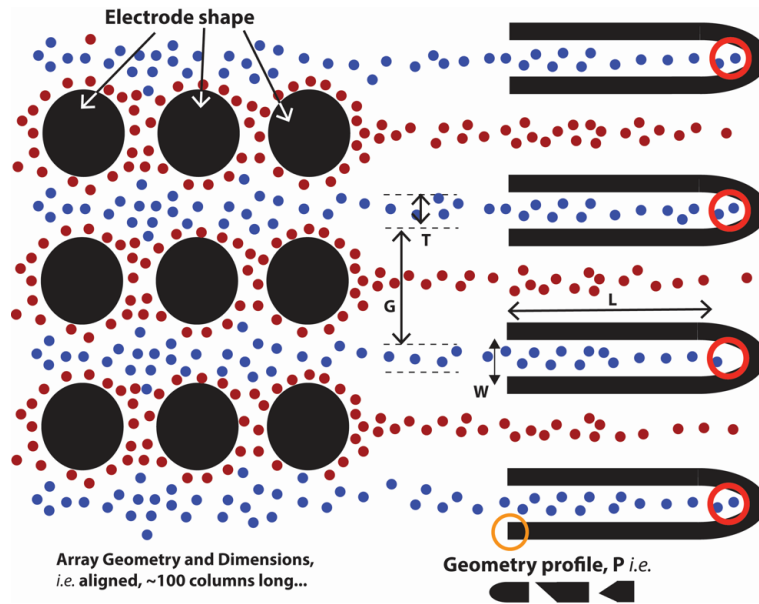
Figure 4. 1. Schematic of the working principle of streaming Dielectrophoresis (DEP). Cells can be focused into streams of specific width T and separation G between each other. Retrieval geometries can be used for continuous extraction from the channel. The impact of device geometry and experimental parameters on the composition and width of the streams is studied here. Specifically, the impact of electrode shape (circles, diamonds, lens-shaped) and height (10%, 50% and 100% of the channel height) as well as flow rate and cell concentration in the sample is of interest.

4.3 Materials and methods

4.3.1   Parameters for computation

COMSOL was used to build the model to solve for the flow field and electric field in a microfluidics channel containing an array of electrodes as detailed previously Section 2.4 of Chapter 2. The simplified top view of the geometrical model used is

illustrated in Figure 4. 2. 3D electrodes spanning 10%, 50%, 75% and 100% of a 100 μm-high channel were simulated. The length of the channel was 9000 μm. Three types of electrode cross-sections were used: circle, diamond and lens. The characteristic dimension for each of them was 50 μm as diameter for circles and side for lens and diamond (see Figure 4. 2). The channel width was around 700 μm and varied slightly depending on the shape of the electrode since the distance between the outer edge of the array and the channel wall was kept constant at 45 μm. The surface of the electrodes was arbitrarily polarized with voltages of 0 and 3 V to maintain a maximum electric field of 9.69×10^4 V/m and field gradient of 8.49×10^{14} V^2/m^3 to reduce the possibility of changes to the cells [168]. Flow rates from 5 to 20 μL/min were implemented since a flow rate of 20 μL/min was calculated to be the maximum value before inducing shear stress above 1.5 dyne/cm^2 on cells using the channel and electrode dimensions explored here. Given the length of the channel and flow rates simulated here, the maximum residence time of the cell in the channel is 40 s when using a flow rate of 1 μL/min.

The Laminar Flow and Electric Currents physics modules were used to compute the flow velocity and electric field gradient to calculate the drag and DEP force fields acting in the simulation domain at steady state. Gravitational and buoyancy forces were used to consider cell sedimentation. Equations (2. 19)-(2. 23) presented in Chapter 2 were solved to obtain the force fields. Given the limited computational power available and the desire to model high cell concentrations, cells were not modelled as spherical particles moving through the device. Instead, potential cell trajectories were modelled as the streamlines obtained by taking the particle velocity vectors calculated using Equation (2.

27) and were used to compute the position of the particle by the Lagrangian tracking method [5]. Both flow velocity and electric field gradient were obtained using COMSOL Muliphysics. The starting points of as many streamlines necessary to simulate a given cell concentration in the channel were randomly determined by generating random values in MATLAB (2014a, MathWorks ,Natick, United States) and feeding them back to COMSOL as starting positions. Such protocol enabled the simulation of cell dispersion throughout the channel cross-section at the inlet as will be expected in experiments. At least three different simulations were performed for each case of interest. Random starting points were used for each of these cases and hence the error bars shown in the results. From this point on in this manuscript, we refer to cell trajectories and locations as those that can be expected from modeling the streamlines in the channel.

The fact that the cells are simulated as streams introduces certain limitations in the calculations of stream widths. The thickness of the cell is not taken into account while simulating the streams. Hence, two streams that can come very close to each other (closer than the value of cell diameter) will not appropriately depict cell behavior. In addition, the number of cells that can be trapped on the electrodes is restricted. This is because as the cells accumulate at the electrode, they cover a certain positive area of the electrode. As more and more cells attract towards the electrode, less area is available for cell trapping. This restriction is not present in the case of the streamlines. In spite of these limitations, the streamlines help to depict potential paths taken by individual cells in the channel. All the streams were released in the channel at one time with the inlet velocities depending on their starting position and corresponding to a parabolic flow profile in the

71

channel. Furthermore, the electric field was assumed to not be affected by local field gradients around electrodes derived from particles already trapped on the electrode surface. All modeled materials were considered non-porous, while the properties of the medium are uniform throughout the channel.

The values for $Re[f_{CM}]$ of SC23 (0.15) and SC27 (-0.09) corresponding to the frequency of 200 kHz were used. This value was chosen based on Figure 2. 3c which shows that the $Re[f_{CM}]$ values for the two types of cells show maximum difference; hence DEP force acting on the two types of cells will differ significantly. The values of radius for the different cells were also taken as shown in Figure 2. 3a. Other simulation parameters are specified in Table 4 1.

Table 4 1 Parameters defined for the model

Name	Value	Description
velocity	u	Flow rate in channel
R	From Figure 2. 3a in Chapter 2	Radius of Stem Cell
σ_m	0.51500 S/m	Conductivity of Media
CM	From Figure 2. 3a in Chapter 2	Clausius Mossotti factor
μ	8.90×10^{-4} Pa·s	Dynamic viscosity of water as media at 25 °C
ε_m	80.2	Relative Permittivity of water as media

Equations (2. 31)-(2. 33) from Chapter 2 were solved in stationary domain in

COMSOL Multiphysics. X, Y and Z components for FDEP were calculated here by using

the equations in for electric field gradient for the SC23 and SC27 cells. The flow velocity

u for the laminar flow field was calculated using Equations (2. 19) and (2. 20) in Chapter

2.

The values for the flow velocity and the F_{DEP} were used to simulate the particle

motion with the particle velocity v given by Equation (2. 27). Streamlines were simulated

by using the velocity represented by Equation (2. 27) with different inlet positions of the

cells. The medium conductivity used was 0.05 S/m which has been shown to not affect

the cell viability of stem cells, as was recently shown by Lu et al. as long as the cell is

exposed for less than a minute [3].
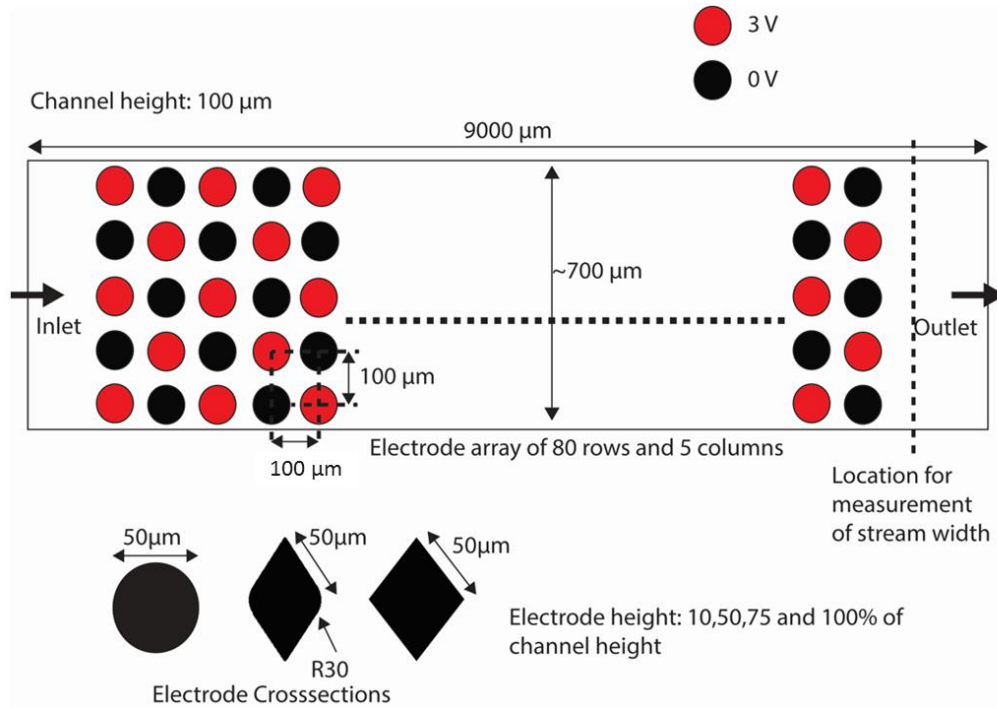
Figure 4. 2 The top view of the model used for numerical analysis with the dimensions and electrode polarity. The top view of the model used for numerical analysis with the dimensions and electrode polarity is shown in the figure. The electrodes are arranged in a manner that they lie in straight rows and symmetrical rows. However, the electrodes are polarized alternately using either 3 or 0 V. The three cross-sections studied in this work are shown: circles, lens and diamonds. The model shown is not true to the scale, but represents the actual shape of the electrodes and channel.

4.3.2   Data analysis

COMSOL data points corresponding to the ends of the streamlines were exported to MATLAB 2014a for post processing. MATLAB was used to filter the streams that represent the SC23 and SC27 cells that are captured at the electrodes and only the

74

streams that reach the outlet were selected. Plots were generated for the ends of the

streamlines at the channel outlet. This data is converted to a histogram wherein the

channel width is divided into small bars (or datasets) for the range of around 6 μm width

along the channel. This width was arbitrarily selected. Thus, the channel of ~700 μm-

width is divided into around 115 bars. The number of streamlines reaching the outlet in

the width of such a bar is stored and this data is used for calculating the percent purity of

both SC23 and SC27 types of streams in the domain. This is calculated using Equation

(4. 1), where X can take the value of 3 and 7 depending on the cell type being analyzed

(SC23 or SC27). Equation (4. 2) is used to calculate the throughput of the system.

$$\% \text{ purity of SC2}X \text{ cells in a bar: } \frac{\text{total number of SC2}X \text{ streamlines in the bar}}{\text{total number of streamlines in the bar}} \times 100 \quad (4.\ 1)$$

$$\% \text{ throughput of SC2}X \text{ cells} \quad (4.\ 2)$$

$$= \frac{\text{total number of SC2}X \text{ streamlines in the bar} \times 100\%}{\text{total number of streamlines of SC2}X \text{ at inlet}}$$

4.4 Results

The results are resumed in the graphs shown in Figure 4. 4a–d for different cases of

electrode shape or cross-section, electrode height, flow rate and cell concentration in the

sample. The x-axis in each case shows the distance along the channel with the scale

marks denoting the center position of the electrodes (45, 195, 345, 495 and 645 μm). The

percentage of SC23 (red) and SC27 (blue) streamlines flowing at that particular location

is denoted in the y-axis. The cells of interest here are SC27 cells, given their neurogenic

properties. A blue stripe spanning the complete height of the graph marks the specific

location where a 100% pure SC27 cell stream can be retrieved. The throughput was calculated as the ratio between the number of SC27 in the streams and those entered into the system. Hence, a 100% throughput means recovery of all cells entered in the system. The throughput is reported in Table 4. 2. The goal of this work is to study the impact of different electrode geometries and experimental parameters on the efficiency and throughput of streaming DEP. structures with diamond and circular cross-sections and width of ~80 μm. The use of a square shape was concluded to provide the highest trapping capacity due to the presence of large volumes with high electric field square gradient. However, the diamond and circle shapes were proven beneficial for cell focusing [169]. In the case of streaming DEP, Cummings et al. studied the use of diamond and circular cross-sections [78,170]. In the case of diamond shaped electrodes, particle concentration was seen to deplete as the particles moved along the channel showing high rate of particle capture. For posts with circular cross-sections, the particles became more focused as they moved through the channel but showed less capture than the diamonds.
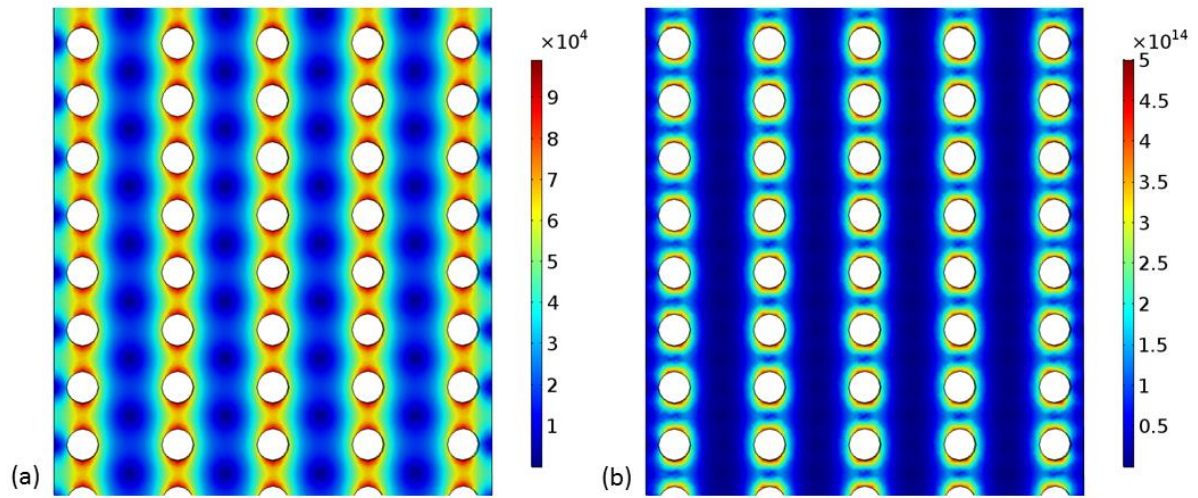
Figure 4. 3 The electric current simulation results for the array of electrodes showing the a) electric field in the domain and the b) electric field gradient around the electrodes

4.4.1 Shape of electrodes

The electrode shape plays an important role in determining the trapping capability when using DEP as well as the flow around it. For example, the use of sharp angles may lead to sharper electric field gradients and possible turbulence at high flow rates. Although the use of cylindrical electrodes is prominent in DEP [48,67,171], other shapes of electrodes or insulator structures have been studied. For example, Saucedo-Espinoza et al. explored

Table 4. 2. The average percentage throughput in the simulation for SC23 and SC27. The throughput represents the percentage of total incoming streams of each type that are present in the streams after the electrode array. Since most of the SC23 streams show positive dielectrophoresis (DEP) and are captured at the electrodes, the throughput for

77

this case is generally low. SC27 cells show negative DEP, no significant trapping and

thus a high throughput is obtained.

Parameter	Value	Throughput : SC23	Throughput : SC27
Shape of electrode	Lens	0.3%	69.43%
	Circle	2.40%	62.09%
	Diamond	8.51%	61.54%
Height of electrode as % of channel ht	10%	11.31%	55.86%
	50%	3.37%	64.35%
	100%	2.40%	62.09%
Flow Rate	1 μL/min	0%	0%
	5 μL/min	0%	33.33%
	10 μL/min	2.40%	68.09%
	20 μL/min	14.48%	81.40%
Cell Concentration (Cells/mL)	10^2	10.61%	41.92%
	10^4	2.88%	68.18%
	10^6	2.36%	62.52%
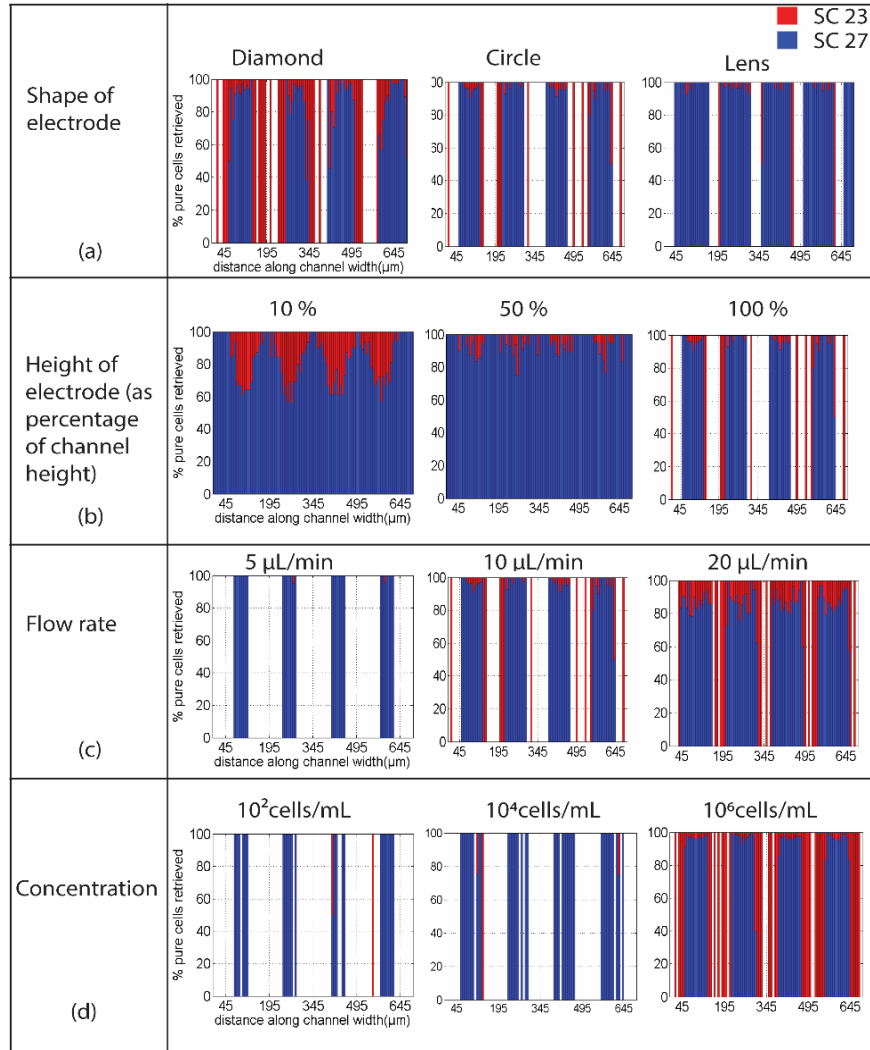
Figure 4. 4 The percentage of SC23 and SC27 retrieved in different conditions considered in the numerical simulations. The stacked histogram in *y*-axis shows the percentage of SC23 and SC27 streams retrieved at different channel locations (from 0 to 700 μm). The *x*-axis in each case denotes the distance along the channel width (a) The impact of electrode cross-section; (b) Impact of relative electrode height; (c) Impact of flow rate. (d) Impact of cell concentration on the separation efficiency between cell types at 10 μL/min.

79

The results obtained when using electrodes of different cross-sections but height equal to 100% of the channel height are shown in Figure 4. 4a for a flow rate of 10 µL/min and cell concentration of 2×10^5 cells/mL. The case of diamond cross-section yields a high amount of SC23 cells being trapped in the array due to the sharp corners of the electrodes and the high field gradients that are generated. Only 8.51% of the SC23 population input in the model could be retrieved and hence the predominance of blue in the figure. About 61.54% of the SC27 cells could be retrieved at the array exit. Although the retrieval throughput of SC27 is high, the purity is only around 90% in most regions, with 95% in a few regions. In the case of circle cross-section, the retrieval of SC27 is about 62.09% whereas SC23 streams have a throughput of 2.40%, showing less trapping of SC23 cells compared to diamonds. For circles, well-defined regions with SC27 purity greater than 95% can be seen in the figure. The use of the lens cross-section yields a throughput of 69.43% for SC27 cells, comparable to that of circles, but features the least percentage of SC23 retrieval among the three, only 0.3% SC23, thereby indicating high trapping and the predominant white regions aligned with the electrodes. The purity obtained in the case of lens is higher than that obtained when using the other two cross-sections; close to 100%, pure SC27 streams can be seen throughout the width of the channel.

4.4.2 Height of electrodes

The height of the electrode with respect to the height of the channel was varied and studied to see the effect it has on the capture and effective focusing of the SC23 and SC27 streams. The obtained results are shown in Figure 4. 4b when the electrodes are

10%, 50% and 100% of the channel height (100 μm here). These results were obtained

when using circular electrodes, a flow rate of 20 μL/min and concentration of 2×10^5

cells/mL. When the electrode height is 10% of the channel height, the throughput for

SC23 is about 11.31%, whereas the throughput for SC27 is about 55.86%, indicating

poor trapping for both cell types, which is beneficial for continuous sorting. However, the

average purity obtained at this electrode height for SC23 streams is around 20% (max.

25%), while the average purity for SC27 streams is around 70% (max. 75%). The

electrodes with a height 10% of the channel are not a good choice for separation of the

two species. For the electrodes with a height 50% of that of the channel, there is

improvement in the trapping of the SC23 streams and the purity of SC27 streams. Around

3.37% of SC23 streams and 64.35% of SC27 streams can be retrieved. These electrodes

show high trapping of SC23 streams, but the focusing of SC27 streams by negative DEP

is limited. The case when the electrodes are as tall as the channel shows high

improvement over the previous cases. Though the throughput of SC23 decreased to only

2.40% in this case, 68.09% SC27 streams were retrieved. The retrieval of highly focused

SC23 and SC27 streams with purity higher than 95% is possible in some regions of the

channel as seen in the graph. These results reinforce experimental results previously

reported where the use of 3D carbon electrodes yielded better trapping efficiency [56].

4.4.3 Flow rate

An important parameter to study when aiming at increasing device throughput is

flow rate. The upper limit on the flow rate value is given by the necessity to prevent cell

damage by shear stress. Hence, a maximum flow rate of 20 μL/min is used in this work.

The results obtained when increasing the flow rate from 5 to 20 µL/min at a concentration of 2×10^5 cells/mL are reported here. Simulations using flow rate of 5 µL/min illustrate how all SC23 cells get captured due to dominance of dielectric force over the drag force. As the flow rate increases to 10 µL/min, the drag force starts to dominate the dielectric force and hence the number of trapped SC23 decreases and around 2.40% of them can be retrieved. Up to 68.09% of SC27 streams are retrieved. Though the retrieval of SC27 streams is high, the purity in this case is affected as some SC23 streams are seen in the same region as the SC27. At 20 µL/min, the maximum purity in SC27 streams that can be expected is around 85% while the throughput is around 81.04%. The throughput of SC23 is 14.48% indicating the decrease in capture of SC23 as the flow rate increases from 10 µL/min to 20 µL/min. The average purity of SC27 streams is higher (85%–90%) in the regions closer to the electrodes than in the regions in between the electrodes where it is around 70%. This is because SC27 flowing near the electrodes are effectively diverted by the dielectric forces, whereas the SC23 streams in this region are attracted to the electrodes. These phenomena decrease as the cells flow deeper into the region between the electrodes, where the SC23 and SC27 are less affected by dielectric force, and more by the drag force. Being similar in size, there is no significant discrimination between them. At the flow rate of 20 µL/min, 100% pure SC23 can be obtained in regions immediately next to the electrodes. The dielectric force is very high in these regions and SC23 streams are directed towards the electrodes. However, given the high drag force at high flow rates, the SC23 cells no longer are captured but instead are focused and eluted collinearly to the electrodes. The SC23 cells that are not

affected by the DEP force attracting them to the electrodes decrease the purity of the SC27 cell stream flowing in between electrodes.

4.4.4 Cell concentration

The results obtained when simulating different cell concentrations at the flow rate of 10 µL/min when using 100 µm-high circular electrodes are shown in Figure 4. 4d. The concentration increased from 10^2 to 10^6 cells/mL. The case with 10^2 cells/mL corresponds to one cell flowing through the modeled channel at a given time. Similarly, 10^4 cells correspond to 100 cells. For the case of 10^5–10^3 cells/mL, random coordinates were generated to determine the starting position of the cells. For the case of 10^3 cells/mL, ten different coordinates were generated to obtain a more realistic model. Three repetitions were done for cases 10^4 and 10^5 cells/mL, while only one trial was implemented for the case of 10^6 cells. The results shown in Figure 4. 4d are representative of each case. In all cases, high purity SC27 streams are obtained from regions in between the electrodes, while mostly all the SC23s in the channel are trapped when concentration is less than 10^5 cells/mL.

4.5 Discussion

The width of the elution stream, *T,* and the separating gap between the streams, *G,* are important design parameters in streaming DEP to enable continuous separation as shown in Figure 4. 1. Depending on their values, one can design geometries with an optimized opening *W* for continuous extraction of the targeted cells from the channel. Photolithography is a technique that is amenable for the fabrication of such

geometries[172]. If using photolithography, the minimal width of these retrieval

geometries is likely to be in the tens of micrometers, with separation between each other

in the same range. The width of these retrieval geometries, W, would ideally be less than

the width of the cell stream, T, since this will allow for a buffer zone to mitigate

contamination with other cells at the edges of the retrieval geometries. Although the

downside to this will be the loss of targeted cells and a decrease in throughput, this may

be less significant if the yield of cell expansion and differentiation during cell

manufacturing is high.

The change of stream width according to the parameters studied here is presented in

Figure 4. 5. All points shown in this figure correspond to stream widths with purity >98%

as calculated using Equation (2. 12) in Chapter 2. Since the diameter of the SC27 cells is

~15 μm, streams narrower than this value are not considered. The effect of electrode

cross-section is shown in Figure 4. 5a. Similar to the results obtained when varying

electrode height and cell concentration (Figure 4. 5b and c, respectively), a peak on the

stream width can be observed when varying the electrode cross-section. This peak occurs

at 10 μL/min in the case of circular electrodes and 5 μL/min for diamonds and lens.

Before these peak values, the increase on stream width is due to the combined effect of

high trapping of SC23 cells on the electrodes and sharp focusing of SC27 streams by

negative DEP. With the increase in flow rate beyond the corresponding peak values, not

all SC23s are remain trapped and they start being eluted. The purity and width of the

SC27 streams are thus reduced. At their peak values, the circular electrodes yield the

widest retrieval zones at 83.16 ± 6.93 μm-width. Lens and diamonds yield 51.97 ± 8.94

μm and 64.68 ± 8.00 μm respectively at their peak values at 5 μL/min flow rate. The lens shape can be described as a combination between circle and diamond shape. Hence, it has regions with high gradients along the curved edges, like circles, which facilitate cell movement along the electrode surface. It also features sharp points like diamonds, which are useful for positive DEP of SC23 due to the high electric field gradient generated at such points. In contrast to the case of diamonds where the stream width decreases rapidly after 5 μL/min of flow rate, the decrease in the case of lens is gradual. This is due to the focusing of SC23 towards the electrodes decreasing gradually when compared to diamonds.

A peak on the stream width can be observed when varying the other parameters of interest as well. In the case of electrode height, the use of electrodes as tall as the channel (100% height) leads to a maximum stream width of 83.16 ± 6.93 μm at 10 μL/min. The use of shorter electrodes does not yield stream widths as wide. In the case of electrodes spanning half the channel height, the peak value of stream width is seen at 5 μL/min but the value drops at higher flow rates since the drag force starts dominating the DEP force. The use of short electrodes only addresses the particles flowing close to the channel floor and hence their separation performance is poor. The region with active electric field is present only at the 10% of the channel height and hence the stream widths obtained in this case are smaller than the electrodes covering 50% and 100% of the channel height.

Using cell concentration of 10^2 cells/mL resulted in the widest stream width (77.96 ± 10.39 μm) followed by 10^4 cells/mL (65.83 ± 8.94 μm) and 10^6 cells/mL (6.93 μm). A peak on the stream width is again observed at 10 μL /min for the concentrations of 10^2

and 10^4 cells/mL. An important observation here is with the cell concentration of 10^5 cells/mL considered in the case of Figure 4. 5a,b. In these cases, the cell concentration of 10^5 cells/mL shows a high stream width of around 83.16 μm. Thus, the stream width is seen to decrease beyond this value of cell concentration. The use of flow rates of 20 μL/min leads to a significant decrease in the width of streams with purity of SC27 cells >98%. For a fixed stream width, a lower cell concentration ~10^2 cells/mL with a high flow rate can give a device with high efficiency, but with a low throughput. Using samples with high concentrations ~10^6 cells/mL at a low flow rate can give a high throughput but with a low efficiency. The parameters to be implemented can thus be optimized based on the requirement of throughput and efficiency depending on the application.

The behavior of stream width and composition depending on electrode geometry, flow rate and sample concentration has been studied here. Implementing a flow rate of 10 μL/min leads to SC27 cell streams featuring purity >98% and as wide as 80 μm when using cylindrical electrodes that are as tall as the channel and a sample concentration in the range 10^2–10^5 cells/mL. However, the throughput changes with the cell concentration from 41.92% at 10^2 cells/mL to 61.52% at 10^5 cells/mL.

The number of cells currently required for neuron-based therapy is around 10^5 per dose. [173] At a flow rate in the device of 10 μL/min, a sample concentration of 10^5 cells/mL, a throughput of 62.09%, and assuming that up to 50% of the sample are cells of interest, the purification of SC27 cells using streaming DEP with the device modeled here

will take around 6 h. At these conditions, an individual cell undergoes shear stress lower than 1.5 dynes/cm^2.
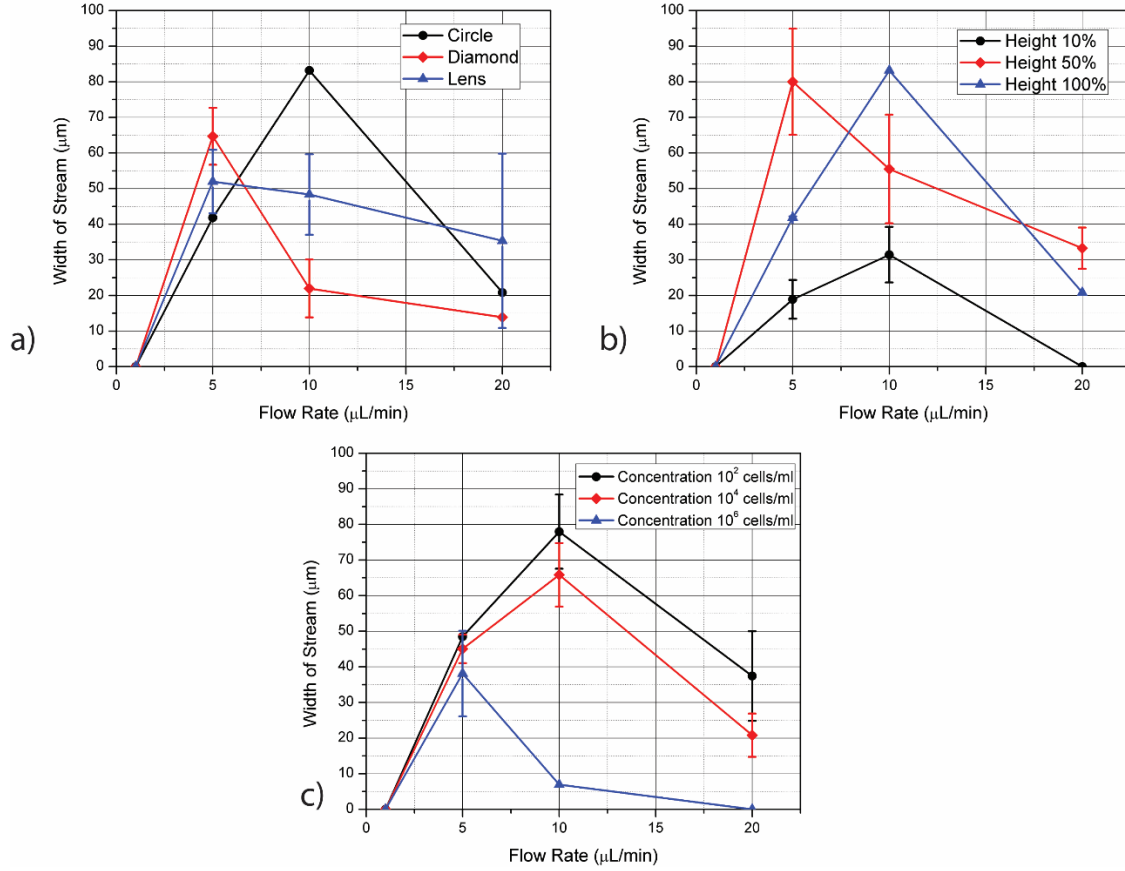
Figure 4. 5 Streamwidth obtained with respect to system parameters. (a) The width of stream or zone obtained in the case of each electrode such that >98% pure streams of SC27 (b) The width of the streams for obtaining >98% pure SC27 streams at different heights of the cylindrical electrodes as the flow rate varies. (c) The study of concentration of streams was conducted for stream purities of 98% and above with the increase in flow rates.

Future work will be on increasing the flow rate through the device while maintaining low levels of shear stress. For example, the channel cross-section will be

significantly expanded to increase the flow rate thanks to the increase of cross-section only. This will likely require the fabrication of improved 3D electrodes and the optimization of their polarizing voltage depending on the electrode material.

Once the streams are formed, retrieval geometries will be implemented. The length of the retrieval geometry L in Figure 4. 1 plays an important role to sustain the retrieved cells. A short geometry will cause quick accumulation and clogging of the retrieval geometry. In addition, at high flow rates, the inflowing stream will cause transient flow in the collection geometry and will build backpressure in the zone. To avoid this, the retrieval geometry should be sufficiently long to allow continuation of the flow developed in the channel. The design of the entrance profile marked as P in the Figure 4. 1 also affects the dynamics of the streaming geometry. For example, at a flow rate of 10 µL/min, a discrete separation between SC27 and SC23 streams is obtained and a pointed entrance profile will cut through the flow without affecting the cell streaming.

4.6 Summary of findings and contribution

The results presented demonstrate the potential to continuously separate SC27 from SC23 cells using streaming dielectrophoresis (DEP). The impact of electrode geometry, flow rate and sample concentration on the generation of cell streams with purity >98% was studied. The use of circle and lens cross-section proves beneficial for obtaining high stream widths, but the circle cross-section offers better reproducibility. The use of electrodes as tall as the channel was concluded to be ideal due to the wide streams obtained at the flow rate of 10 µL/min. The stream widths show a peak with the increase in flow rate initially as the effect of DEP and drag forces aid the stream

formation, but the stream width decreases further as the flow rate increases. Increasing

the cell concentration above 10^5 cells/mL was seen to generate narrower stream widths.

The throughput obtained in the case of electrodes with 100% height and circular cross-

section is 62.09% and varies with electrode shape and flow rate in the channel. The use of

cylindrical electrodes as tall as the channel leads to the generation of streams with width

up to 80 μm, which facilitates the fabrication of retrieval geometries using

photolithography. The time required to generate a therapeutic dose using the parameters

optimized here can be as long as 6 h. This is deemed too long for a practical application

and further work is required to shorten this time to less than 30 min. However, these

initial results allow for identifying the effect of different parameters on the equilibrium

between the DEP and drag forces required for streaming DEP. Streaming DEP can enable

continuous separation of cells in a microfluidic chip. Chapter 5 focusses on the further

part of the work where streamingDEP is considered purely for positiveDEP.

CHAPTER FIVE

ANALYTICAL EXPRESSION AND EXPERIMENTAL VALIDATION OF
STREAMING DIELECTROPHORESIS (streamingDEP)

(Rucha Natu, Monsur Islam and Rodrigo Martinez-Duarte, "Non-dimensional Streaming

Dielectrophoresis Number for a System of Continuous Particle Separation", Submitted to

Analytical Chemistry, October 2018.)

5.1 Introduction

Chapter 4 explores the feasibility of using streaming using DEP and drag forces as a

continuous separation technique. The use of positiveDEP for streaming (referred to as

streamingDEP) has not been widely reported. Cummings et al. introduced the concept of

streamingDEP using electrokinetic flow and insulator-based DEP to focus 200 nm-

diameter particles into streams in the vicinity of the electrode surface [78]. Nakano et al.

later reported streamingDEP of proteins Immunoglobulin G and bovine serum albumin,

also using insulator based DEP in combination with electrokinetic flow [174]. The use of

streamingDEP is important because it opens up a whole region of the device that was

previously unattainable when limited to streaming with negativeDEP only. Since

particles are not trapped on the electrodes, streamingDEP allows for simultaneous sorting

using both positive and negativeDEP. The magnitude of positiveDEP forces are known to

be higher than negativeDEP forces, which is expected to enable higher spatial resolution

during sorting, effectively removing the limitation of continuous sorting.

In Chapter 4, it is evident that streamingDEP is observed only in certain range of the flow, voltage and frequency parameters. To determine this working range for streamingDEP, a relation between the system parameters and the streaming behavior is needed. This Chapter provides an analytical expression to predict the streamingDEP behavior based on the experimental conditions for a given cell. To this end, the derivation of an expression for streamingDEP number (SDN) depending on velocity in the channel, voltage and frequency of the polarizing signal, cell electrical properties and dimensions of an array of cylindrical electrodes is presented. Then, the results of an experimental study of the applicability of SDN when using latex particles are presented. Finally, SDN is used to corroborate experimental results from Cummings [78].

5.2 Derivation of streamingDEP number

Different examples of streamingDEP are shown in Figure 5. 1a-b. Note how the particles and Candida cells are focused on lines collinear with the electrode rows. Examples also show how particles undergoing positive and negativeDEP undergo focusing on specific locations. StreamingDEP is possible due to the equilibrium between DEP and drag force. If DEP overcomes drag, the particle will be trapped on the electrodes; if drag overcomes DEP the particle is eluted away and any sorting is solely due to cell size.

5.2.1 Definition of variables

The region of interest in this work is an array of N columns and M rows of cylindrical electrodes with radius r_e (Figure 5. 1c). The center-to-center distance

between electrodes is denoted by C_x along the x axis (rows) and C_y along the y axis (columns). Since a minimum number of columns is expected to be necessary to focus particles into streams, the importance of columns supersedes that of rows in streamingDEP. Hence, the analysis was simplified to the central row of electrodes in the array first and then to one half of such a row due to symmetry. Three reference lines aligned to the x axis will be used here to facilitate analysis: 1) line AA intersecting the center of the first electrode of the row of interest, 2) line BB intersecting the center of the last electrode, and 3) line CC at a distance k away from the last electrode and representing the region where streamingDEP will be characterized. The location in which the particle enters the domain of interest is given by X_{in}, which can be any position between the edge of the first electrode and the middle of the gap between rows, or $r_e < X_{in} < C_x/2$. The length of the electrode row, or distance between AA and BB, will be given by $L=(NC_y)$. The location of the particle at the line BB will be given by X_{out} and is used as an auxiliary variable. The final position of the particle will be measured along the line CC and reported as X_{stream}. A number of variables are also defined to make this analysis non-dimensional. These are confinement ratio $\lambda = r_p/d$; the constriction ratio $\gamma = r_e/d$ where $d=(C_x/2)$; while X_{in}, X_{out} and X_{stream} are rendered non-dimensional by dividing each by d leading to X_{in}^*, X_{out}^*, and X_{stream}^* (i.e. $X_{in}^*=X_{in}/d$). Reference line CC provides an expansion to the flow domain on reference line BB. Thus, the particle position on reference line CC, i.e X_{stream}^*, can be determined from position X_{out}^* by using the proportionality given by Equation (5. 1).
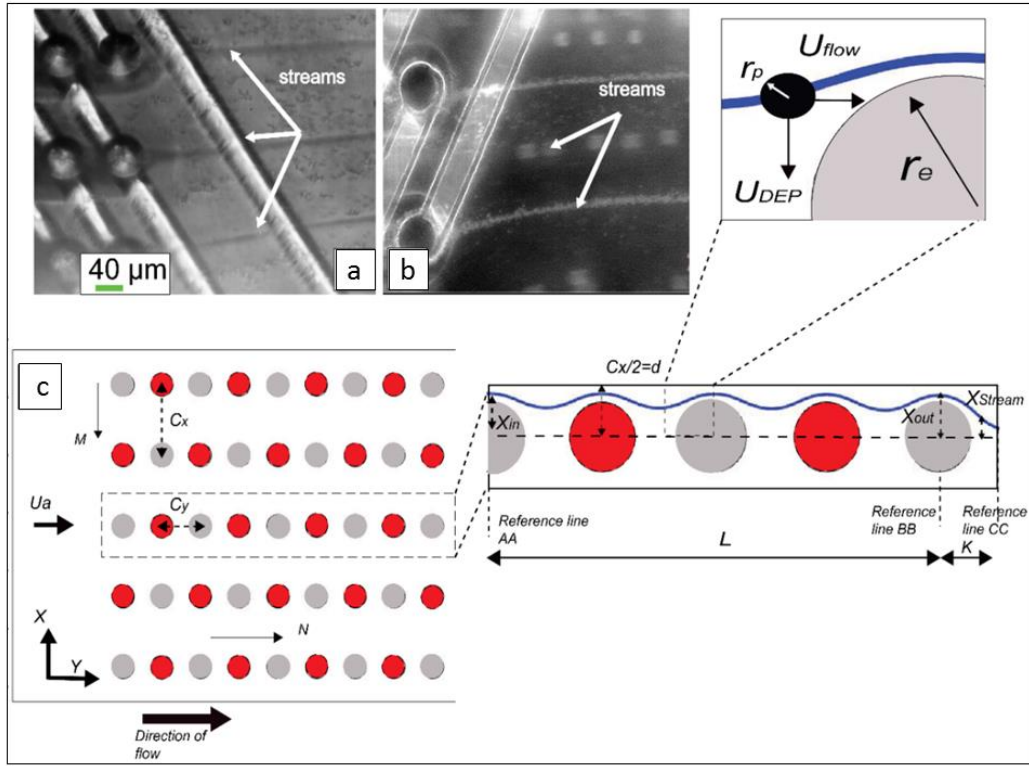
Figure 5. 1 Streams obtained at different instances and schematic for analysis. Streams obtained at different instances. a) Streams obtained with C.albicans cells with 3D carbon electrode chip using positive DEP at 500 kHz, 20V and 0.022 m/s flow rate. b) Continuous separation of 1 and 10 μm particles seen as an effect of streaming, where 1 μm particles show positive DEP whereas the 10 μm particles show negative DEP. c) Schematic of the simulated channel showing a hypothetical particle trajectory with the terms and nomenclature used in the equations

The z axis is along the height of the channel H. The flow rate at the inlet of the channel is U_a and the voltage used to polarize the electrodes is V.

$$X_{stream}^* = \frac{(X_{out}^* - \gamma)}{(1 - \gamma)} \qquad (5.1)$$

5.2.2 Assumptions and simplifications

All quantities are considered in SI units. Analysis cinsiders low Reynolds Number for the flow-electrode system (≤ 10) where flow vortices are not present [175]. The flow is assumed fully developed, laminar, steady and incompressible flow. Furthermore, the gap-to-diameter ratio for the electrodes ($\frac{C_y}{2r_e}$) uses is smaller than 5 and for this ratio, vortices are not formed between cylinders.[176,177]. Particles are assumed to be spherical. When the trajectory for particle originating at $X_{in}{}^*$ is governed solely by the flow, particle follows the flow pathlines and focusing does not occur. The presence of electrodes create negligible disturbance in the flow pathlines for the cases considered here [178]. In such a case, we can assume that in absence of electric field the particle position with respect to the electrode in x direction is unchanged and $X_{in}{}^* = X_{out}{}^*$. When electric field is present, the particle position in the x direction will change due to the DEP force. This displacement can be accounted by the DEP velocity of the particle,

$$u_{px} = u_{xDEP} \tag{5.2}$$

In the y direction, the particle movement will mainly occur due to the flow velocity since u_{yDEP} is around 10^4 times smaller than the flow velocity component (Appendix B) and is neglected in the analysis. Hence,

$$u_{py} = u_{yflow} + u_{yDEP} \approx u_{yflow} \tag{5.3}$$

Owing to the nature of pressure driven flows, u_{yflow} will have a parabolic profile, with the velocity maxima at the distance d from the electrode.

In this work, to simplify the calculations, the velocity $u_{py} = u_{yflow}$ is taken to be constant for the entire time of the particle travel. With this value of u_{py}, the time taken to reach the end of the channel is given by $\frac{L}{u_{py}}$. As the particle comes closer to the electrode, i.e to the edges of the parabolic flow profile, u_{py} is expected to decrease. Using constant value of u_{yflow}, enables the consideration of smallest possible time for the particle travel. In a 3D channel, the flow profile along z is defined between the top and the bottom cover plate and can be given by the parabolic profile representing flow between stationary parallel plates using Couette's flow equation. Because of this flow profile, the velocity varies within channel as a function of height. Similar parabolic profile is also developed in the x-y plane between the vertical walls of the channel. The average velocity U$_{ah}$, in the x-y plane at height h, is given by,

$$U_{ah} = 4U_a(\frac{h}{H})(1 - (\frac{h}{H}))$$
(5. 4)

where h is measured along the channel height (refer to Appendix B).

The non-dimensional velocity u_{py}^* for a particle at height H, was obtained from COMSOL simulation by solving for laminar flow similar to the process in Chapter 4. (detailed in Appendix B)

$$u_{py}^* = \frac{u_{py}}{U_{ah}} = 6.4(X_{in}^* - \gamma)(1 - (X_{in}^* - \gamma))(2\gamma + 1))$$
(5. 5)

Since u$_{px}$ depends only on DEP, the expression for u_{px}^* is

$$u_{px}^* = \frac{u_{xDEP}}{U_{ah}} = \frac{2\pi\varepsilon Re[fcm]r_p^3\nabla E_{rms}^2}{6\pi\mu r_p U_{ah}} \qquad (5.6)$$

COMSOL was also used to derive a non-dimensional expression for electric field E^* (Equation(B. 3)) (Appendix B). As previously reported by Kralj, et. al and Schnelle, et al. [179,180], this approach is useful to derive an expression of E for complex geometries where an analytical expression is challenging to derive. E_{rms} corresponds to the AC sinusoidal signal used in this work.

$$E^* = 0.55(\frac{x^*}{\gamma})^{-1} \quad \text{and} \quad E_{rms} = 0.7E^* * (\frac{V}{d-r})/\sqrt{\gamma} \qquad (5.7)$$

For obtaining non-dimensional equations for the particle velocities, the distance in x direction and y direction are given in terms of non-dimensional variables by Equation (5. 8),

$$x^* = x/d \text{ and } dx^* = dx/d ; y^* = y/L \text{ and } dy^* = dy/L \qquad (5.8)$$

5.2.3 Derivation

A crucial consideration in the derivation of SDN is that a particle only streams if the time it takes to travel from X_{in}^* to X_{out}^* is smaller than that required to traverse the array length L.To conform to the condition of streaming, the particle should satisfy the inequality,

$$\int_{Xin}^{Xout} \frac{dx}{u_{px}} \leq \int_0^L \frac{dy}{u_{py}} \qquad (5.9)$$

The left side of the inequality describes the total time taken by the particle to cover the distance from X_{in} to X_{out} and the right side describes the time taken to cover the length L along y direction. By using the non-dimensional terms in Equation (5. 8), integral $\int_{Xin}^{Xout} dx$ will be modified to $\int_{X_{in}^*}^{X_{out}^*} d.dx^*$ and $\int_0^L dy$ will be modified to $\int_0^1 Ldy^*$. Equation (5. 9) can be written as,

$$\int_{X_{in}^*}^{X_{out}^*} \frac{d * dx^*}{U_{ah} * u_{px}^*} \leq \int_0^1 \frac{L * dy^*}{U_{ah} * u_{py}^*} \qquad (5.\ 10)$$

By calculating ∇E_{rms}^2 from Equation (5. 7) and substituting the value for u_{py}^* and u_{px}^* from equations (5. 5) and (5. 6), Equation (5. 10) can be written as,

$$\frac{\mu(X_{in}^{*\ 4} - X_{out}^{*\ 4})(d-r)^2}{0.39\lambda^2 \varepsilon Re[fcm]V^2\gamma} \leq \frac{L}{u_{py}^* U_{ah}} \qquad (5.\ 11)$$

Which can be further simplified as,

$$\frac{\mu(X_{in}^{*\ 4} - X_{out}^{*\ 4})(d-r)^2 u_{py}^* U_{ah}}{0.39\lambda^2 \varepsilon Re[fcm]V^2\gamma NC_y} \leq 1 \qquad (5.\ 12)$$

Where the term $\frac{\mu(X_{in}^{*\ 4} - X_{out}^{*\ 4})(d-r)^2 u_{py}^* U_{ah}}{0.39\lambda^2 \varepsilon Re[fcm]V^2\gamma NC_y}$ is the Streaming DEP Number (SDN) and depends on the device geometry, particle properties and the profiles of both the flow and electric fields in the domain. SDN=0 when no flow is present. SDN=1 implies within the time taken by the particle to reach the distance *L*, it can be successfully focused at a distance of X_{out}^*. SDN>1 signifies that the time taken by the particle to reach the outlet is

too short for focusing. 0<SDN<1 represents streaming since the time taken by the particles to travel in x direction to the location $X_{out}{}^*$ is smaller than the time taken by the particles to travel the distance of L ($=NC_y$) in y direction. However, this condition also applies to particles that are trapped. Distinguishing between the streaming and captured particles based on the value of SDN has limitations. Further simplification of SDN by determining the probability of the cells reaching the outlet is feasible, but will depend on the number of cells for a particular application. To explore the transition of SDN, where the behavior shifts from capture to streaming, experiments were conducted.

5.3 Materials and methods

5.3.1 Device fabrication

DEP chip with 3D carbon electrodes was used for experimentation. Device fabricated in this work featured 180 rows, each row featuring 5 electrodes all arranged in straight columns. Electrodes were 100-µm high and 50 µm-in diameter. The separation between the centers of the electrodes in the x-axis (C_x) was 122 µm, while C_y was 105 µm. A 0.6 mm-wide, 3 cm-long channel was cut from a 127 µm-thick double sided pressure sensitive adhesive, or PSA (Switchmark 212R, Flexcon, USA) and adhered to a previously prepared acrylic holder, in a process described previously[181]. This arrangement was then manually positioned around the carbon electrode array and sealed using a rolling press. The voltage drop across carbon electrodes is influenced by the resistivity of carbon. Hence, when 20 V peak to peak (Vpp) are applied to the system, the

net voltage is about 15 Vpp [48]. But while referring to the applied voltage in this work, only the net voltage applied to the system is reported.

5.3.2   Experimental samples

Two different experimental samples were used: 1) suspension of 1 um-diameter particles, 2) mixture between 1 and 10 um particles in equal parts. Relative permittivity of the particles is taken to be 2.5. *C.albicans* cells were used with sugar solution with conductivity of $2.5*10^{-3}$ S/m. The cell concentration obtained was $\sim 10^6$ cells/ml. The sample preparation process is detailed in Section 1.2.5 of Chapter 1.

5.3.3   Experimental protocol

Experimental samples were flowed through the DEP device using a syringe pump (FusionTouch 200, Chemyx, USA) to determine a flow velocity in the range 0. 022-0.088 m/s for a given experiment. The voltage in the domain was varied from 10 to 20 V peak to peak and the frequency was varied from 10 kHz to 10 MHz (using a BK Precision 4052 Function Generator, USA). Experiment was recorded using a Nikon Eclipse LV100 equipped with a fast camera (Andor Zyla). Similar experiments were also conducted to demonstrate streaming behavior with *C.albicans* cells. Initially the channel was filled with the cell sample to establish the flow. Once a steady flow was established, the electric signal was switched on. The sample was flowed through the device for 1 min in each case, after which the images for the streams were recorded.

5.3.4   Data analysis

The image stacks recorded during experiments were analyzed using ImageJ software. The light intensity of the image at the outlet was recorded in each case. The image intensity was recorded for the case where the field was switched off and designated as 'control'. The relative intensity of the images with respect to the control was calculated, by normalizing the difference in intensity of experiment and control. The regions where the particles formed focused streams showed high light intensity on the image. The width of the regions where the intensity showed peaks was measured with respect to the device width. This is characterized as the stream width of the focused particles. The stream width was measured at the end of three intermediate electrode rows to avoid the effect caused by the channel boundaries and the electrode rows at the edges of the device. The resolution of the measurement is limited by the microscope imaging system which is ~0.1μm. Of note, this procedure did not allow to quantify the concentration of the streams. Instead, two representative cases of SDN where at least 80% and 100% of the particles in the selected domain form focused streams are studied. Hence, the values of SDN were calculated for $X_{in}^* = 0.8$ and 1. If a particle enters the domain at $X_{in}^* = 0.8$ and exists at certain X_{stream}^* value, all the particles entering the domain with a smaller X_{in}^* will elute at a smaller distance . Thus considering the case of $X_{in}^* = 0.8$ contains the behavior of all particles entering at smaller distances or 80% of the particles. Similarly, $X_{in}^* = 1$ encompasses the behavior of 100% of the particles.

5.4   Results

5.4.1 Effect of flow rate

For the 1 um polystyrene particles, streaming was observed at the h of around 10 μm. The velocity U_{ah} is calculated for h=10 μm and used for SDN calculations. SDN values were calculated for different flow rates and were seen to increase with the increase in flow rate. Particle focusing was evident in the velocity range of 0.022-0.088 m/s streaming. This is shown in, the streamwidth plot in the Figure 5. 2a. The SDN values for $X_{in}^* = 1$ in this range are above 0.7. At the flow velocity of 0.044 m/s, the SDN for $X_{in}^* = 1$ exceeds 1. The SDN for $X_{in}^* = 0.8$ at 0.044 m/s is around 0.6. The SDN value for $X_{in}^* = 0.8$ reaches 1 beyond the flow velocity of 0.07 m/s. Figure 5. 2b, shows the intensity of the stream at the central row of electrodes for different velocities against the channel width. With the increase in flow rate, the stream intensity decreases, indicating that less number of particles form focused streams at higher flow rates. This behavior is compared with SDN values seen in Figure 5. 2a. As the SDN for $X_{in}^* = 1$ exceeds 1, 100% of the particles are no longer streamed, although SDN for $X_{in}^* = 0.8$ is smaller than 1 indicating formation of streams by 80% of the particles. Though streams are formed, only 80% of the particles form these and the intensity decreases. Beyond the flow velocity of 0.08 m/s, SDN values for both cases are higher than 1 and no visible streams are seen as predicted by SDN values. This is the region where drag force dominates over DEP. For the velocities smaller than 0.028 m/s, where the SDN value is smaller than 0.7,

no streams are seen.
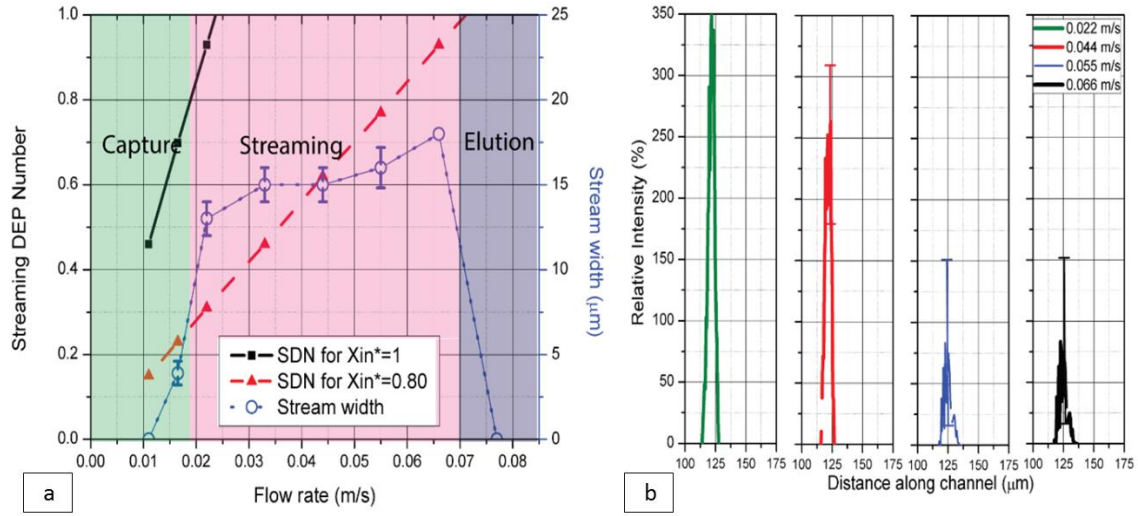
Figure 5. 2 Change in stream width with flow velocity. a) The value of stream width with the change in flow rate is plotted along with the calculated SDN values for $X_{in}^* = 0.8$ and 1. The SDN values increase with the flow rate and the stream width. b) Relative intensity analysis for stream from the central electrode array for flow velocities between 0.022-0.066 m/s shows decrease in stream intensity with rise in flow velocities.

5.4.2 Effect of voltage

The value of SDN is calculated for different voltages and decreases with increasing voltage as shown in Figure 5. 3a. With the increase in voltage, the DEP force increases. Stream formation is obtained in the voltage range from 12-20V as seen in the figure. For voltages between 10-14 V, the SDN value calculated for $X_{in}^* = 0.8$ is in the range of 1 to 0.65. Beyond the voltage of 18 V, the SDN value for $X_{in}^* = 1$ is smaller than 1, indicating that 100% of the particles will be streamed. The Figure 5. 3b indicates the intensities of

the streams obtained at different voltages. With the increase in voltage, the intensity increases implying that more and more particles are focused. This is validated by the fact that SDN value for $X_{in}^* = 1$ is smaller than 1 at higher voltages indicating 100% particle streaming.

At low voltages, (< 12Vpp) streams were not seen in the domain, where the SDN values are greater than 1. This behavior can be due to the dominance of drag over DEP force. At voltages beyond 25 V, the hypothesis is that DEP force will become dominant and result into higher particle capture.

As the particles are captured at the electrode, a layer of particles is formed around the electrode. It is hypothesized that the captured particles along with the electrode together behave as an effective electrode, which is bigger than the actual electrode. The formation of a layer due to the presence of particles results in additional domain for the transfer of charge from the electrodes and can cause decrease in the effective voltage. The SDN value increases with the increase in r_e and decrease in voltage. Higher SDN values imply the tendency of the system to show particle focusing rather than trapping. Eventually, after few layers of particles, the electrode can get saturated and no longer capture particles. The capacity of the electrodes to capture particles gets exhausted resulting into streaming in this case. A similar saturation in DEP device was observed by other authors [182][96]. Thus the parameters showing particle capture can eventually show streams with a small stream width as visible in the experiments.
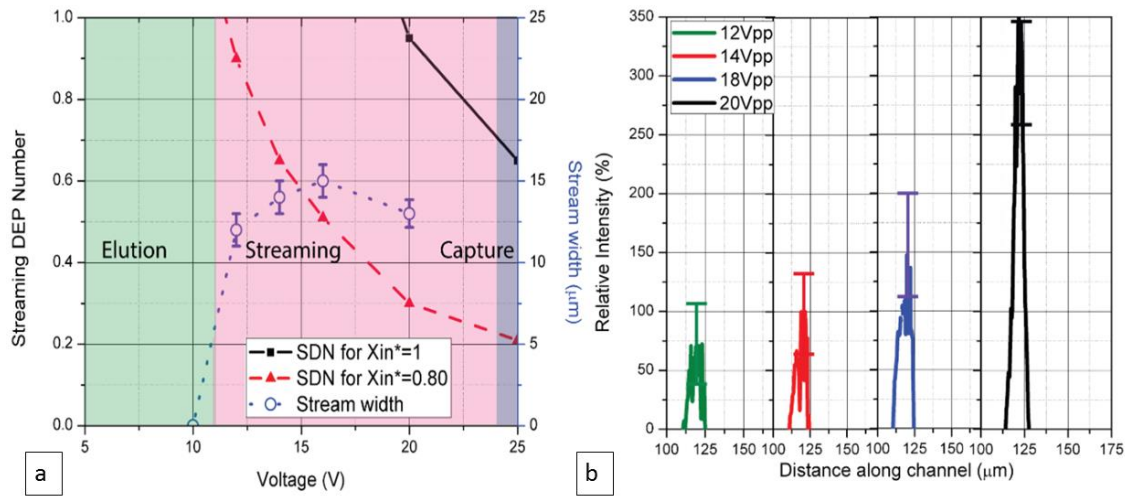
Figure 5. 3 Change in streamwidth with voltage. a) The value of stream width with the change in voltage is plotted along with the calculated SDN values for $X_{in}^* = 0.8$ and 1. The SDN values and stream width decrease with the increasing voltage. b) Intensity analysis with ImageJ conducted for streams obtained at 12 V and 18 V in comparison to the control which shows no presence of streams. The peaks marked in the image correspond to the streams.

5.4.3 Effect of field frequency

The SDN values for different frequencies are plotted in Figure 5. 4a. The SDN value shows an increase with the increase in frequency. Frequency behavior of the latex particles is determined by the value of real part of Clausius Mossotti factor $Re[f_{CM}]$ (Appendix B). Based on the results, the SDN value for $X_{in}^* = 1$ for the frequency of 100 kHz is around 0.8. Particle focusing is seen at this frequency. With the increase in frequency beyond 100 kHz, the SDN value increases. At 1000 kHz, the SDN value for $X_{in}^* = 1$ and 0.8 are both close to 1, and transition from streaming to elution behavior is expected. A closer look at Figure 5. 4 b indicates the increase in intensity of stream with increase in frequency from 100-500 kHz, whereas at 1000 kHz, the intensity drops indicating decrease in the stream formation, which is true to the prediction of SDN values. With the increase in frequency, the Clausius Mossotti factor of latex beads goes on decreasing and as an effect, the DEP force also decreases. As the drag force becomes dominant, stream width increases. Beyond the frequency of 1000 kHz, DEP force is weak and drag is dominant, leading to hydrodynamic streaming without any particle focusing. At low frequencies, the DEP force dominates the drag force, leading to high amount of particle trapping. At higher frequencies, drag force starts dominating. This results into particle focusing and streaming behavior. After a certain maximum flow rate, particle focusing is no longer visible as the drag force is exceedingly dominant.
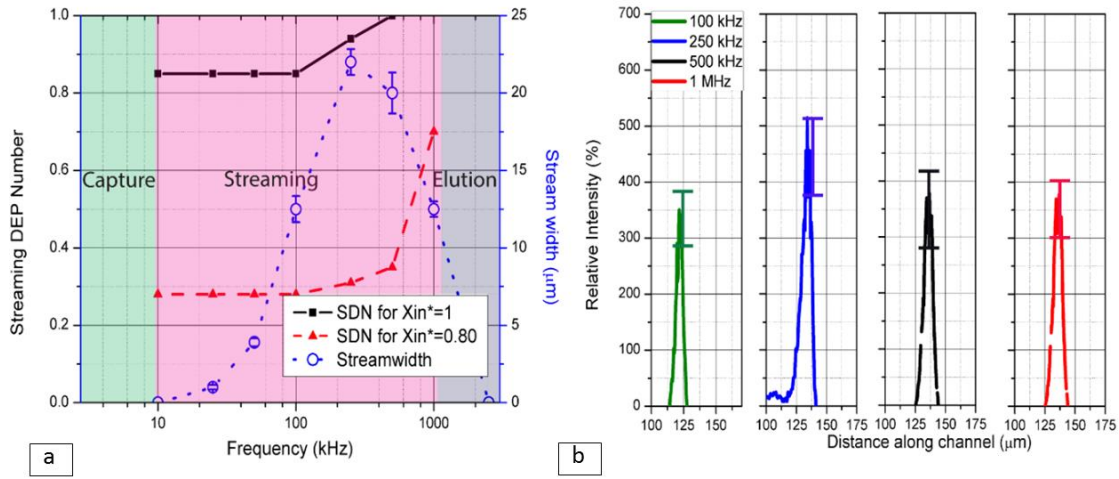
Figure 5. 4 Change in streamwidth with frequency. a) The streaming DEP number are calculated and plotted for different frequencies. The SDN values are plotted for $X_{in}^* = 1$ and $X_{in}^* = 0.8$. b) Intensity for streams with change in frequency is plotted and it shows that the maximum stream intensity occurs at 250 kHz.

5.5 Discussion

1 μm latex beads show positive DEP in the range of frequencies applied in this study. The latex beads in the domain, can either flow without any influence of DEP force, get captured at the electrodes or deviate due to the DEP force and flow in focused streams. When the DEP force is dominating, the 1 μm latex beads get captured at the electrodes by positive DEP. As the drag force increases, the particles begin to flow along the electrodes forming streams. When the drag force becomes exceedingly dominant, the particles flow without any influence of DEP. Based on this phenomenon, three zones can be defined. The capture zone indicates high particle capture or trapping DEP, streaming zone indicates focused streams formed by the combined action of DEP and drag forces

106

and elution zone indicates particles flowing without any effect of DEP. Based on the experiments the range of SDN values from 0 to 0.7 were determined to signify particle capture. When the SDN value is greater than 0.7, but less than 1, we define the region as streaming zone. For SDN values greater than 1, the particles get eluted. SDN value is the ratio of the time take by the particle to travel in x direction to desired focused length to the time taken to travel the actual channel length.

Thus, a small SDN value implies that the particle reaches the desired focus position much before it reaches the end of the channel. Such a particle will likely get trapped before it reaches the end of the channel. If the SDN value is more than 0.7, it implies that the particle has travelled more than 70% of the channel length before it gets focused. Such a particle will likely form a focused stream. Choosing 70% of the channel length allows for further room for particle focusing before the particle reaches the end of the channel. Having SDN value as close as possible to 1, makes an ideal case for focusing. The streaming with 1 µm polystyrene particles is seen at around the height of 10 µm in the current microchannel. We hypothesize that this is because the flow velocity at this height is favorable for streaming behavior; i.e the drag and DEP force are effectively balanced. The flow velocity along h is parabolic and decreases with the height from the center of the channel. The velocity at the height of 10 µm enables the formation of streams with higher efficiency. At low flow velocities, the streaming is observed in the entire channel. In addition, the small electric field gradient created by the leads connecting the carbon electrodes, attract the particles closer to the bottom of the channel. For enabling particle separation, streaming should be shown by the particles in the entire

channel. The SDN value increases with increase in flow rate. The maximum velocity of the flow occurs at the distance *h=H/2* and the SDN value should be calculated at this value for designing streaming DEP devices.

Streaming DEP number can provide a qualitative idea about the behavior of the device, in terms of the zone where the device operates. Current analysis relies on the application of drag and DEP force on the particle to determine the particle movement. When the particles are close to the electrodes, i.e the particle-electrode distance is comparable to particle size; the presence of particle can alter the charge density around the electrode [183] .As the electric field travels through the particle, the net electric field in the domain changes. Correction factors have been introduced by other authors to account for these perturbations [5,184]. This can affect the particle trajectory very close to the electrode. As the particles approach the electrode, there is a tendency to form particle chains[185] and this can affect the effective particle size that has been considered for analysis. The electric field created by presence on one particle can affect the movement of the neighboring particles [186][187]. The DEP force acting on the different particle members of the chain varies and this variation can affect the particle trajectory. The near wall effects can also cause the velocity of the particle to reduce and corresponding corrections have been introduced previously [188]. As the spacing between the electrodes decreases, the effects of flow separation or formation of vortices affects the particle movement and neglecting the x component of the velocity will not be possible. Future work will focus on implementing these factors to further strengthen the analysis for the streaming DEP number. The shape of electrodes in this case is

cylindrical. The electric field profile and flow profile depend on the cross sectional shape of the electrode. Another objective of the future work will be to implement a shape factor based on the relation between electrode cross section and electric field profile. Such a shape factor can enable generalization of the streaming DEP number for electrodes other than cylinders.

SDN value was calculated for the streaming DEP device used in the experiments conducted by Cummings et al.[170,189]. The device showed streaming behavior for polystyrene particles at the parameters used calculated for this work (Appendix B).These works use electroosmotic flow rather than pressure driven flow. In the analysis for this work, the velocity U_a corresponding to the electrophoretic velocity calculated from these references is used. Additionally, the value of DEP voltage used for this analysis is based on the DEP force calculations using COMSOL simulations for the device detailed by Cummings et al. The array of cylindrical posts was used for focusing of 200 nm polystyrene beads and the stream width is estimated to be about 8 μm, based on the images of streams shown in these references. SDN calculated for these values is 0.73. This number lies in the streaming region and indicates streaming as observed by the authors of these works.

5.6 Summary of findings and contribution

Streaming with positive DEP is a potential separation method, which has not been intensively explored. The particle trajectory in streamingDEP depends upon the action of the DEP and drag forces. This particle behavior was analyzed and a non-dimensional

streaming DEP number (SDN) was proposed. SDN values obtained for streaming DEP with polystyrene particles were used to validate the focusing behavior. Based on this, the range of SDN values from 0-0.7 imply particle capture, values from 0.7-1 indicate formation of focused streams and SDN values beyond 1 indicate particle elution. SDN can serve as a qualitative tool to predict the streaming behavior of the DEP device based on the design parameters. It can also be used as a design tool to obtain the required parameters for streaming DEP by selecting SDN value in the streaming range.

CHAPTER SIX

ROBOTIC DIELECTROPHORESIS (ROBODEP)

(Computational study of conical geometries presented in this chapter is from -Natu, Rucha, Monsur Islam, and Rodrigo Martinez-Duarte. "Carbon cone electrodes for Selection, Manipulation and Lysis of Single cells." *ASME 2015 International Mechanical Engineering Congress and Exposition*. American Society of Mechanical Engineers, 2015)

6.1 Introduction

Automation using liquid handling robots is a crucial part of life science laboratories for dispensing and transferring small volumes for reagent liquids, compounds, samples of DNA and cells in genetic research [190,191], bioanalysis [192–194], sample preparation [195,196] and high throughput screening in pharmaceutical industries [197,198]. Though liquid handling systems enable rapid, high throughput, consistent and parallel liquid movement [199,200], these devices have a limited cell sorting ability. Cell sorting is mostly based on size, morphology and spectral features, analyzed using image intensity for the cells [201][202][203]. Image analysis techniques generally rely on staining or labelling the cells, and can only be used for specific cells. Moreover ability to sort cells has limitations for cells with similar sizes.

In the presented device, aim is to extend the use of DEP to sort and selectively pick cells based on their inherent properties and combine it with the capabilities of the well-established technique of liquid handling robots to transport and transfer the cells at

specific locations. In the envisioned device, the electrode chip will be a modular unit that will be mounted on the liquid handling robot, which will selectively trap cells by dielectrophoresis, automatically transport them to required sites where they can be integrated with the further analysis steps. This process, thus integrates the functions of cell sorting and cell placement with the sample handling robotic setup. In this work, the feasibility of such a system is demonstrated and further steps are taken to study the parameters that affect the performance on this setup.

The robotic pick and place device consists of three steps. During the first step, i.e pick, the selected cells are picked up from the mixture of cells using dielectrophoresis (DEP). The second step is the wash step where the unwanted cells sticking to the chip are washed off and during the third step, which is termed as place, the cells are deposited on the grid for further analysis. Figure 6. 1 shows a schematic of the steps executed during this process. Various physical phenomena become important at different stages.
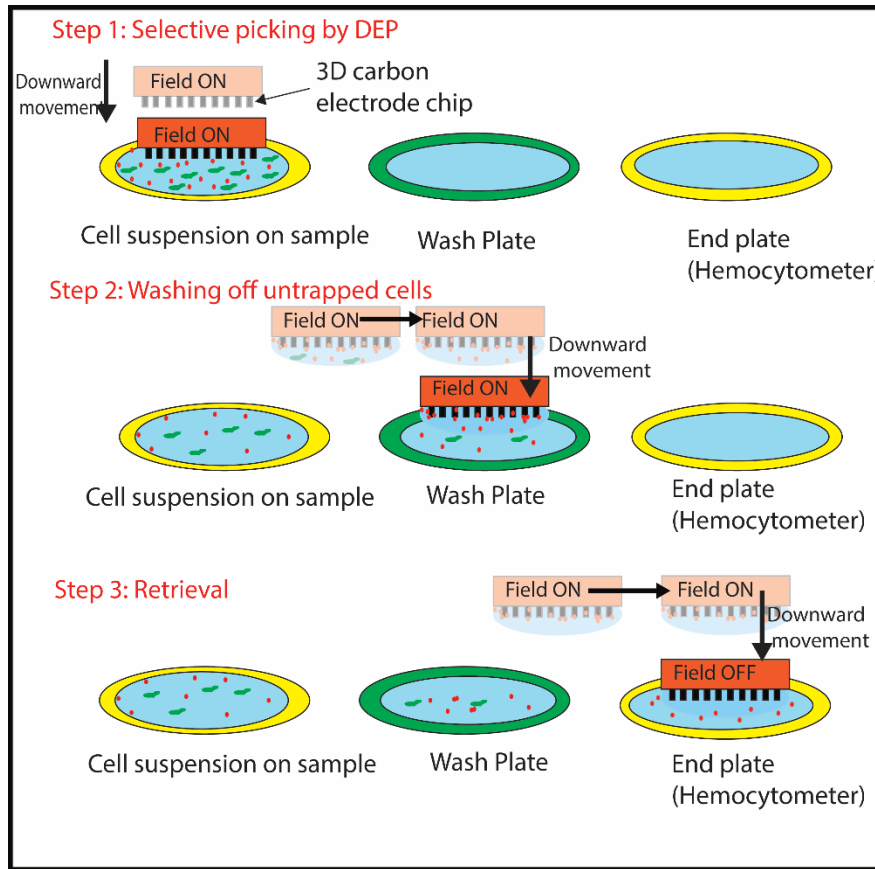
Figure 6. 1 Schematic of the robotic DEP device with the three steps: Pick, wash and place.

6.2 Materials and Methods

6.2.1   Experimental setup

The 3D carbon electrode chip used in this work was fabricated by the process of SU8 photolithography followed by pyrolysis in an inert atmosphere. The fabrication procedure has been in Chapter 1, Section 1.2.3. Device fabricated in this work featured 50 rows, with intercalated arrangement of electrodes; each of them 100-μm high and 50 μm-diameter. Indium leads were soldered on the carbon pads and conducting copper tape

of thickness around ~70 µm was used to make electric connections with the chip through indium. The copper tapes were covered with a thin layer of epoxy to avoid contact with the cell culture. The chip was held on the modified printer head using pressure sensitive adhesive.

In this work, A2 Delta 3D printer (Afinibot, Shenzhen, China) was used as the robotic system. The extrusion probe, held by three supporting arms in this printer was replaced by modified printer head to house the 3D carbon electrode chip. The arms enabled 3 dimensional movement of the header and hence the chip. The electrical connections for the chip are held on the header. The stage consisted of a glass plate divided into three sections, namely for cell culture, wash and place. The header is mounted such that, the chip faces the glass plate. Figure 6. 2 shows the setup for this device.
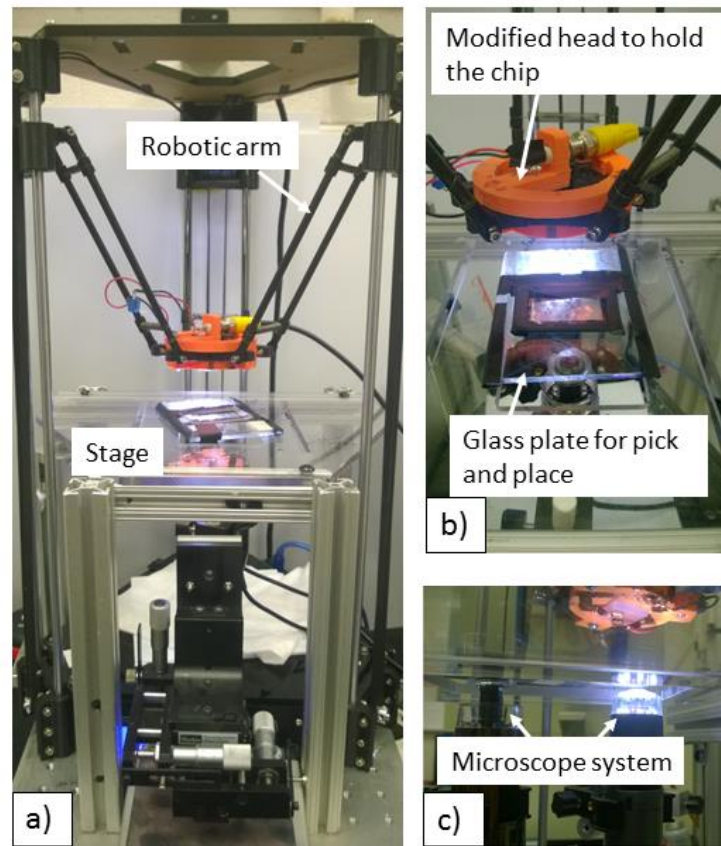
Figure 6. 2 Experimental setup for robotic DEP operation. a) The 3D printer, which is used here as a robotic manipulator for the electrode chip is combined with a stage. The stage hoists the glass plate for the experiment. b) The modified printer head which holds the 3D carbon chip at its electrical connections is visible in this image. The glass plate on the stage is divided into three sections, culture section, wash section and place section separated by black electrical tape. c) Two microscopes are arranged below the stage, one below the cell culture section and other below the place section. These handheld microscopes are mounted using 3 axis adjustable stands.

6.2.2 Experimental samples

The cell sample preparation process for these cells is detailed in Section 1.2.5 in Chapter 1.Yeast strains of *C.albicans* and *C.tropicalis* were used in this work. The average cell size for *C.albicans* is 4-6 μm and for *C.tropicalis* is 4-8 μm[83] For studying the cell separation, the *C.tropicalis* cells are mixed with 10 μm latex particles in sugar solution.

The Rat Adipose Stem Cells (RASC) are also used for this experiment. These cells are washed with sugar solution in a way similar to the candida cells, except that the conductivity of the sugar solution was adjusted to 120 μS/m. For the experiment with cell separation, non-viable stem cells are obtained by heat treating the cells for 20 min at the 70˚C. At this conductivity, we observed that the viable cells showed positive DEP whereas the non-viable RASCs showed negative DEP. The cell viability is assessed by using Live/Dead Viability/Cytotoxicity Kit (Thermo Fisher Scientific, Waltham, MA) which is prepared with 20μl of 2mM EthD-1 and 5 μl 4mM calcein AM in 10 ml sterile tissue culture-grade D-Phosphate-buffer saline (PBS) (Thermo Fisher Scientific, Waltham, MA).

6.2.3 Experimental protocol

Around 10 μl of cell culture was pipetted on the culture section. The wash section was filled with DEP media. A glass plate with grid was placed at the place section. The movement of the header was controlled by the use of the software Repetier host. The

116

robotic arm first moves to the cell culture section, such that the carbon chip lands in the cell culture. During this step, the voltage is switched on. The cells are captured by DEP and as the chip rises above the cell culture section, cells are carried with the chip. The next step is the wash step and is required to get rid of the contaminants. In this step, the chip gets immersed in the wash section and is transported in the wash section at a desired speed. In the third stage, the chip is transferred to the place section, where it is positioned on the glass grid plate. During this stage, the electric supply is switched off to release the cells captured. In this way, the selected cells from the cell culture section can be successfully transferred to the place section by an automated robotic device.

6.2.4   Data analysis

The numbers of cells for each experiment were counted in the place section. The cells during place step are dropped on a hemocytometer grid in 10 µl of liquid. These cells are then covered with a glass slide and counted. Number of cells within 1 cm^2 of the hemocytometer grid is counted manually under the microscope. For the cases where Ti electrodes are used for collecting placed cells, the number of cells which is visible in the plane of the Ti electrodes are counted. The process is repeated at least 3 times for each experimental case. The standard deviations in different experiments with similar parameters are plotted as error bars on the graph.

6.3 Results

The robotic cell transfer was feasible by the use of electrode chip. For each of the steps involved in the process, different parameters play an important role. The study of each step and involved factors is given below.

6.3.1   Pick step

At this stage, the electrodes get immersed in the cell culture and the cells are captured at the electrodes by DEP force. Once these cells are captured, they will be carried with the chip and transferred further. Thus, the ability of the cells to remain attached to the electrodes during the lift up is important in this stage. The DEP force acting on the cells depends upon the Clausius Mossotti factor for the cell-media system, the cell size, shape and the applied electric field.

The electric field depends on the voltage applied to the system, and it was expected that, at higher voltage, the number of cells that can be trapped and retained during the transfer will be higher. The results obtained for number of *C.albicans* cells transferred at the voltage of 5, 10 and 20 Vpp are shown in Figure 6. 3a. The voltage of 20 Vpp enabled the transfer of highest number of cells, followed by 10 Vpp. This implies that the DEP force variation due to the change in voltage is an important factor during the pick stage.

The DEP behavior of the cells depends on the Clausius Mossotti factor which can be varied by changing the frequency of the electric current. With the change in frequency, the corresponding DEP force will change and affect the number of cells being picked and

retained. In case of *C.albicans*, it was observed that the number of cells picked increased with the increase in frequency from 10 kHz to 100 kHz and was maximum at 100 kHz. Beyond this frequency, the number of cells captured decreased. The control in Figure 6. 3b indicates the number of cells transferred without DEP. It is speculated that these are the cells which reach the place section due to the wetting of the chip. The difference between the control and the experimental cases is the number of cells which are actually transferred by the action of DEP. At 10 kHz, we observed that the *C.albicans* cells show negative DEP and thus we expected that the cells should not be captured at this frequency. In the Figure 6. 3b, at 10 kHz, a negative difference was seen between the number of cells transferred in the experiment and in control. Similar study was conducted with *C.tropicalis* cells, which shows a slightly different DEP response than *C.albicans*. The results obtained with *C.tropicalis* are shown in Figure 6. 3c.

Assuming the cells used here as spherical cells, the effect of cell size, applied voltage and Clausius Mossotti factor were tested for the performance at pick step. To study the effect of size of cell, two different types of cells, *C.albicans* (diameter~4µm) and RASCs (diameter~20 µm) were studied. Both type of cells could be attracted at the electrodes and transferred successfully, implying the feasibility of the method irrespective of the cell size. Figure 6. 3d shows the image of *C.albicans* captured at the electrodes. The number of cells captured and retained during the entire process depends on the cell concentration.
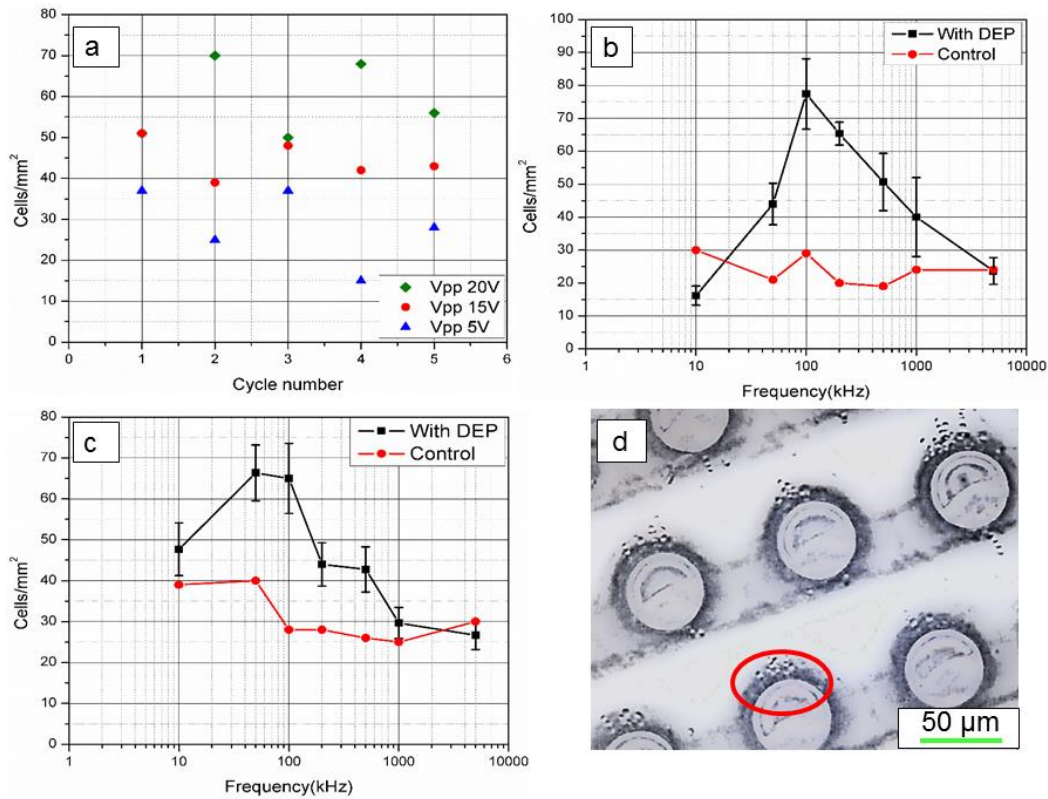
Figure 6. 3 Output during Pick step with change in system parameters. a) The output as obtained at different voltages in the experiment. As expected, the cell output for *C.albicans* increases with increase in applied voltage. b) The behavior of capture and transfer for the *C.albicans* cells with the change in DEP frequency is shown in this image. The control in this case indicates the number of cells transferred without DEP i.e cells carried by the liquid wetting of the device. With the increase in frequency, the number of cells being transferred to the place section by DEP changes, with maximum cell transfer occurring at 100 kHz. c) The behavior of capture and transfer for the *C.tropicalis* cells with the change in DEP frequency is shown in this image. The control indicates the number of cells transferred without DEP.d) *C.albicans* captured at the electrodes during the pick step.

6.3.2 Wash step

It is speculated that the transfer of cells in the previous control experiments was due to the wetting of the chip. During cell separation, when only particular type of cells is required, wetting can cause contamination. It must be eliminated to increase the purity of the cells placed. Wash step is required to eliminate the cells which are not captured by DEP. Wetting of the chip occurs when the chip and the surrounding connections get immersed in the cell culture. Along with the liquid, unwanted cells also get carried with the chip. This behavior increases if the chip and connections have rough surfaces which make them hydrophilic. We did not observe any direct relation between the number of cells carried by wetting and the cell size.

During this step, as the chip travels in the wash tank, the cells are subjected to drag force from the moving fluid, which causes the uncaptured cells to move and disperse in the wash tank. The device here uses microelectrodes with the gap between electrodes being around ~80 μm. The footprint of the electrode chip is approximately $2.5*2.5$ mm^2, whereas the footprint of the tank is approximately $40*40$ mm^2. As the chip and the header move through the tank, the gap between the electrodes provides resistance to the flow and the liquid tends to flow around the electrodes rather than between them. To enable the liquid to flow from the region between the electrodes, the movement of the chip in the wash tank is repeated. The number of repetions of this cycle is also a control parameter for the wash step.

COMSOL based modelling was used to study the velocity v around the electrodes for robotic speeds U. It was observed that, as U increases, the electrodes on the edge of

the chip are subjected to high velocity, but the electrodes within the array provide

resistance to the flow as shown in Figure 6. 4b. Based on these results, we simulated the

behavior of chip at different speeds of the header (100mm/min or 0.0017 m/s-5000

mm/min or 0.083 m/s). The $Re[f_{cm}]$ was assumed to be 0.75 for *C.albicans* and

C.tropicalis at 100 kHz. (This value is based on the $Re[f_{cm}]$ value for *S.cerevisiae* cells

which belongs to the same family of cells, saccharomycetaceae). The permissible

velocity u calculated from Equation (2. 22) in Chapter 2 is thus smaller than 0.001 m/s at

the electric field gradient ~ 10^{15} V^2/m^3 which is seen for the cylindrical carbon electrodes

at 20 V as calculated in previous work[54]. A velocity value comparable to this can be

achieved at the header speed of 2500 mm/min or 0.041 m/s. Figure 6. 4a shows the

permissible velocity value at ∇E^2 of $10^{15}V^2/m^3$ to $10^{14}V^2/m^3$ and the average velocity

within the chip at different header speeds. Based on the values in this figure, header

speed of 0.041 m/s was considered ideal for wash. Further experiments were conducted

with *C.albicans* to test different speeds with different number of repetions.

Different speeds and number of runs in the wash tank were tested for the number of

C.albicans cells carried by the chip through wetting when the DEP signal is off. The

results are shown in the graph in Figure 6. 4c. The error bars indicate the randomness

occurring during these runs. The number of cells being transferred decreases with the

increase in speed and with the number of runs. This shows that, by increasing the number

of runs and speed, it was possible to get an effective contact between the chip and the

liquid. With the increase in speed and number of runs, the error bars became smaller,

implying that the results obtained were more consistent. The runs in Figure 6. 4c were

optimized for *C.albicans* cells. The wash speed used for *C.albicans* was also used for *C.tropicalis* as these cells show similar size and DEP response at 100 kHz. According to the Equation (2. 22), the speed used for RASCs should be larger than that used for the candida cells due to the increase in size. However, it was observed that the cell transfer output at these speeds was very low. The $Re[f_{cm}]$ for these cells is not known and hence calculating the velocity was not possible theoretically. Additionally, the size of these cells is comparable to the gap between electrodes and thus, we believe that the presence of the cell will affect the electric field in the domain. The speed for wash will depend on these parameters. In this work, the speeds of header used varied from 5 to 50 mm/min. The best results were obtained for 20mm/min of wash speed and this speed was used for the experiments with viability retained for 95% of the cells.
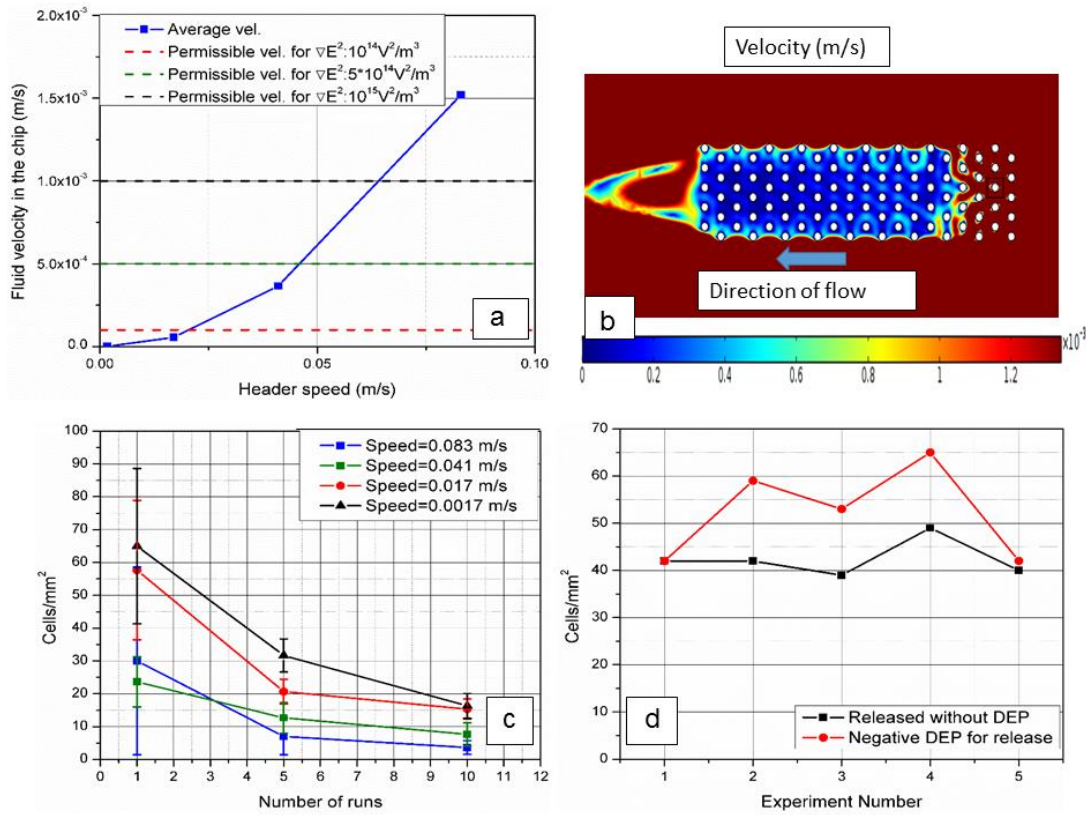
Figure 6. 4 Optimization of the wash step. a) The average velocity in the chip that was calculated using simulation and the permissible velocity from Equation (2. 22) are plotted. b) The chip provides resistance to the flow and thus the flow within the chip is very low compared to the flow around the chip as seen in simulation. c) To eliminate the contamination the wash step was operated at different number of runs and speeds. The speed of 0.083 m/s and 10 runs give the minimum contamination for *C. albicans* cells. The number of cells that were carried by the chip when the field is off is shown for different wash speeds and number of runs. With the increase in wash speed and number of runs, the number of cells carried reduces. d) Number of cells transferred by using negative DEP in comparison to cells transferred without DEP is shown.

6.3.3 Place step

The third step in this experiment is the place step. When the electric signal is switched off, it is expected that the cells are released on the grid plate. These cells are expected to settle down at the specific locations on the plate where they can be analyzed. Some cells adhere to the electrodes once they are captured. These cells can remain adhered to the electrodes in spite of the electric signal being switched off. Secondly, when the cells are released, their movement is influenced by the liquid on the grid plate and they do not readily settle at the specific locations.

The adhesion depends on the properties of cell and the electrode surface. If the cells remain adhered to the electrode, they need to be pushed away from the electrodes. Some of the ways to do this would be to change the frequency of the electric field so that the cells show negative DEP or increase the media conductivity so that the cells show negative DEP or electroosmosis, use of reagents like trypsin or surfactants to reduce the adhesion. In these experiments, negative DEP was used to release *C.albicans* from the electrodes (at frequency of 10 kHz). Figure 6. 4d shows the graph where the number of cell released by negative DEP and by switching off the electric field is compared. A small change in the amount of cells released was seen in this case for *C.albicans*, but it can be a possible method to improve cell release with other cells which are adherent. (eg. Endothelial cells)

An important consideration during placing the cells will be placement at specific locations. In the current device, the liquid on the grid plate inhibits proper placement of the cells. To resolve this issue, we used DEP traps to locate the cells in the place section.

2D titanium electrode chips (Ti chips) were used as traps in the place of the grid plate in an experiment with pick and place of RASCs. Once the cells are released at the place section, the electric field on such a device can be switched on to trap the cells on the chip at desired positions. Some cells could be held by DEP at the electrodes on this chip. The use of 2D Ti electrodes in this case proved a limitation as cells that were in different planes could not be captured at the electrodes. The current device has a limited movement resolution (100 µm). We believe that, with a higher precision in control of the position of the electrode chip, the cells can be directly dropped on the Ti electrodes where they can be held with DEP.

6.3.4   Cell separation

Automated cell sorting and cell transfer is a major application for the envisioned device. Current device was tested for its ability for cell sorting. *C.tropicalis* cells were separated from mixture with 10 µm polystyrene beads using this device. At 100 kHz, the *C.tropicalis* cells show positive DEP whereas the 10 µm polystyrene beads show negative DEP for the media used here. This difference in the DEP behavior was used to selectively pick *C.tropicalis* cells and transfer them to the place section. The results for separation are shown in Figure 6. 5a. For the experiment in Figure 6. 5a, the initial ratio of cells and particles used was 3:17. The average concentration obtained after separation is 15.5:4.5. This shows that, it was possible to selectively pick the cells with high efficiency. The wash speed optimized in the previous step was used and low number of cells and particles were carried when the DEP signal was off. The control in Figure 6. 5a shows the percentage of cells which were transferred without DEP.

The separation of live and dead stem cells was also carried out using the device. These cells show similar size, but at 100 kHz, the live cells show a positive DEP whereas the dead cells show negative DEP. This difference in the properties was used to sort the live cells and transfer them to the place section. After the process was complete, the number of live and dead cells on the grid plate could be counted by imaging under the microscope with the live/dead viability stain.

The wash step was optimized for this experiment and the wash speed of 0.0034 m/s was used with 2 runs. The concentrations of live and dead cells used in this experiment was 3:7. The average separation efficiency obtained was 4:1. This proves that this device can be effective in separating and transferring selected cells. The results for separation of live and dead RASCs are shown in Figure 6. 5 a.
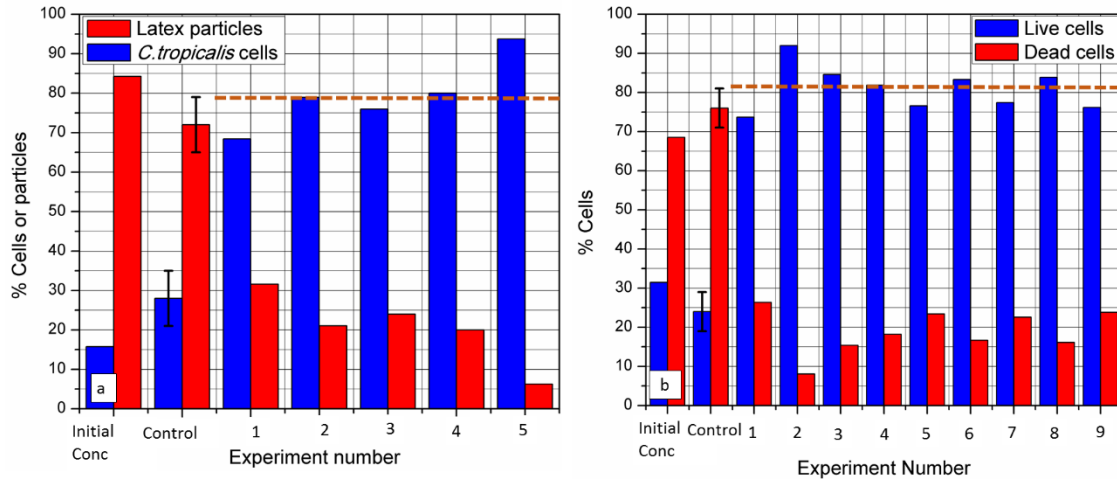
Figure 6. 5 Cell sorting using robotic DEP setup shows different cases with particle cell separation. The initial concentration is shown by the experiment no.0. The dotted line in each figure shows the average separation efficiency obtained for all experiments. a) This figure shows different separation experiments that were run to separate *C.tropicalis* cells

from the mixture of *C.tropicalis* and 10 µm latex beads. The initial concentration of cells to particles was 15-85%. At 100 kHz, *C.tropicalis* show positive DEP whereas the latex beads show negative DEP. This difference in the DEP behavior was used to selectively pick the cells and transfer them to the place section. The average efficiency in this case was 81%. a) Live and dead RASC were mixed in the ratio 30-70%. The live cells show positive DEP whereas the dead cells show low negative DEP at 100 kHz. This difference in DEP behavior was used to separate these cells. The average separation efficiency achieved in this case is 81%.

6.3.5 Single cell isolation

An important application for the automated pick and place device can be selective picking and transferring of single cells. A further step to electroporate or lyse the cells can also be incorporated at the place step by changing the applied voltage. In order to trap a single cell at an electrode, localized high gradient needs to be generated such that, the volume of the gradient is comparable to the cell volume. It is hypothesized that, for trapping a small cell as *C.albicans*, used in this work, a conical electrode geometry with a sharp tip having high local gradient and resulting DEP force will be required. In case of the RASCs, the cell diameter is between 20-30 µm and the cell volume is roughly 35,000 µm^3. Gradient generated at the edges of the cylindrical electrodes used in the experiments was high enough to trap a single stem cell when the cell concentration is low (10^3 cells/ml). Single cell picking of RASCs was thus achieved by this device by tailoring the cell concentration. The images in Figure 6. 6 a shows single cell captured at different

electrodes during the pick step. The Figure 6. 6b shows the number of cells transferred by this process. Control in this case indicates the number of cells transferred without DEP.

The 2D titanium electrode chip (Ti Chip) was positioned at the place section. When the cells were transferred to the place section, the electric field generated on the Ti chip was used to trap the cells and further increase in voltage resulted in swelling of cells. Figure 6. 6c shows the cells transferred to the Ti chip in the place section and Figure 6. 6d shows cells trapped at the Ti electrodes when the field is switched on. A separate experiment was conducted to study the effect of electric field on the volume of RASCs. Thus, this device was capable on integrating the process of single cell pick and cell transfer.
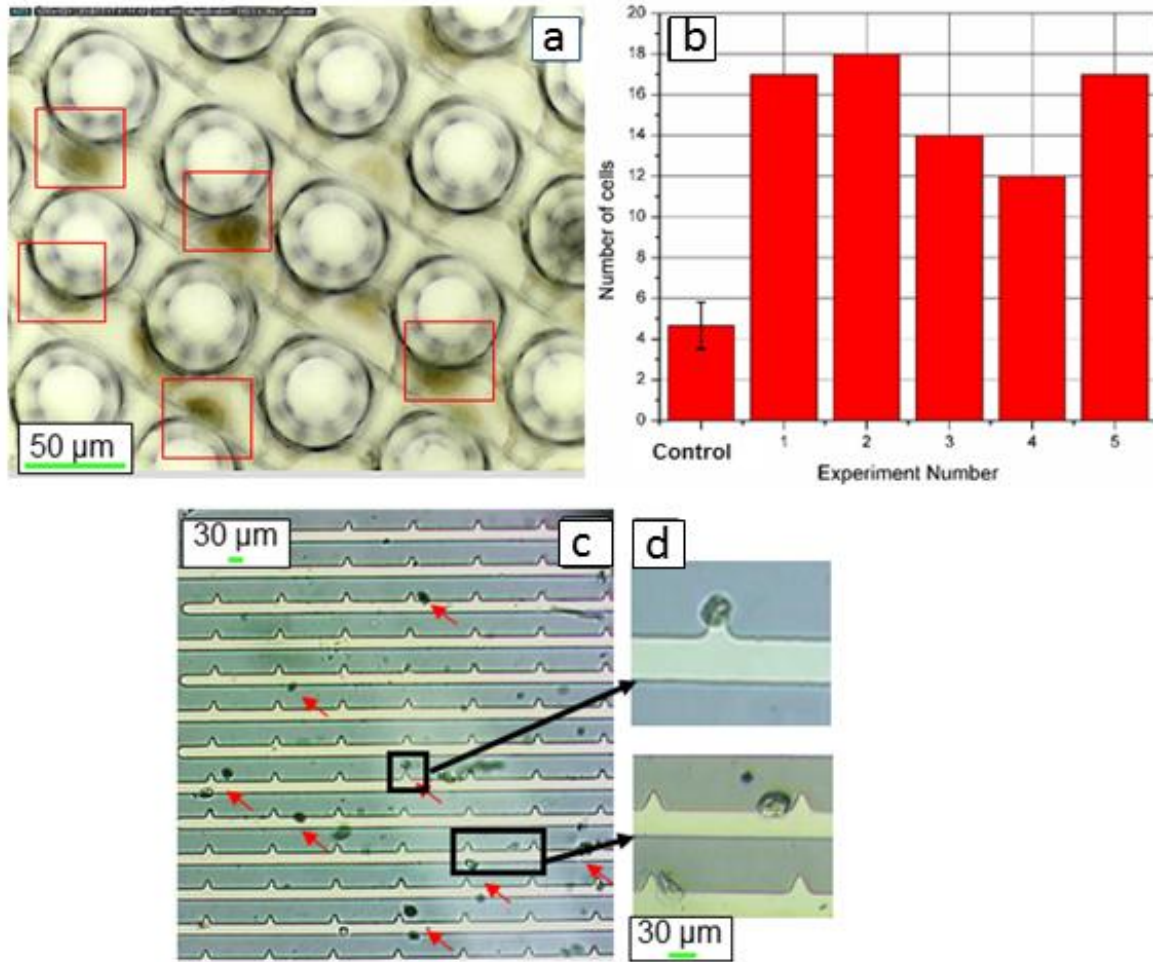
Figure 6. 6 Single cell pick and transfer using robotic DEP setup. a) This figure show single cells captured at the edge of the electrode in different instances. The size (dia) of the cell varies from 20-30 μm. b) Number of single cells transferred by pick and place are shown in this process. The control indicates the cells transferred without DEP .c) This image show the cells which were transferred to the Ti chip placed on the place section. Arrows are used to point out the cells placed on the Ti chip by this process. d) Different instances where the cells are captured at the triangular electrodes in the chip when DEP field is turned on are visible.

6.3.6 Computational study of conical electrode geometries

As stated in previous section, for single cell capture of smaller cells (dia ~4 μm) like *C.albicans* will require localized gradient of electric field. Computational model consisting of conical electrode geometries was studied to find the suitable electrode geometry for such a system. Geometry of an electrode dictates the distribution of electric field and gradient around the electrode. Electrodes of a shape of a cone with curved tips were characterized. This shape was selected as it gives an advantage of narrow tip, where the electric field and gradient is high. Conical electrodes are characterized by the base radius, the apex radius, and the angle made by the axis with the surface. The geometric model constructed is shown in Figure 6. 7a. Parameters considered are given in Table 1. 1. The electric field and electric field gradient for various conical electrode geometries as computed using computational model detailed in Chapter 2, Section 2.4.

A small block was defined around an electrode to calculate the volume of the region with electric gradient higher than 10^{18} V/m^3 around the electrode tip. This particular electrode was chosen to represent an electrode in the array surrounded by six other electrodes and thus influenced by their potentials. Material properties used in the model are shown in the Table 6. 1.
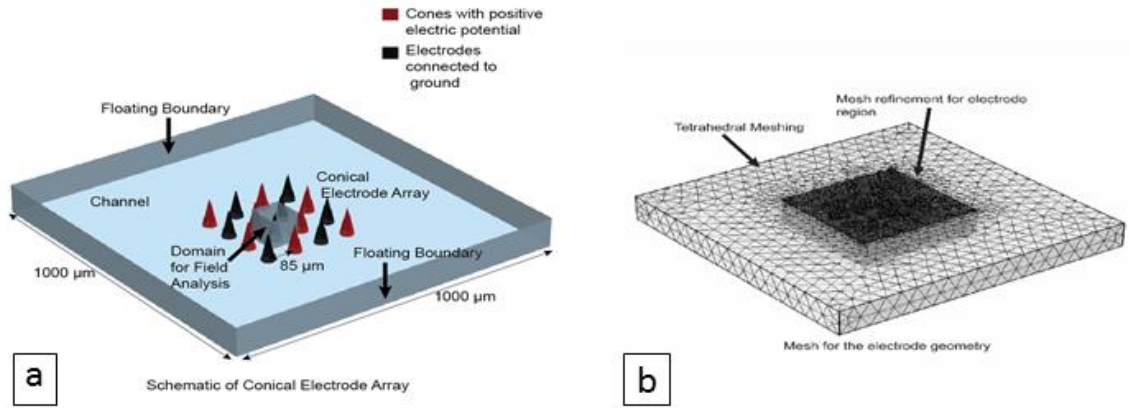
Figure 6. 7 Geometry for simulation of conical electrodes. a) Geometry for COMSOL simulation model. b) Mesh for COMSOL Model with implemented refinement

Figure 6. 8 a-c show the electric field and gradient simulated for a cone with semi angle 12˚ and 45˚ respectively. The high gradient region is concentrated at the tips of the geometry. The localized volume of high electric gradient (above 10^{18} V^2/m^3) is higher at 12˚ than at 45˚.
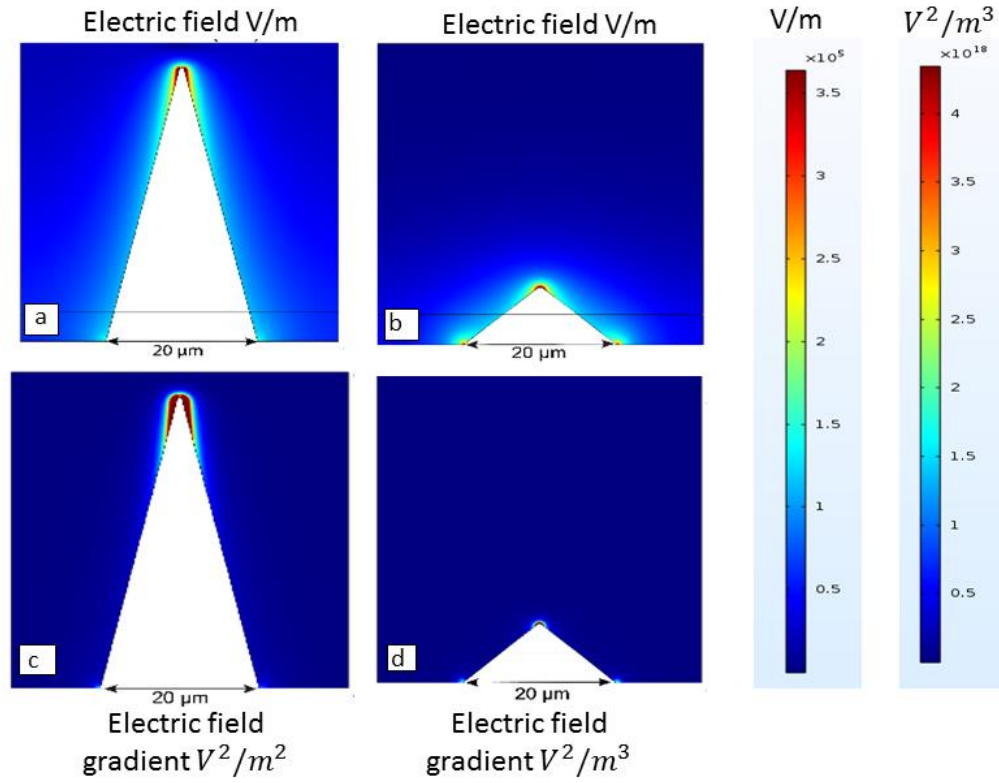
Figure 6. 8 Electric field simulated for conical electrodes. a) Electric field simulated for geometry with semi angle 12˚ and base radius 20 μm at 2V. b) Electric field simulated for geometry with semi angle 45˚ and base radius 20 μm at 2V. c) Electric field gradient simulated for geometry with semi angle 12˚ and base radius 20 μm at 2V. d) Electric field gradient simulated for geometry with semi angle 45˚ and base radius 20 μm at 2V. The color bars on the right represent electric field (V/m) and electric field gradient (V^2/m^3) in the domain.

The values for the maximum electric field were obtained at each angle and by using Equation (2. 39), the maximum electric field at which cells can be captured without lysing for the three frequencies of electric current, 10, 100, and 1000 kHz was calculated. It can be seen from Figure 6. 9a, that the values of electric field obtained at all angles other than 18° can successfully capture cells at the frequency of 100 kHz without lysis. Angles above 30° and the angle of 12°can are used for the frequency of 10 kHz.
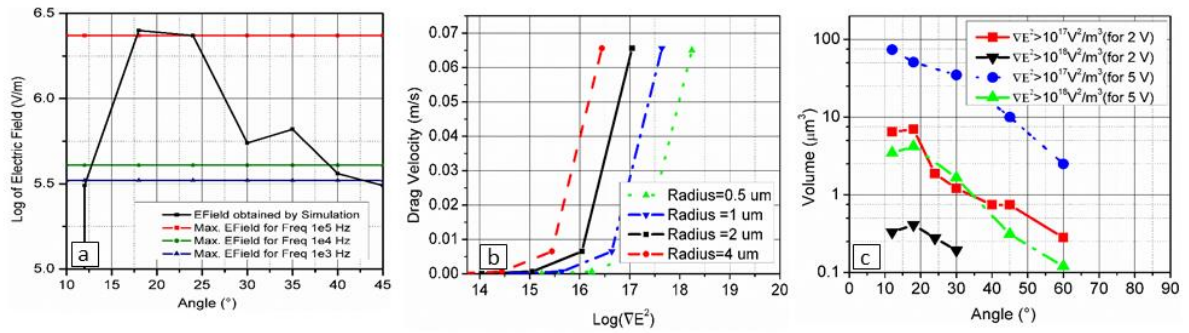
Figure 6. 9 Plot of electric field for conical electrodes. a) Plot of the electric field at various angles and the maximum field sustained at various semi angles of cone for 2 micron yeast cells without lysing at 2V. b) Plot of the drag velocity vs the log value of the ∇E^2 for yeast cells with radii 1, 2 and 4 μm. c) Plot of the volume of highest gradient for different angles at the tip.

If the frequency of electric field selected is 10 kHz, none of the models except the angle 45° can capture cells effectively without lysing them. The maximum transport velocity for the array can be based on the gradient of the electric field for the different models and is shown in Figure 6. 9b. A single cell should be trapped at the tip of the conical electrodes. To find if such trapping was feasible, the volumes of the region with desired values of DEP force were calculated. This was done using the derived values

obtained by interpolation function inbuilt in COMSOL. It was found that, the maximum

value of the gradient occurred at the tip of the electrode and had a value of around 10^{17}-

10^{18} (V^2/m^3). It was observed that the results for this gradient value were acceptable for

the voltage of 2V and 5V for the given conductivity. These are plotted in Figure 6. 9c.

Plots to demonstrate the points satisfying all the three parameters were further obtained

for the voltage of 2V and 5V. These figures enabled the comparison of different

parameters with the cone angle. Figure 6. 9c shows the angles with a favorable capture

volume and cell membrane potential.

Table 6. 1 Parameters for simulation study

	Parameter	Value
1.	Base Radius of cone	10,20,25 μm
2.	Semi angle of cone	Angles 12˚ to 60˚ (increment 6˚)
3.	Tip Radius of cone	0.5,1,2 μm
4.	Voltage applied	2,5,10 and20 V
5.	Gap between Cones	85μm
6.	Conductivity	0.001S/m for media

6.4 Discussion

In this work, feasibility of pick and place of selected cells using 3D carbon electrodes was demonstrated. The use of 3D electrodes enables picking of cells from the cell culture; the use of DEP provides selectivity of cells and the robotic arm enable the device to complete an automated cycle. This device can be looked as a modular addition to the liquid handling robots with the ability to selectively pick, transfer and possibly electroporate cells.

The current device has a resolution of 100 μm in its 3-dimensional movement due to the limitation of the robotic setup. This limited resolution affects the pick and place steps. The electrode footprint is around 40 μm (dia) and 100 μm (height), thus even the smallest error in the movement of the robotic arm can change the placement of the electrode. By improving the resolution, the movement of the header can be refined. One of the reasons that the cells obtained show contamination is the low efficiency of the wash step. Currently, owing to the footprint of the header, the wash tank used is much wider than the electrode chip and the device creates a path of high resistance in the movement of the liquid. One of the future goals will be to reduce the header footprint and the size of the wash tank. By making this change, the optimization of wash speed with the change in DEP properties of the cell and the size of the cell can be better correlated and will be repeatable. It is speculated that it is important to treat the electrode surfaces to enhance the performance of the electrodes. Along with the electrodes, it is important to treat all the surfaces that come in direct contact with the liquid to reduce wetting and subsequent contamination. In case of a cell like *C.albicans*, with the diameter of around 4 μm,

localized gradient will be needed for single cell pick and place. Thus, the use of conical electrodes will be recommended. Fabrication of such conical carbon structures using SU-8 photolithography with back exposure has been demonstrated earlier [57]. Secondly, the retrieval process of the cells at specific locations faces a challenge. A precise control of place step with a higher resolution of the robotic arm can solve this issue. Additionally since the Ti chip has 2D electrodes, it has limited range of electric field gradient along the height and fails to trap the cells that are not in the same plane. Due to the voltage limitations in the setup, electroporation of the cells could not be achieved. In the future work, with the use of higher voltage, the cells can be lysed on the 3D carbon electrodes that can replace the 2D Ti electrodes to ensure better placement of cells. By optimizing this system, there is a possibility to apply this technology to pick, place and analyze single cells.

6.5 Summary of findings and contribution

In this work, pick and place of selected cells was successfully demonstrated using 3D carbon electrodes on an automated robotic platform. The use of 3D electrodes enables picking of cells from the cell culture, the use of DEP provides selectivity of cells and the robotic arm enables the device to complete an automated cycle.

The dependence of the device performance on the DEP and flow parameters is studied here. The working of the pick step in the device is affected by the change in voltage and current frequency. The device shows capability of lifting cells of different sizes. The performance of the wash step is affected by the gap between the electrodes, wash speed and the number of runs. By using the equilibrium between DEP and drag

force, velocity could be determined to optimize the wash velocity. The relation between numbers of runs still needs to be determined. Further work to understand the DEP force acting on the cell in such a case is necessary.

Negative DEP can enable cell repulsion and efficient release of the cells as seen in the experiment. Using 2D electrodes to locate the released cells also proved helpful. The issues arising due to the limited range of electric field between the 2D electrodes limits the ability of precise placement. The fact that the cells are released in the media limits the ability of the cells to be easily deposited on the plate. Further work needs to target this part of the device.

CHAPTER SEVEN

CONCLUSION AND FUTURE WORK

This work encompasses the steps towards developing devices for rapid, continuous cell sorting and for automated cell sorting. First part of the work includes a systematic study of shrinkage during pyrolysis. In this analysis, the importance of degassing through surface area was investigated. The results show that surface area ratio or *SAR* is the most important factor in the basic shrinkage value for the SU-8 structure. A set of mathematical relations were obtained to calculate shrinkage based on *SAR,* pyrolysis temperature and pyrolysis atmosphere which are the factors that affect shrinkage. There still exist gaps to be addressed. These include studying the impact of pressure, degree of SU-8 cross-linking, and exploring effects of other atmospheres. These gaps can be addressed in the future by using simulation model that considers shrinkage as a transient effect. These steps are necessary towards designing manufacturing processes that yield carbon structures tailored to specific applications. The impact of heating rate and dwell time is analyzed here for a limited parameter values, due to the limitations of the furnace. For a complete picture, further analysis with high heating rates and dwell times is needed. The effect of atmospheric pressure is another important parameter, which can affect shrinkage and needs to be incorporated in the future work.

The 3D electrodes optimized in the first step were successfully used to fabricate the cylindrical electrodes for the applications of streamingDEP and robotic DEP. StreamingDEP was developed here as a separation technique that combines positive DEP

with flow based drag force for particle separation. The dominance of either of these forces, affects the particle behavior, based on which they can be captured, streamed or eluted. Application of this technique was investigated with neural stem cells, which have similar sizes but different membrane capacitances. An analytical streamingDEP number was developed which encapsulates the effect of the system parameters and device geometry in particle streaming. Experiments successfully validated the behavior predicted by streamingDEP number. In the future, streamingDEP number can be developed as a prediction tool used for designing separation devices. The further steps will incorporate the effect of shape of electrode, effect of particle size and the perturbation of the electric field due to the presence of particle in this study. The electrodes are observed to saturate with particles and give rise to streams after a certain time; this saturation behavior can be estimated through the streaming DEP number, as a further study and this will enable one to define distinct transition between the trapping and streaming. Future fabrication work will involve installing retrieval geometries to efficiently retrieve highly pure cells. The use of soft lithography techniques can enable such fabrication.

The third objective of this work was to demonstrate the feasibility of robotic pick and place of the cells using a 3D electrode device. The device fabricated in this work was able to successfully pick selected cells and transfer those to prescribed locations. The device was also successfully applied for single cell pick and transfer of stem cells and for cell separation. For transfer of smaller cells, electrodes with narrow tips that have limited capture volume (~ cell volume) with high electric field gradient will be needed. An

optimization study of conical geometries for single cell capture performed here can prove useful for future single cell capture devices. The current robotic device has an efficiency of about 80%, due to the low efficiency of the wash step. The future work will focus on optimizing the wash step by the use of smaller wash tank and a better surface finish on the entire surface of the electrodes and connections. A robotic arm with better spatial resolution needs to be used to obtain better performance on each step. The device is desired to have an ability to lyse cells by the change in voltage and drop intracellular components on the plate at desired locations. The entire envisioned setup will involve automated picking up of single cells by DEP based selection, transfer of these cells to place section, lysis of cells and release of intracellular material on the plate for analysis. The future device can be a modular addition to the liquid handling robots, which are commonplace in bioanalysis laboratories.

Study of shrinkage provides advancement in the understanding of the pyrolysis process during carbonization of SU-8. The streamingDEP number developed here builds an analytical model to study the system behavior. This can provide a design tool for developing streamingDEP devices in the future. Rapid cell separation with streamingDEP can be implemented for cell sorting in cell therapy, by being a potential alternative to label based sorting, due to high speed and efficiency that can be obtained. Robotic DEP can be a useful platform for single cell study, 3D culturing as well as cell patterning. This work is a stepping-stone for various future devices, which can be applied to healthcare diagnostics, single cell research and therapeutics.

APPENDICES

Appendix A

ANOVA and Tukey's test procedure followed for studying shrinkage

Analysis of Variance (ANOVA) was used to analyze the difference between average shrinkage obtained for different treatments. Treatment implies different shapes, pyrolysis temperatures, dwell times, heating rates and atmospheres. The procedure used here is the standard ANOVA procedure from Engineering Statistics.[204]

In case of the analysis for different shapes, different cross sectional shapes with similar SAR value are considered. Null hypothesis in this case is that the average shrinkage for the three cross sections does not show a statistically significant difference. If the P-value obtained for the analysis is smaller than 0.01, null hypothesis will be rejected at, it will imply that the average shrinkage for different shapes is different.

8 posts (samples) were analyzed for each shape to calculate percent shrinkage of characteristic dimension D and 5 posts were analyzed for calculating percent shrinkage in the height H. Three shapes were considered for SAR value of 2, namely, hexagon (SAR=2.15±0.84), square (SAR=1.88±1.07) and circle (SAR=1.80±0.23). Hence, number of treatments here will be 3 (Shape: Hexagon, Square and Circle). The average shrinkage and variance in case of each treatment was computed. Grand Mean was calculated by taking the average of all the treatments. Sum of Squares Between (SSB) was calculated using the Equation (A. 1);

$$SSB = (Number\ of\ samples) \qquad\qquad (A.1)$$

$$* (Grand\ Mean$$

$$- Average\ Shrinkage\ for\ each\ treatment)^2$$

Degrees of Freedom for SSB is given by (Number of Treatments-1). Hence in the case where 3 different shapes were analyzed, the Degrees of Freedom for SSB=2. Mean of SSB (MSSB) is calculated by dividing SSB by degrees of Freedom. SSB accounts for the difference in between the average shrinkage values between different treatments. Sum of Squares Within (SSW) was calculated using the Equation (A. 2);

$$\sum_{n=1}^{Number\ of\ Samples} (Average\ shrinkage\ for\ Treatment \qquad (A.2)$$

$$- Shrinkage\ for\ the\ sample)^2$$

Degrees of Freedom for SSW is given by (Number of Treatments*(Number of Samples-1)). Hence in the case where 3 different shapes were analyzed, with 8 posts in each case, the Degrees of Freedom for SSB=21. Mean of SSW (MSSW) is calculated by dividing SSW by degrees of Freedom. SSW accounts for the difference in between shrinkage values for different samples.

F-Statistics, as given by Equation (A. 3), is the ratio of the variation between different treatments to different samples. A high F-value signifies that the variation in between treatments is higher compared to that within particular treatments. Under Null Hypothesis, SSB and SSW are expected to be similar in value.

$$F \ Statistic = \frac{MSSB}{MSSW} \qquad\qquad (A. \ 3)$$

Based on the F-value and degrees of freedom, using the F table[205], P value can be noted. If the P-Value is greater than 0.01, Null Hypothesis was NOT rejected. For P-value smaller than 0.01, null hypothesis is rejected. If the Null hypothesis is rejected, it implies that the average shrinkage for each treatment is different. If the null hypothesis is rejected, Tuckey's test is used.

For example in the case of shrinkage at different temperatures, the P-value was smaller than 0.01 and hence the null hypothesis that the average shrinkage for all temperatures is same was rejected. For Tuckey's test, it is required to calculate the critical difference. This value is based on the degrees of freedom and variance in the data. If the variance in between two treatments, in this case, between two temperatures is greater than the critical difference, it implies that the two temperatures have different average shrinkage. To calculate the critical difference, the Q-statistics for the data is required.

For Tuckey's test, the degree of freedom for numerator is equal to number of treatments. For the case of analysis with different temperatures, 650, 900 and 1150°C were used. Hence number of treatments and the degree of freedom for numerator is 3. Degree of freedom for the denominator is calculated as the product of (total number of observations across all treatments-no. of treatments). Based on the Q-table[206], the Q statistic for the data is obtained. To calculate the pooled variance, the Equation (A. 4) is used.

$$Pooled\ Variance = (\frac{\sum_{n=1}^{Number\ of\ Treatments} \sigma^2}{Number\ of\ Treatments}) \qquad (A.4)$$

Critical difference is obtained as,

$$Critical\ Difference = Q * \sqrt{Pooled\ Variance} \qquad (A.5)$$

If absolute difference in the variance between a pair of treatments is greater than the critical difference, it indicates that the average shrinkage for the two treatments is statistically different.

Non-dimensional electrical and velocity field

B.1 Calculation of non-dimensional velocity:

Flow in the microfluidic channel can be represented as a flow between two stationary parallel plates. Accordingly, the equation of the flow in the z direction at the height h is given as;

$$U_h = 6U_a(h/H)(1 - \frac{h}{H}) \qquad \text{(B. 1)}$$

The flow profile at the height h in the x-y plane can also be represented as a parabola for flow between two vertical plates. U_h from Equation (B. 1) represents the maxima for this parabolic profile. Thus the average flow velocity at height h can be given as,

$$U_{ah} = \left(\frac{2}{3}\right)U_h = 4U_a(h/H)(1 - \frac{h}{H}) \qquad \text{(B. 2)}$$

The velocity in the y direction is the sum of u_{yDEP} and u_{yflow} in the domain. The DEP velocity in y-direction is at least 10^4 times smaller than the flow velocity and thus is makes negligible contribution to the total velocity. (Figure B. 1)
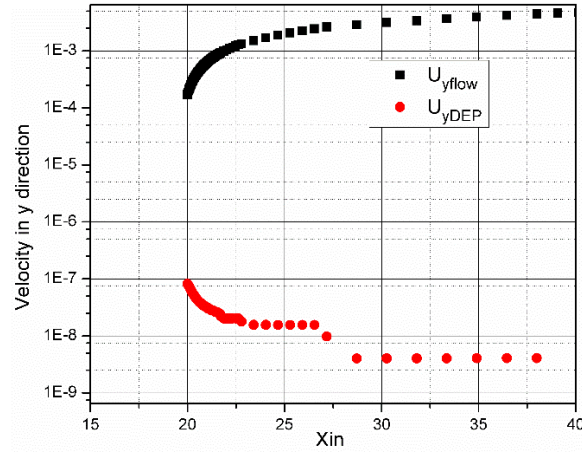
Figure B. 1 The comparison of u_{yDEP} and u_{yflow} in the region between electrodes

B.2 Calculation of electric field using COMSOL Multiphysics:

Equations (2. 32)-(2. 34) from Chapter 2 are solved in COMSOL Multiphysics. Electric field is non-dimensionalized (E^*) by dividing it by the distance *(d-r)* and by multiplying it by applied voltage *V*. This non-dimensional field is validated by using multiple values for the voltage *V*, distance *d* and electrode radius *r*. Electric field is calculated at different distances from the electrode as shown by the vertical lines in Figure B. 2A. The average electric field on each of these lines is plotted and a best fit curve is fitted to it as shown in Figure B. 2B. This best fit curve defines the average electric field in the domain between the two electrodes. The equation of this curve is given as;

$$E^* = 0.55(\frac{x^*}{\gamma})^{-1}$$

(B. 3)

148
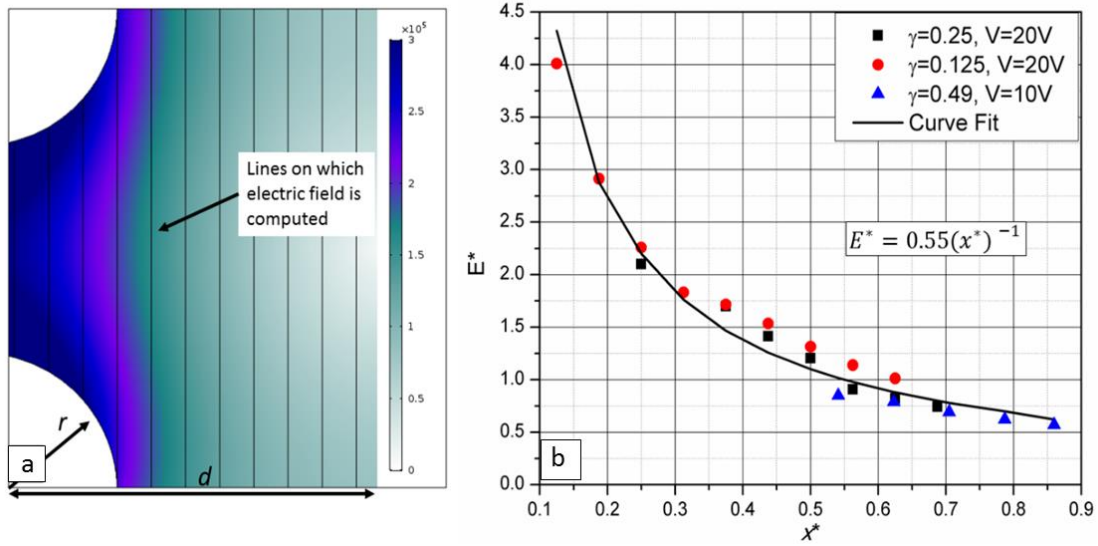
Figure B. 2. Non-dimensional electric field calculation in the domain. a) Average electric field is calculated on each of the vertical lines. b) Average electric field for three different cases is plotted against x* and a best fit curve is fitted to the data. The best-fit curve has r value of 0.95.

Similarly, velocity u in the domain is calculated for different values of d, r and Ua. The velocity on the line joining the electrodes is plotted and it shows a parabolic curve. A best-fit curve is derived for different combinations of the dimensions as shown in Figure B. 3. The non-dimensional equation of the velocity is given as,

$$u_{py} = 6.4U_a(X_{in}^* - \gamma)(1 - (X_{in}^* - \gamma))(2\gamma + 1)) \qquad (B.4)$$
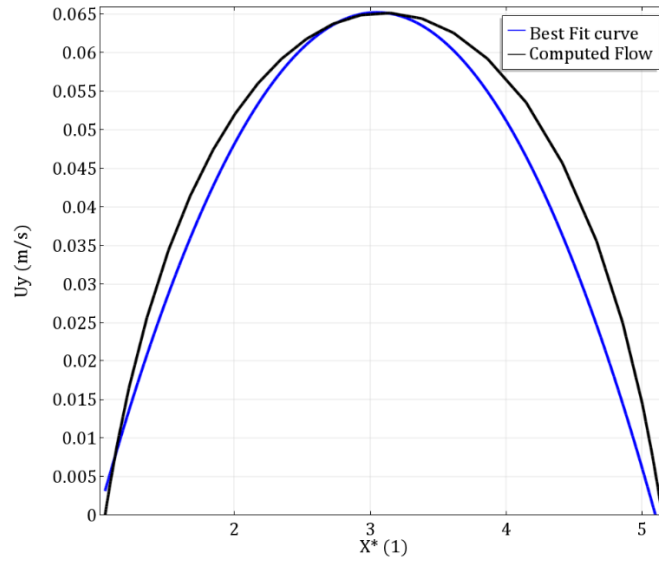
Figure B. 3 Curve of best fit for the velocity profile between two electrodes

The real part of Clausius Mossotti factor Re[fcm] for 1 um latex particles is

plotted in Figure B. 4 and was used to study the streaming behavior with the change in

frequency.
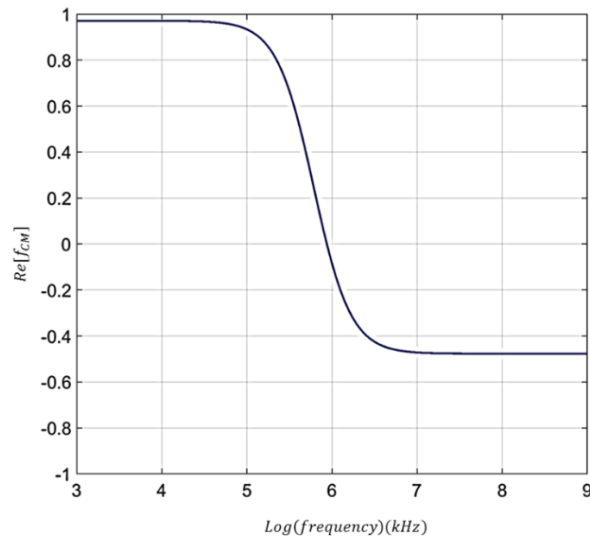
Figure B. 4 Re[fcm] for 1 μm latex particles. The value is calculated for the media

conductivity of 10-5 S/m and the conductivity of the latex particles was taken as 0.0052

S/m with surface conductance 1.3*10-^{9} S. Relative permittivity of the particles is taken to be 2.5.

B.3 Parameters calculated for the streamingDEP model by Cummings et. al

Table B. 1 Device parameters calculated for reference [170,189]

		For device in ref [170,189]
Design Parameters	r (m)	18*10^{-6}
	C_x (m)	63*10^{-6}
	C_y (m)	63*10^{-6}
	N	12
Particle and media properties	ε(F/m)	7.10*10^{-10}
	σ_m (S/m)	5*10^{-5}
	r_p(m)	5*10^{-7}
	σ_p(S/m)	0.018
	μ(Pa.s)	0.001
	Zeta potential (mV)	19.5
System parameters	V(V)	0.4 (calculated based on DEP force)
	f (kHz)	100
	U_a(m/s)	2.3*10^{-6} m/s (calculated for the electric field 25 V/mm)

REFERENCES

[1]   J. Kim, M. Johnson, P. Hill, B.K. Gale, Microfluidic sample preparation: cell lysis and nucleic acid purification., Integr. Biol. (Camb). 1 (2009) 574–586. doi:10.1039/b905844c.

[2]   J. El-Ali, P.K. Sorger, K.F. Jensen, Cells on chips., Nature. 442 (2006) 403–411. doi:10.1038/nature05063.

[3]   J. Lu, C.A. Barrios, A.R. Dickson, J.L. Nourse, A.P. Lee, L.A. Flanagan, Advancing practical usage of microtechnology: a study of the functional consequences of dielectrophoresis on neural stem cells, Integr. Biol. 4 (2012) 1223. doi:10.1039/c2ib20171b.

[4]   I. Doh, Y.H. Cho, A continuous cell separation chip using hydrodynamic dielectrophoresis (DEP) process, Sensors and Actuators A-Physical. 121 (2005) 59–65.

[5]   K.H. Kang, Y. Kang, X. Xuan, D. Li, Continuous separation of microparticles by size with direct current-dialectrophoresis, Electrophoresis. 27 (2006) 694–702. doi:10.1002/elps.200500558.

[6]   Y. Huang, E.L. Mather, J.L. Bell, M.J. Madou, MEMS-based sample preparation for molecular diagnostics, Anal. Bioanal. Chem. 372 (2002) 49–65.

[7]   S. Zheng, H. Lin, J.-Q. Liu, M. Balic, R. Datar, R.J. Cote, Y.-C. Tai, Membrane microfilter device for selective capture, electrolysis and genomic analysis of human circulating tumor cells., J. Chromatogr. A. 1162 (2007) 154–61. doi:10.1016/j.chroma.2007.05.064.

[8]   A.W. Wognum, A.C. Eaves, T.E. Thomas, Identification and isolation of hematopoietic stem cells., Arch. Med. Res. 34 (2004) 461–475. doi:10.1016/j.arcmed.2003.09.008.

[9]   Q. Zhang, R.H. Austin, Applications of Microfluidics in Stem Cell Biology, Bionanoscience. 2 (2012) 277–286. doi:10.1007/s12668-012-0051-8.

[10]   J. Fu, P. Mao, J. Han, Nanofilter array chip for fast gel-free biomolecule separation, Appl. Phys. Lett. 87 (2005) 1–3. doi:10.1063/1.2149979.

[11]   H. Lu, M. a Schmidt, K.F. Jensen, A microfluidic electroporation device for cell lysis., Lab Chip. 5 (2005) 23–29. doi:10.1039/b406205a.

[12]   M. Mahalanabis, H. Al-Muayad, M.D. Kulinski, D. Altman, C.M. Klapperich, Cell lysis and DNA extraction of gram-positive and gram-negative bacteria from whole blood in a disposable microfluidic chip., Lab Chip. 9 (2009) 2811–2817. doi:10.1039/b905065p.

[13]   A.M. Foudeh, T. Fatanat Didar, T. Veres, M. Tabrizian, Microfluidic designs and techniques using lab-on-a-chip devices for pathogen detection for point-of-care diagnostics, Lab Chip. 12 (2012) 3249–3266. doi:10.1039/c2lc40630f.

[14]   O. Laczka, J.M. Maesa, N. Godino, J. del Campo, M. Fougt-Hansen, J.P. Kutter, D. Snakenborg, F.X. Mu??oz-Pascual, E. Baldrich, Improved bacteria detection by coupling magneto-immunocapture and amperometry at flow-channel microband electrodes, Biosens. Bioelectron. 26 (2011) 3633–3640. doi:10.1016/j.bios.2011.02.019.

[15]   D.S. Reichmuth, S.K. Wang, L.M. Barrett, D.J. Throckmorton, W. Einfeld, A.K.

Singh, Rapid microchip-based electrophoretic immunoassays for the detection of swine influenza virus, Lab Chip. 8 (2008) 1319–1324. doi:10.1039/b801396a.

[16] R. Gómez-Sjöberg, A.A. Leyrat, D.M. Pirone, C.S. Chen, S.R. Quake, Versatile, fully automated, microfluidic cell culture system, Anal. Chem. 79 (2007) 8557–8563. doi:10.1021/ac071311w.

[17] K. Gupta, D.H. Kim, D. Ellison, C. Smith, A. Kundu, J. Tuan, K.Y. Suh, A. Levchenko, Lab-on-a-chip devices as an emerging platform for stem cell biology, Lab Chip. 10 (2010) 2019–2031. doi:10.1039/c004689b.

[18] N. Uchida, D.W. Buck, D. He, M.J. Reitsma, M. Masek, T. V Phan, A.S. Tsukamoto, F.H. Gage, I.L. Weissman, Direct isolation of human central nervous system stem cells., Proc. Natl. Acad. Sci. 97 (2000) 14720–5. doi:10.1073/pnas.97.26.14720.

[19] G.J. Spangrude, S. Heimfeld, I.L. Weissman, Purification and characterization of mouse hematopoietic stem cells, Science (80-.). 241 (1988) 58–62. doi:10.1126/science.2898810.

[20] M.P. Hughes, Technological developments in dielectrophoresis and its path to commercialization, Cell Gene Ther. Insights. 4 (2018) 81–88. doi:10.18609/cgti.2018.010.

[21] J. McGrath, M. Jimenez, H. Bridle, Deterministic lateral displacement for particle separation: a review, Lab Chip. 14 (2014) 4139–4158.

[22] M. Jiang, K. Budzan, G. Drazer, Fractionation by shape in deterministic lateral displacement microfluidic devices, Microfluid. Nanofluidics. 19 (2015) 427–434.

doi:10.1007/s10404-015-1572-6.

[23]   P. Tallapragada, N. Hasabnis, K. Katuri, S. Sudarsanam, K. Joshi, M.
       Ramasubramanian, Scale invariant hydrodynamic focusing and sorting of inertial
       particles by size in spiral micro channels, J. Micromechanics Microengineering. 25
       (2015). doi:10.1088/0960-1317/25/8/084013.

[24]   N. Nivedita, I. Papautsky, Continuous separation of blood cells in spiral
       microfluidic devices., Biomicrofluidics. 7 (2013) 54101. doi:10.1063/1.4819275.

[25]   A. Nilsson, F. Petersson, H. Jönsson, T. Laurell, Acoustic control of suspended
       particles in micro fluidic chips., Lab Chip. 4 (2004) 131–135.
       doi:10.1039/b313493h.

[26]   F. Guo, Z. Mao, Y. Chen, Z. Xie, J.P. Lata, P. Li, L. Ren, J. Liu, J. Yang, M. Dao,
       S. Suresh, T.J. Huang, Three-dimensional manipulation of single cells using
       surface acoustic waves, Proc. Natl. Acad. Sci. 113 (2016) 1522–1527.
       doi:10.1073/pnas.1524813113.

[27]   M. Chabert, J.-L. Viovy, Microfluidic high-throughput encapsulation and
       hydrodynamic self-sorting of single cells, Proc. Natl. Acad. Sci. 105 (2008) 3191–
       3196. doi:10.1073/pnas.0708321105.

[28]   L. Mazutis, J. Gilbert, W.L. Ung, D.A. Weitz, A.D. Griffiths, J.A. Heyman,
       Single-cell analysis and sorting using droplet-based microfluidics, Nat. Protoc. 8
       (2013) 870–891.
       doi:10.1038/nprot.2013.046\rhttp://www.nature.com/nprot/journal/v8/n5/abs/nprot
       .2013.046.html#supplementary-information.

[29]   D. Di Carlo, N. Aghdam, L.P. Lee, Single-cell enzyme concentrations, kinetics, and inhibition analysis using high-density hydrodynamic cell isolation arrays, Anal. Chem. 78 (2006) 4925–4930. doi:10.1021/ac060541s.

[30]   T.P. Hunt, R.M. Westervelt, Dielectrophoresis tweezers for single cell manipulation, Biomed. Microdevices. 8 (2006) 227–230. doi:10.1007/s10544-006-8170-z.

[31]   F. Arai, A. Ichikawa, M. Ogawa, T. Fukuda, K. Horio, K. Itoigawa, High-speed separation system of randomly suspended single living cells by laser trap and dielectrophoresis, Electrophoresis. 22 (2001) 283–288. doi:10.1002/1522-2683(200101)22:2<283::AID-ELPS283>3.0.CO;2-C.

[32]   S.C. Grover, A.G. Skirtach, R.C. Gauthier, C.P. Grover, Automated single-cell sorting system based on optical trapping, J. Biomed. Opt. 6 (2001) 14. doi:10.1117/1.1333676.

[33]   S.C. Chapin, V. Germain, E.R. Dufresne, Automated trapping, assembly, and sorting with holographic optical tweezers., Opt. Express. 14 (2006) 13095–13100. doi:10.1364/OE.14.013095.

[34]   E.W.H. Jager, O. Inganäs, I. Lundström, Microrobots for micrometer-size objects in aqueous media: Potential tools for single-cell manipulation, Science (80-.). 288 (2000) 2335–2338. doi:10.1126/science.288.5475.2335.

[35]   Y. Zhang, B.K. Chen, X. Liu, Y. Sun, Autonomous robotic pick-and-place of microobjects, IEEE Trans. Robot. 26 (2010) 200–207. doi:10.1109/TRO.2009.2034831.

[36]   E.B. Steager, M.S. Sakar, C. Magee, M. Kennedy, A. Cowley, V. Kumar, Automated biomanipulation of single cells using magnetic microrobots, 32 (2013) 346–359. doi:10.1177/0278364912472381.

[37]   K. Mølhave, T. Wich, A. Kortschack, P. Bøggild, Pick-and-place nanomanipulation using microfabricated grippers, (2006). doi:10.1088/0957-4484/17/10/002.

[38]   K.S.C.Æ.J.L. Æ, Viable cell handling with high aspect ratio polymer chopstick gripper mounted on a nano precision manipulator, (2008) 1627–1633. doi:10.1007/s00542-008-0580-9.

[39]   L. Valihrach, P. Androvic, M. Kubista, Platforms for single-cell collection and analysis, Int. J. Mol. Sci. 19 (2018) 22–24. doi:10.3390/ijms19030807.

[40]   R. Sakamoto, T. Saeki, M. Nagai, T. Shibata, S.- Base, 3D Manipulation of Single Cells Using Dielectrophoretic Probe Array, (n.d.) 8–10.

[41]   M. Abonnenc, N. Manaresi, M. Borgatti, G. Medoro, E. Fabbri, A. Romani, L. Altomare, M. Tartagni, R. Rizzo, O. Baricordi, E. Tremante, E. Lo Monaco, P. Giacomini, R. Guerrieri, R. Gambari, Programmable interactions of functionalized single bioparticles in a dielectrophoresis-based microarray chip, Anal. Chem. 85 (2013) 8219–8224. doi:10.1021/ac401296m.

[42]   J. Nilsson, M. Evander, B. Hammarström, T. Laurell, Review of cell and particle trapping in microfluidic systems., Anal. Chim. Acta. 649 (2009) 141–57. doi:10.1016/j.aca.2009.07.017.

[43]   D.R. Gossett, W.M. Weaver, A.J. MacH, S.C. Hur, H.T.K. Tse, W. Lee, H. Amini,

D. Di Carlo, Label-free cell separation and sorting in microfluidic systems, Anal. Bioanal. Chem. 397 (2010) 3249–3267. doi:10.1007/s00216-010-3721-9.

[44] J. Autebert, B. Coudert, F.C. Bidard, J.Y. Pierga, S. Descroix, L. Malaquin, J.L. Viovy, Microfluidic: An innovative tool for efficient cell sorting, Methods. 57 (2012) 297–307. doi:10.1016/j.ymeth.2012.07.002.

[45] P.R.C. Gascoyne, J. Vykoukal, Particle separation by dielectrophoresis, Electrophoresis. 23 (2002) 1973–1983.

[46] M. Li, R.K. Anand, Cellular dielectrophoresis coupled with single-cell analysis, Anal. Bioanal. Chem. 410 (2018) 2499–2515.

[47] S. Ranganathan, R. McCreery, S.M. Majji, M. Madou, Photoresist-derived carbon for microelectromechanical systems and electrochemical applications, J. Electrochem. Soc. 147 (2000) 277–282.

[48] R. Martinez-Duarte, F. Camacho-Alanis, P. Renaud, A. Ros, Dielectrophoresis of lambda-DNA using 3D carbon electrodes, Electrophoresis. 34 (2013) 1113–1122.

[49] M. Islam, R. Natu, R. Martinez-Duarte, Carbon MEMS for Selected Lab-on-a-Chip Applications, in: Carbon next Silicon? Book-2 Appl., 2015: pp. 79–100.

[50] R. Martinez-Duarte, R. a Gorkin, K. Abi-Samra, M.J. Madou, The integration of 3D carbon-electrode dielectrophoresis on a CD-like centrifugal microfluidic platform., Lab Chip. 10 (2010) 1030–43. doi:10.1039/b925456k.

[51] J. Gilmore, M. Islam, J. Duncan, R. Natu, R. Martinez-Duarte, Assessing the importance of the root mean square (RMS) value of different waveforms to determine the strength of a dielectrophoresis trapping force, Electrophoresis.

(2017) 1–4. doi:10.1002/elps.201600551.

[52]   R. Martinez-Duarte, Carbon-electrode Dielectrophoresis for Bioparticle

        Manipulation, ECS Trans. 61 (2014) 11–22.

[53]   Y. Yildizhan, N. Erdem, M. Islam, R. Martinez-Duarte, M. Elitas,

        Dielectrophoretic separation of live and dead monocytes using 3D carbon-

        electrodes, Sensors (Switzerland). 17 (2017). doi:10.3390/s17112691.

[54]   M. Islam, R. Natu, M.F. Larraga-Martinez, R. Martinez-Duarte, Enrichment of

        diluted cell populations from large sample volumes using 3D carbon-electrode

        dielectrophoresis, Biomicrofluidics. 10 (2016) 033107.

[55]   M.D.C. Jaramillo, R. Martínez-Duarte, M. Hüttener, P. Renaud, E. Torrents, A.

        Juárez, Increasing PCR sensitivity by removal of polymerase inhibitors in

        environmental samples by using dielectrophoresis., Biosens. Bioelectron. 43

        (2013) 297–303. doi:10.1016/j.bios.2012.12.049.

[56]   R. Martinez-Duarte, P. Renaud, M.J. Madou, A novel approach to

        dielectrophoresis using carbon electrodes, Electrophoresis. 32 (2011) 2385–2392.

[57]   R. Martinez-Duarte, SU-8 Photolithography as a Toolbox for Carbon MEMS,

        Micromachines. 5 (2014) 766–782.

[58]   M.D.C. Jaramillo, E. Torrents, R. Martinez-Duarte, M.J. Madou, A. Juarez, On-

        line separation of bacterial cells by carbon-electrode dielectrophoresis,

        Electrophoresis. 31 (2010) 2921–2928.

[59]   G. Mernier, R. Martinez-Duarte, R. Lehal, F. Radtke, P. Renaud, Very High

        Throughput Electrical Cell Lysis and Extraction of Intracellular Compounds Using

3D Carbon Electrodes in Lab-on-a-Chip Devices, Micromachines. 3 (2012) 574–581.

[60] R. Natu, M. Islam, R. Martinez-Duarte, Shrinkage Analysis of Carbon Micro Structures Derived from SU-8 Photoresist, ECS Trans. 72 (2016) 27–33.

[61] B.Y. Park, L. Taherabadi, C. Wang, J. Zoval, M.J. Madou, Electrical Properties and Shrinkage of Carbonized Photoresist Films and the Implications for Carbon Microelectromechanical Systems Devices in Conductive Media, J. Electrochem. Soc. 152 (2005) J136.

[62] R. Martinez-Duarte, P. Renaud, M. Madou, A novel approach to dielectrophoresis using carbon electrodes, Electrophoresis. 32 (2011) 2385–92.

[63] G.T. Teixidor, R. a Gorkin, P.P. Tripathi, G.S. Bisht, M. Kulkarni, T.K. Maiti, T.K. Battacharyya, J.R. Subramaniam, A. Sharma, B.Y. Park, M. Madou, Carbon microelectromechanical systems as a substratum for cell growth, Biomed. Mater. 3 (2008) 034116.

[64] L. Amato, A. Heiskanen, C. Caviglia, F. Shah, K. Zór, M. Skolimowski, M. Madou, L. Gammelgaard, R. Hansen, E.G. Seiz, M. Ramos, T.R. Moreno, A. Martínez-Serrano, S.S. Keller, J. Emnéus, Pyrolysed 3D-Carbon Scaffolds Induce Spontaneous Differentiation of Human Neural Stem Cells and Facilitate Real-Time Dopamine Detection, Adv. Funct. Mater. 24 (2014) 7042–7052.

[65] R.L. McCreery, Advanced Carbon Electrode Materials for Molecular Electrochemistry, Chem. Rev. 108 (2008) 2646–2687.

[66] C. Wang, M. Madou, From MEMS to NEMS with carbon, Biosens. Bioelectron.

20 (2005) 2181–2187.

[67] H. Xu, K. Malladi, C. Wang, L. Kulinsky, M. Song, M. Madou, Carbon post-microarrays for glucose sensors, Biosens. Bioelectron. 23 (2008) 1637–1644.

[68] B.Y. Park, M.J. Madou, Design, fabrication, and initial testing of a miniature PEM fuel cell with micro-scale pyrolyzed carbon fluidic plates, J. Power Sources. 162 (2006) 369–379.

[69] R.R. Kamath, M.J. Madou, Three-Dimensional Carbon Interdigitated Electrode Arrays for Redox-Amplification, Anal. Chem. 86 (2014) 2963–2971.

[70] S. Sharma, A. Khalajhedayati, T.J. Rupert, M.J. Madou, SU8 Derived Glassy Carbon for Lithium Ion Batteries, ECS Trans. 61 (2014) 75–84.

[71] G.T. Teixidor, R.B. Zaouk, B.Y. Park, M.J. Madou, Fabrication and characterization of three-dimensional carbon electrodes for lithium-ion batteries, J. Power Sources. 183 (2008) 730–740.

[72] H.-S. Min, B.Y. Park, L. Taherabadi, C. Wang, Y. Yeh, R. Zaouk, M.J. Madou, B. Dunn, Fabrication and properties of a carbon/polypyrrole three-dimensional microbattery, J. Power Sources. 178 (2008) 795–800.

[73] B. Hsia, M.S. Kim, M. Vincent, C. Carraro, R. Maboudian, Photoresist-derived porous carbon for on-chip micro-supercapacitors, Carbon N. Y. 57 (2013) 395–400.

[74] M. Beidaghi, W. Chen, C. Wang, Electrochemically activated carbon micro-electrode arrays for electrochemical micro-capacitors, J. Power Sources. 196 (2011) 2403–2409.

[75] R. Martinez-Duarte, J. Andrade-Roman, S.O. Martinez, M.J. Madou, A High Throughput Multi-stage, Multi-frequency Filter and Separation Device based on Carbon Dielectrophoresis, in: 11th Annu. NSTI Nanotechnol. Conf. Trade Show, 2008: pp. 316–319.

[76] H.A. Rouabah, B.Y. Park, R.B. Zaouk, H. Morgan, M.J. Madou, N.G. Green, Design and fabrication of an ac-electro-osmosis micropump with 3D high-aspect-ratio electrodes using only SU-8, J. Micromechanics Microengineering. 21 (2011) 035018.

[77] B.H. Lapizco-Encinas, R. V. Davalos, B. a. Simmons, E.B. Cummings, Y. Fintschenko, An insulator-based (electrodeless) dielectrophoretic concentrator for microbes in water, J. Microbiol. Methods. 62 (2005) 317–326. doi:10.1016/j.mimet.2005.04.027.

[78] E.B. Cummings, Streaming dielectrophoresis for continuous-flow microfluidic devices, IEEE Eng. Med. Biol. Mag. 22 (2003) 75–84.

[79] R. Martinez-Duarte, M.J. Madou, A novel approach to Dielectrophoresis using Carbon electrodes, in: 2009.

[80] R. Martinez-Duarte, Label-free Cell Sorting using Carbon-electrode Dielectrophoresis and Centrifugal Microfluidics, University of California, Irvine, 2010.

[81] J. Shin, Electrically active microarray of 3D carbon MEMS electrodes for pathogen detection systems, 2008.

[82] Y. Yildizhan, U.B. Gogebakan, A. Altay, M. Islam, R. Martinez-Duarte, M. Elitas,

Quantitative Investigation for the Dielectrophoretic Effect of Fluorescent Dyes at Single-Cell Resolution, ACS Omega. 3 (2018). doi:10.1021/acsomega.8b00541.

[83]   S. Silva, M. Negri, M. Henriques, R. Oliveira, D.W. Williams, J. Azeredo, Candida glabrata, Candida parapsilosis and Candida tropicalis: Biology, epidemiology, pathogenicity and antifungal resistance, FEMS Microbiol. Rev. 36 (2012) 288–305. doi:10.1111/j.1574-6976.2011.00278.x.

[84]   N.G. Green, H. Morgan, Dielectrophoresis of submicrometer latex spheres. 1. Experimental results, J. Phys. Chem. B. 103 (1999) 41–50.

[85]   N.L. Kennea, H. Mehmet, Neural stem cells., J. Pathol. 197 (2002) 536–550. doi:10.1002/path.1189.

[86]   S. Goldman, Stem and progenitor cell-based therapy of the human central nervous system., Nat. Biotechnol. 23 (2005) 862–871. doi:10.1038/nbt1119.

[87]   H. a. Pohl, The motion and precipitation of suspensoids in divergent electric fields, J. Appl. Phys. 22 (1951) 869–871. doi:10.1063/1.1700065.

[88]   T.B. Jones, Fundamentals, in: Electromechanics Part., 1995: pp. 5–33.

[89]   Z.R. Gagnon, Cellular dielectrophoresis: Applications to the characterization, manipulation, separation and patterning of cells, Electrophoresis. 32 (2011) 2466–2487. doi:10.1002/elps.201100060.

[90]   M.P. Hughes, Nanoelectromechanics in Engineering and Biology, 2000.

[91]   X. Wang, Y. Huang, R. Holzel, J.P.H. Burt, Theoretical and experimental of the dielectric , dielectrophoretic and electrorotational behaviour of colloidal particles, (1993).

[92]   Electrorotation of liposomes verification of dielectric multi shell model, (n.d.).

[93]   C.M. Das, F. Becker, S. Vernon, J. Noshari, C. Joyce, P.R.C. Gascoyne, Dielectrophoretic Segregation of Different Human Cell Types on Microscope Slides, 77 (2005) 2708–2719. doi:10.1021/ac048196z.

[94]   A.K.M. Zaidi, D. Thaver, S.A. Ali, T.A. Khan, Pathogens associated with sepsis in newborns and young infants in developing countries., Pediatr. Infect. Dis. J. 28 (2009) S10–S18. doi:10.1097/INF.0b013e3181958769.

[95]   R. Pethig, M.S. Talary, Dielectrophoretic detection of membrane morphology changes in Jurkat T-cells undergoing etoposide-induced apoptosis, Iet Nanobiotechnology. 1 (2007) 2–9. doi:DOI 10.1049/iet-nbt:20060018.

[96]   J.L. Prieto, J. Lu, J.L. Nourse, L.A. Flanagan, A.P. Lee, Frequency discretization in dielectrophoretic assisted cell sorting arrays to isolate neural cells, Lab Chip. 12 (2012) 2182–2189. doi:10.1039/c2lc21184j.

[97]   M. Stephens, M.S. Talary, R. Pethig, A.K. Burnett, K.I. Mills, The dielectrophoresis enrichment of CD34+ cells from peripheral blood stem cell harvests, Bone Marrow Transpl. 18 (1996) 777–782.

[98]   E.A. Henslee, P. Crosby, S.J. Kitcatt, J.S.W. Parry, A. Bernardini, R.G. Abdallat, G. Braun, H.O. Fatoyinbo, E.J. Harrison, R.S. Edgar, K.F. Hoettges, A.B. Reddy, R.I. Jabr, M. von Schantz, J.S. O'Neill, F.H. Labeed, Rhythmic potassium transport regulates the circadian clock in human red blood cells, Nat. Commun. 8 (2017) 1978. doi:10.1038/s41467-017-02161-4.

[99]   F.H. Labeed, J. Lu, H.J. Mulhall, S.A. Marchenko, K.F. Hoettges, L.C. Estrada,

A.P. Lee, M.P. Hughes, L.A. Flanagan, Biophysical characteristics reveal neural stem cell differentiation potential, PLoS One. 6 (2011) 1–11. doi:10.1371/journal.pone.0025458.

[100] P. Bagnaninchi, N. Drummond, I. Giaever, Real-time label-free monitoring of adipose-derived stem cell differentiation with electric cell-substrate impedance sensing, Proc. Natl. Acad. Sci. 108 (2011) 6462–6467. doi:10.1073/pnas.1018260108.

[101] D.M. Vykoukal, P.R.C. Gascoyne, J. Vykoukal, Dielectric characterization of complete mononuclear and polymorphonuclear blood cell subpopulations for label-free discrimination., Integr. Biol. (Camb). 1 (2009) 477–84. doi:10.1039/b906137a.

[102] M.S. Talary, K.I. Mills, T. Hoy, A.K. Burnett, R. Pethig, Dielectrophoretic separation and enrichment of CD34 cell subpopulations from bone marrow, Med. Biol. Eng. Comput. 33 (1995) 235–237.

[103] L.A. Flanagan, J. Lu, L. Wang, S.A. Marchenko, N.L. Jeon, A.P. Lee, E.S. Monuki, Unique Dielectric Properties Distinguish Stem Cells and Their Differentiated Progeny, Stem Cells. 26 (2008) 656–665. doi:10.1634/stemcells.2007-0810.

[104] J. Vykoukal, D.M. Vykoukal, S. Freyberg, E.U. Alt, P.R.C. Gascoyne, Enrichment of putative stem cells from adipose tissue using dielectrophoretic field-flow fractionation., Lab Chip. 8 (2008) 1386–93. doi:10.1039/b717043b.

[105] H. Morgan, M.P. Hughes, N.G. Green, Separation of submicron bioparticles by

dielectrophoresis, Biophys. J. 77 (1999) 516–525.

[106]   J. Park, S. Song, H. Jung, Continuous focusing of microparticles using inertial lift
force and vorticity via multi-orifice microfluidic channels, (2009) 939–948.
doi:10.1039/b813952k.

[107]   J. Zhang, S. Yan, G. Alici, N.T. Nguyen, D. Di Carlo, W. Li, Real-time control of
inertial focusing in microfluidics using dielectrophoresis (DEP), RSC Adv. 4
(2014) 62076–62085. doi:10.1039/c4ra13075h.

[108]   J. Zhang, D. Yuan, Q. Zhao, S. Yan, S.Y. Tang, S.H. Tan, J. Guo, H. Xia, N.T.
Nguyen, W. Li, Tunable particle separation in a hybrid dielectrophoresis (DEP)-
inertial microfluidic device, Sensors Actuators, B Chem. 267 (2018) 14–25.
doi:10.1016/j.snb.2018.04.020.

[109]   J. Zhou, I. Papautsky, Fundamentals of inertial focusing in microchannels, Lab
Chip. 13 (2013) 1121–1132. doi:10.1039/c2lc41248a.

[110]   Y. Huang, X. Wang, F.F. Becker, P.R.C. Gascoyne, Introducing dielectrophoresis
as new force field for field-flow fractionation, Biophys. J. 73 (1997) 1118–1129.

[111]   P.S. Williams, T. Koch, J.C. Giddings, Charactierzation of near-wall
hydrodynamic lift forces using sedimentation field-flow fractionation, Chem. Eng.
Commun. 111 (1992) 121–147.

[112]   A. Castellanos, A. Ramos, A. Gonzalez, N.G. Green, H. Morgan,
Electrohydrodynamics and dielectrophoresis in microsystems : scaling laws, J.
Phys. D. Appl. Phys. 36 (2003) 2584–2597.

[113]   A. Castellanos, A. Ramos, A. González, N.G. Green, H. Morgan,

Electrohydrodynamics and dielectrophoresis in microsystems: scaling laws, J. Phys. D. Appl. Phys. 36 (2003) 2584–2597.

[114] A. Ramos, H. Morgan, N.G. Green, A. Castellanos, Ac electrokinetics: a review of forces in microelectrode structures, J. Phys. D. Appl. Phys. 31 (1998) 2338–2353.

[115] P.K. Wong, C.Y. Chen, T.H. Wang, C.M. Ho, An AC electroosmotic processor for biomolecules, TRANSDUCERS 2003 - 12th Int. Conf. Solid-State Sensors, Actuators Microsystems, Dig. Tech. Pap. 1 (2003) 20–23. doi:10.1109/SENSOR.2003.1215243.

[116] D.W. Lee, Y.H. Cho, A continuous electrical cell lysis device using a low dc voltage for a cell transport and rupture, Sensors Actuators, B Chem. 124 (2007) 84–89. doi:10.1016/j.snb.2006.11.054.

[117] R. Kostecki, X. Song, K. Kinoshita, Electrochemical Analysis of Carbon Interdigitated Microelectrodes, 2 (1999) 465–467.

[118] R. Kostecki, X. Song, K. Kinoshita, Fabrication of Interdigitated Carbon Structures by Laser Pyrolysis of Photoresist, Electrochem. Solid-State Lett. 5 (2002) E29–E31.

[119] Z. Tang, T. Shi, J. Gong, L. Nie, S. Liu, An optimized process for fabrication of high-aspect-ratio photoresist-derived carbon microelectrode array on silicon substrate, Thin Solid Films. 518 (2010) 2701–2706.

[120] B.Y. Park, L. Taherabadi, C. Wang, J. Zoval, M.J. Madou, Electrical Properties and Shrinkage of Carbonized Photoresist Films and the Implications for Carbon Microelectromechanical Systems Devices in Conductive Media, J. Electrochem.

Soc. 152 (2005) J136–J143.

[121] A. Singh, J. Jayaram, M. Madou, S. Akbar, Pyrolysis of negative photoresists to fabricate carbon structures for microelectromechanical systems and electrochemical applications, J. Electrochem. Soc. 149 (2002) E78–E83.

[122] S. Ranganathan, R. McCreery, S.M. Majji, M. Madou, Photoresist-Derived Carbon for Microelectromechanical Systems and Electrochemical Applications, J. Electrochem. Soc. 147 (2000) 277–282.

[123] L. Amato, A. Heiskanen, R. Hansen, L. Gammelgaard, T. Rindzevicius, M. Tenje, J. Emne, Dense high-aspect ratio 3D carbon pillars on interdigitated microelectrode arrays, Carbon N. Y. 94 (2015) 792–803.

[124] C. Wang, L. Taherabadi, G. Jia, M. Madou, Y. Yeh, B. Dunn, C-MEMS for the Manufacture of 3D Microbatteries, Electrochem. Solid-State Lett. 7 (2004) A435–A438.

[125] M.M. Wang, E. Tu, D.E. Raymond, J.M. Yang, H. Zhang, N. Hagen, B. Dees, E.M. Mercer, A.H. Forster, I. Kariv, P.J. Marchand, W.F. Butler, Microfluidic sorting of mammalian cells by optical force switching, Nat. Biotechnol. 23 (2005) 83–87.

[126] O.J.A. Schueller, S.T. Brittain, G.M. Whitesides, Fabrication of glassy carbon microstructures by pyrolysis of microfabricated polymeric precursors, Adv. Mater. 9 (1997) 477–480.

[127] E. Fitzer, W. Schaefer, S. Yamada, The Formation of Glasslike Carbon by Pyrolysis of Polyfurfuryl Alcohol and Phenolic Resin, Carbon N. Y. 7 (1969) 643–

648.

[128] E. Giogli, M. Islam, R. Martinez-Duarte, Fabricating suspended carbon wires using SU-8 photolithography, in: ECS Trans., 2016. doi:10.1149/07201.0125ecst.

[129] C.L. Wang, G.Y. Jia, L.H. Taherabadi, M.J. Madou, A Novel Method for the Fabrication of High-Aspect Ratio C-MEMS Structures, J. Microelectromechanical Syst. 14 (2005) 348–358.

[130] C.S. Sharma, A. Sharma, M. Madou, Multiscale carbon structures fabricated by direct micropatterning of electrospun mats of SU-8 photoresist nanofibers., Langmuir. 26 (2010) 2218–22.

[131] K. Malladi, C. Wang, M. Madou, Fabrication of suspended carbon microstructures by e-beam writer and pyrolysis, Carbon N. Y. 44 (2006) 2602–2607.

[132] D.-Y. Kang, C. Kim, G. Park, J.H. Moon, Liquid immersion thermal crosslinking of 3D polymer nanopatterns for direct carbonisation with high structural integrity, Sci. Rep. 5 (2015) 18185.

[133] J.A. Lee, S.W. Lee, K.-C. Lee, S. Il Park, S.S. Lee, Fabrication and characterization of freestanding 3D carbon microstructures using multi-exposures and resist pyrolysis, J. Micromechanics Microengineering. 18 (2008) 035012.

[134] R. Martinez-Duarte, M.J. Madou, G. Kumar, J. Schroers, A novel method for Amorphous Metal Micromolding using Carbon MEMS, in: Proc. Transducers 2009, Denver, CO, 2009: pp. 188–191.

[135] E. Giogli, M. Islam, R. Martinez-Duarte, Fabricating Suspended Carbon Wires Using SU-8 Photolithography, ECS Trans. 72 (2016) 125–134.

[136] R. Du, S. Ssenyange, M. Aktary, M.T. Mcdermott, Fabrication and Characterization of Graphitic Carbon Nanostructures with Controllable Size , Shape , and Position, Small. 5 (2009) 1162–1168.

[137] A.M. Lyons, L.P. Hale, C.W. Wilkins Jr, Photodefinable carbon films : Control of image quality, J. Vac. Sci. Technol. B Microelectron. Process. Phenom. 3 (1985) 447–452.

[138] A. Mardegan, R. Kamath, S. Sharma, P. Scopece, P. Ugo, M. Madou, Optimization of Carbon Electrodes Derived from Epoxy-based Photoresist, J. Electrochem. Soc. 160 (2013) B132–B137.

[139] R.J. Ong, T.A. Berfield, N.R. Sottos, D.A. Payne, Sol–gel derived Pb(Zr,Ti)O3 thin films: Residual stress and electrical properties, J. Eur. Ceram. Soc. 25 (2005) 2247–2251.

[140] C. J. Kleverlaan, A.J. Feilzer, Polymerization shrinkage and contraction stress of dental resin composites, Dent. Mater. 21 (2005) 1150–1157.

[141] S.F. Walsh, Shrinkage and Warpage Prediction for Injection Molded Components*, J. Reinf. Plast. Compos. 12 (1993) 769–777.

[142] J.L. Ferraane, Developing a more complete understanding of stresses produced in dental composites during polymerization, Dent. Mater. 21 (2005) 36–42.

[143] G. Jenkins, K. Kawamura, L. Ban, Formation and structure of polymeric carbons, Proc. R. Soc. Lond. A. Math. Phys. Sci. 327 (1972) 501–517.

[144] L.H. Lee, Mechanisms of Thermal Degradation of Phenolic Condensation Polymers. II. Thermal Stability and Degradation Schemes of Epoxy Resins, J.

Polym. Sci. Part A. 3 (1965) 859–882.

[145] H. Nakagawa, S. Tsuge, Studies on Thermal Degradation of Epoxy Resins by High-Resolution Pyrolysis-Gas Chromatography, J. Anal. Appl. Pyrolysis. 12 (1987) 97–113.

[146] C. Beyler, M. Hirschler, Thermal decomposition of polymers, in: SFPE Handb. Fire Prot. Eng., Natl Fire Protection Assn, Quincy, MA, 2002: pp. 110–131.

[147] T. Noda, M. Inagaki, S. Yamada, Glass-Like Carbons, J. Non. Cryst. Solids. 1 (1969) 285–302.

[148] H.-J. Kim, Y.-H. Joo, S.-M. Lee, C. Kim, Characteristics of Photoresist-derived Carbon Nanofibers for Li-ion Full Cell Electrode, Trans. Electr. Electron. Mater. 15 (2014) 265–269.

[149] Y.M. Hassan, C. Caviglia, S. Hemanth, D.M.A. Mackenzie, T.S. Alstrøm, D.H. Petersen, S.S. Keller, High temperature SU-8 pyrolysis for fabrication of carbon electrodes, J. Anal. Appl. Pyrolysis. (2017) 91–99.

[150] S. Sharma, M. Madou, Micro and nano patterning of carbon electrodes for bioMEMS, Bioinspired, Biomim. Nanobiomater. 1 (2012) 252–265.

[151] L. Liew, R.A. Saravanan, V.M. Bright, M.L. Dunn, J.W. Daily, R. Raj, Processing and characterization of silicon carbon-nitride ceramics : application of electrical properties towards MEMS thermal actuators, 103 (2003) 171–181.

[152] J. Su, A.C. Lua, Effects of carbonisation atmosphere on the structural characteristics and transport properties of carbon membranes prepared from Kapton ® polyimide, 305 (2007) 263–270.

[153] A. Bejan, A.. Kraus, Forced convection: forced flows, in: Heat Tranfser Handb., John Wiley & Sons, Inc., 2003.

[154] T.E. ToolBox, Hydrogen-Specific Heat, (n.d.). http://www.engineeringtoolbox.com/hydrogen-d_976.html.

[155] The Engineering Toolbox, Nitrogen-Specific Heat, (n.d.).

[156] E. book S.R. comparators D. Supplies, Themal conductivity of Gases Chart, (n.d.). http://www.engineersedge.com/heat_transfer/thermal-conductivity-gases.htm.

[157] A.M. Lyons, C.W. Wilkins, M. Robbins, Thin pinhole-free carbon films, Thin Solid Films. 103 (1983) 333–341.

[158] B. Dickens, Thermally Degrading Polyethylene Studied by Means of Factor- Jump Thermogravimetry, J. Polym. Sci. Part A Polym. Chem. 20 (1982) 1065–1087.

[159] Q. Jia, A.C. Lua, Effects of pyrolysis conditions on the physical characteristics of oil-palm-shell activated carbons used in aqueous phase phenol adsorption, J. Anal. Appl. Pyrolysis. 83 (2008) 175–179.

[160] V. Seebauer, J. Petek, G. Staundinger, Effects of particle size, heating rate and pressure on measurement of pyrolysis kinetics by thermogravimetric analysis, Fuel. 76 (1997) 127–1282.

[161] E. Cetin, B. Moghtaderi, R. Gupta, T.. Wall, Influence of pyrolysis conditions on the structure and gasification reactivity of biomass chars, Fuel. 83 (2004) 2139–2150.

[162] K. Murata, K. Sato, Y. Sakata, Effect of pressure on thermal degradation of polyethylene, J. Anal. Appl. Pyrolysis. 71 (2004) 569–589.

[163] P.W. Zandstra, A. Nagy, Tem ell ioengineering, Growth Factors. (2001) 275–305.

[164] R.A. Koeppe, C. Cortex, M. Petrides, B. Alivisatos, E. Meyer, A.C. Evans, P. Natl, A. Sci, A.M. Owen, A.C. Evans, E. Zarahn, J.D. Cohen, H.B. Mapp, J.D. Cohen, D.M. Barch, S.A. Spence, S.R. Hirsch, D.L. Clarke, C.B. Johansson, J. Wilbertz, B. Veress, E. Nilsson, H. Karlstro, U. Lendahl, J. Frise, Generalized Potential of Adult Neural Stem Cells, 288 (2000) 1660–1663.

[165] G. Martino, G. Martino, S. Pluchino, S. Pluchino, The therapeutic potential of neural stem cells., Nat. Rev. Neurosci. 7 (2006) 395–406. doi:10.1038/nrn1908.

[166] S. Okada, K. Ishii, J. Yamane, A. Iwanami, T. Ikegami, H. Katoh, Y. Iwamoto, M. Nakamura, H. Miyoshi, H.J. Okano, C.H. Contag, Y. Toyama, H. Okano, In vivo imaging of engrafted neural stem cells: its application in evaluating the optimal timing of transplantation for spinal cord injury., FASEB J. 19 (2005) 1839–1841. doi:10.1096/fj.05-4082fje.

[167] A.C. Schnitzler, A. Verma, D.E. Kehoe, D. Jing, J.R. Murrell, K.A. Der, M. Aysola, P.J. Rapiejko, S. Punreddy, M.S. Rook, Bioprocessing of human mesenchymal stem/stromal cells for therapeutic use: Current technologies and challenges, Biochem. Eng. J. 108 (2015) 3–13. doi:10.1016/j.bej.2015.08.014.

[168] J. Teissié, M.P. Rols, An experimental evaluation of the critical potential difference inducing cell membrane electropermeabilization., Biophys. J. 65 (1993) 409–413. doi:10.1016/S0006-3495(93)81052-X.

[169] M.A. Saucedo-Espinosa, B.H. Lapizco-Encinas, Design of insulator-based dielectrophoretic devices: Effect of insulator posts characteristics, J. Chromatogr.

A. 1422 (2015) 325–333. doi:10.1016/j.chroma.2015.10.030.

[170] E.B. Cummings, A.K. Singh, Dielectrophoresis in Microchips Containing Arrays of Insulating Posts: Theoretical and Experimental Results, Anal. Chem. 75 (2003) 4724–4731.

[171] C. Wang, L. Taherabadi, G. Jia, S. Kassegne, J. Zoval, M. Madou, Carbon-MEMS architectures for 3D microbatteries, Proc. SPIE. 5455 (2004) 295–302.

[172] J. a. Rogers, R.G. Nuzzo, Recent progress in soft lithography, Mater. Today. 8 (2005) 50–56. doi:10.1016/S1369-7021(05)00702-9.

[173] M. Serra, C. Brito, C. Correia, P.M. Alves, Process engineering of human pluripotent stem cells for clinical application, Trends Biotechnol. 30 (2012) 350–359. doi:10.1016/j.tibtech.2012.03.003.

[174] A. Nakano, T.-C. Chao, F. Camacho-Alanis, A. Ros, Immunoglobulin G and bovine serum albumin streaming dielectrophoresis in a microfluidic device, Microfluid. Miniaturization. 32 (2011) 2314–2322.

[175] C. Ming-Hsunwu, W. Chih-Yung, Y. Ruey-Hor, W. Ming-Chneg, W. An-Bang, Experimental and numerical study of the separation angle for flow around a circular cylinder at low Reynolds number, J. Fluid Mech. 515 (2004) 233–260.

[176] A. Vakil, S.I. Green, Numerical Study of Two-Dimensional Circular Cylinders in Tandem at Moderate Reynolds Numbers, J. Fluids Eng. 135 (2013) 071204–0771213.

[177] G. Juncu, A numerical study of momentum and forced convection heat transfer around two tandem circular cylinders at low Reynolds numbers. Part I: Momentum

transfer, Int. J. Heat Mass Transf. 50 (2007) 3788–98.

[178] R. Martinez-duarte, S. Cito, E. Collado-arredondo, S.O. Martinez, M.J. Madou, Fluido-Dynamic and Electromagnetic Characterization of 3D Carbon Dielectrophoresis with Finite Element Analysis, Sensors & Transducers. 3 (2008) 25–36.

[179] J.G. Kralj, M.T.W. Lis, M.A. Schmidt, K.F. Jensen, Continuous dielectrophoretic size-based particle sorting, Anal. Chem. 78 (2006) 5019–5025. doi:10.1021/ac0601314.

[180] T. Schnelle, T. Muller, G. Gradl, S.G. Shirley, G. Fuhr, Paired microelectrode system: dielectrophoretic particle sorting and force calibration, J. Electrostat. 47 (1999) 121–132.

[181] M. Islam, R. Natu, R. Martinez-Duarte, A study on the limits and advantages of using a desktop cutter plotter to fabricate microfluidic networks, Microfluid. Nanofluidics. 19 (2015) 973–985. doi:10.1007/s10404-015-1626-9.

[182] A. Kale, X. Lu, S. Patel, X. Xuan, Continuous-flow dielectrophoretic trapping and patterning of colloidal particles in a ratchet microchannel, J. Micromechanics Microengineering. 24 (2014).

[183] N.C. Chen, C.H. Chen, M.K. Chen, L.S. Jang, M.H. Wang, Single-cell trapping and impedance measurement utilizing dielectrophoresis in a parallel-plate microfluidic device, Sensors Actuators, B Chem. 190 (2014) 570–577. doi:10.1016/j.snb.2013.08.104.

[184] M. Li, S. Li, W. Cao, W. Li, W. Wen, G. Alici, Continuous particle focusing in a

waved microchannel using negative dc dielectrophoresis, J. Micromechanics Microengineering. 22 (2012).

[185] Y. Ai, Z. Zeng, S. Qian, Direct numerical simulation of AC dielectrophoretic particle-particle interactive motions, J. Colloid Interface Sci. 417 (2014) 72–79. doi:10.1016/j.jcis.2013.11.034.

[186] Y. Ai, S. Qian, DC dielectrophoretic particle-particle interactions and their relative motions, J. Colloid Interface Sci. 346 (2010) 448–454. doi:10.1016/j.jcis.2010.03.003.

[187] X. Wang, Y. Huang, Particle dipole-dipole interaction in AC electric fields, in: Proceeding 16th IEEE Eng. Med. Biol., 1996.

[188] H.-H. Cui, J. Voldman, X.-F. He, K.-M. Lim, Separation of particles by pulsed dielectrophoresis, Lab Chip. 9 (2009) 2306–2312.

[189] E. Cummings, Streaming Dielectrophoresis for Continuous-Flow Microfluidic Devices, IEEE Eng. Med. Biol. Mag. (2003) 75–84.

[190] R. Stepanauskas, Single cell genomics: An individual look at microbes, Curr. Opin. Microbiol. 15 (2012) 613–620. doi:10.1016/j.mib.2012.09.001.

[191] R.J. Elshire, J.C. Glaubitz, Q. Sun, J.A. Poland, K. Kawamoto, E.S. Buckler, S.E. Mitchell, A robust, simple genotyping-by-sequencing (GBS) approach for high diversity species, PLoS One. 6 (2011) 1–10. doi:10.1371/journal.pone.0019379.

[192] W.Z. Shou, M. Pelzer, T. Addison, X. Jiang, W. Naidong, An automatic 96-well solid phase extraction and liquid chromatography–tandem mass spectrometry method for the analysis of morphine, morphine-3-glucuronide and morphine-6-

glucuronide in human plasma, J. Pharm. Biomed. Anal. 27 (2002) 143–152.

[193] C.J. Fregeau, C.M. Lett, R.M. Fourney, Validation of a DNA IQ^{TM}-based extraction method for TECAN robotic liquid handling workstations for processing casework, Forensic Sci. Int. Genet. 4 (2010) 292–304.

[194] A. Hopwood, J. Brookes, A. Shariff, P. Cage, E. Tatum, R. Mirza, A Fully Integrated Robotic System for High Sample Throughput Within a DNA Databasing Unit A Fully Integrated Robotic System for High Sample Throughput Within a DNA Databasing Unit, (2015).

[195] D. Paull, A. Sevilla, H. Zhou, A.K. Hahn, H. Kim, C. Napolitano, A. Tsankov, L. Shang, K. Krumholz, P. Jagadeesan, C.M. Woodard, B. Sun, T. Vilboux, M. Zimmer, E. Forero, D.N. Moroziewicz, H. Martinez, M.C. V. Malicdan, K.A. Weiss, L.B. Vensand, C.R. Dusenberry, H. Polus, K.T.L. Sy, D.J. Kahler, W.A. Gahl, S.L. Solomon, S. Chang, A. Meissner, K. Eggan, S.A. Noggle, Automated, high-throughput derivation, characterization and differentiation of induced pluripotent stem cells, Nat. Methods. 12 (2015) 885–892. doi:10.1038/nmeth.3507.

[196] M. Muraro, G. Dharmadhikari, D. Grun, N. Groen, T. Dielen, E. Jansen, L. van Gurp, M.A. Engelse, F. Carlotti, E.J.P. de Koning, A. van Oudenaarden, A Single-Cell Transcriptome Atlas of the Human Pancreas, Cell Syst. 3 (2016) 385–394.e3.

[197] S.A. Sundberg, High-throughput and ultra-high-throughput screening: Solution and cell-based approaches, Curr. Opin. Biotechnol. 11 (2000) 47–53. doi:10.1016/S0958-1669(99)00051-8.

[198] R.P. Hertzberg, A.J. Pope, High-throughput screening: new technology for the 21st

century, Curr. Opin. Chem. Biol. 4 (2000) 445–451.

[199] C. Rinke, J. Lee, N. Nath, D. Goudeau, B. Thompson, N. Poulton, E. Dmitrieff, R. Malmstrom, R. Stepanauskas, T. Woyke, Obtaining genomes from uncultivated environmental microorganisms using FACS–based single-cell genomics, Nat. Protoc. 9 (2014) 1038–1048. doi:10.1038/nprot.2014.067.

[200] F. Kong, L. Yuan, Y.F. Zheng, W. Chen, Automatic liquid handling for life science: A Critical Review of the Current State of the Art, J. Lab. Autom. 17 (2012) 169–185. doi:10.1177/2211068211435302.

[201] R. Backhaus, J. Eberhardt, M. MEinhardt, G. Bornmann, Method and Device for Automated Removal of Cells and or Cell Colonies.pdf, 2007.

[202] L.D. Goldstein, Y.J.J. Chen, J. Dunne, A. Mir, H. Hubschle, J. Guillory, W. Yuan, J. Zhang, J. Stinson, B. Jaiswal, K.B. Pahuja, I. Mann, T. Schaal, L. Chan, S. Anandakrishnan, C. wah Lin, P. Espinoza, S. Husain, H. Shapiro, K. Swaminathan, S. Wei, M. Srinivasan, S. Seshagiri, Z. Modrusan, Massively parallel nanowell-based single-cell gene expression profiling, BMC Genomics. 18 (2017) 1–10. doi:10.1186/s12864-017-3893-1.

[203] S. Haupt, J. Grützner, M.C. Thier, T. Kallweit, B.H. Rath, I. Laufenberg, M. Forgber, J. Eberhardt, F. Edenhofer, O. Brüstle, Automated selection and harvesting of pluripotent stem cell colonies, Biotechnol. Appl. Biochem. 59 (2012) 77–87. doi:10.1002/bab.1014.

[204] D.C. Mongomery, G. C.Runger, N.F. Hubele, Engineering Statistics, 5th Edition, 2010.

[205] Statistics Online Computational Resource, F Distribution Tables, UCLA,

Statisctics, Neurol. LONI. (n.d.). http://www.socr.ucla.edu/applets.dir/f_table.html.

[206] R.E. Hamton, J.E. Havel, Critical Values for the Tukey Q Test, in: Introd. Biol.

Stat., Waveland Press, 2006: p. 162.